Condition Monitoring of Lithium Iron Phosphate Batteries by a Probabilistic and a Sensor-Based Approach

Dissertation

to attain the academic degree

"Doktor der Technischen Wissenschaften"

from

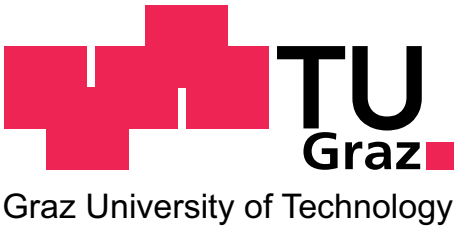

Institute of Electrical Measurement and Measurement Signal Processing
Inffeldgasse 23/2, 8010 Graz, Austria

supervisor: Univ.-Prof. Dipl.-Ing. Dr.techn. Georg Brasseur
co-supervisor: Univ.-Prof. Dr.phil. Heinz Krenn

submitted by: Dipl.-Ing. Thomas Gallien, BSc

Graz, May 23, 2016

Affidavit

I declare that I have authored this thesis independently, that I have not used other than the declared sources/resources, and that I have explicitly marked all material which has been quoted either literally or by content from the used sources. The text document uploaded to TUGRAZonline is identical to the present doctoral thesis.

....

date (signature)

Eidesstattliche Erklärung

Ich erkläre an Eides statt, dass ich die vorliegende Arbeit selbstständig verfasst, andere als die angegebenen Quellen/Hilfsmittel nicht benutzt und die den benutzten Quellen wörtlich und inhaltlich entnommenen Stellen als solche kenntlich gemacht habe. Das in TUGRAZonline hochgeladene Textdokument ist mit der vorliegenden Dissertation identisch.

Graz, am ....

(Unterschrift)

Abstract

In recent years, lithium ion batteries have become widely used energy sources for various battery-powered applications. Particularly for high-power automotive and storage applications, lithium iron phosphate ($LiFePO_4$) proved to be a promising cathode material for lithium ion batteries since it features low raw material costs, a high availability and an outstanding thermal stability. Especially the latter is of great significance for the automotive industry as the risk of battery fires in case of a traffic accident is significantly reduced compared e.g. to the hazard potential of $LiCoO_2$ batteries. Moreover, $LiFePO_4$ batteries offer high power density and are therefore preferably used for hybrid electric vehicle drive trains.

However, the user experiences a major drawback. Since the mechanism of insertion/depletion of lithium ions in the $LiFePO_4$ electrode proceeds according to a two-phase process, the electrode potential and, thus, the battery's terminal voltage shows a in wide ranges flat dependence on the state of charge. Additionally, hysteresis phenomena significantly influence the battery's open circuit voltage which are most likely caused by multiple thermodynamical equilibria in the $LiFePO_4$ electrode. Thus, the mapping between battery's state of charge and its open circuit voltage is not unique and strongly depends on the cycling history. This circumstance proves to be problematic if the task is to determine the battery's state of charge. Since this quantity is not directly accessible, state-of-the-art methods for condition monitoring infer the state of charge from measurements of the operating current and the battery's terminal voltage. Due to the mentioned mapping between the state of charge and the battery's open circuit voltage, these methods perform poorly in the case of $LiFePO_4$ batteries.

This thesis focuses on the task of the determination of the state of charge of $LiFePO_4$ batteries, by analyzing two different approaches. The first approach tackles the problem with Bayesian filtering. Thereby the open circuit voltage hysteresis is incorporated into the dynamic model and a joint estimation framework utilizing a sequential Monte Carlo method is used. The second approach is based on the basically novel idea of inferring the state of charge from the battery's magnetic properties. This approach is motivated by the role of the transition ion in the $FePO_4$ crystal. Hence, the feasibility of a state of charge sensor concept based on magnetic principles is investigated by an experimental determination of the concomitant change of the magnetic susceptibility of the $LiFePO_4$ electrode during/charging.

Kurzfassung

Lithium-Ionen-Batterien sind mittlerweile weitverbreitete Energiespeicher für zahlreiche batteriebetriebene Anwendungen. Besonders im Bereich von Hochleistungsanwendungen, wie zum Beispiel elektrische Antriebe im automotiven Bereich oder stationäre Energiespeicher in regionalen Verbrauchernetzen, hat sich Lithiumeisenphosphat ($LiFePO_4$) als vielversprechendes Kathodenmaterial für Lithium-Ionen-Batterien etabliert. Begründet wird dies durch die gute Verfügbarkeit der Rohstoffe, die damit verbundenen moderaten Herstellungskosten sowie die herausragende thermodynamische Stabilität. Letztere ist im Speziellen für die Automobilindustrie von großer Bedeutung, da von $LiFePO_4$-Batterien, im Gegensatz zu anderen Lithium-Ionen-Zellchemien wie z.B. $LiCoO_2$, im Falle eines Verkehrsunfalles ein geringes Gefährdungspotenzial ausgeht. Des Weiteren weisen $LiFePO_4$-Batterien eine hohe spezifische Leistungsdichte auf und werden daher bevorzugt in elektrischen Hybridfahrzeugen eingesetzt.

Nachteilig im Gebrauch von $LiFePO_4$-Batterien erweist sich jedoch der für diese Zellchemie charakteristische Verlauf der Zellruhespannung. Dies wird durch die Tatsache begründet, dass die Einlagerung/Verarmung von Lithium-Ionen in der $LiFePO_4$-Elektrode über weite Bereiche des möglichen Ladungszustandes anhand eines Zweiphasenprozesses stattfindet. Folglich weist die Zellspannung einen sehr flachen Verlauf in Abhängigkeit des Ladezustandes auf. Des Weiteren ist die Zellspannung signifikant von einem Hystereseeffekt beinflusst, was vermutlich mit dem Auftreten mehrfacher thermodynamischer Gleichgewichte in der $LiFePO_4$-Elektrode zusammenhängt. Zusammenfassend muss angemerkt werden, dass die Abbildung des Ladezustandes auf die Zellspannung nicht eindeutig ist und stark von der Ladehistorie abhängt. Entsprechend schwierig ist es, den nicht messbaren Ladezustand der Batterie mithilfe der etablierten Methoden zu bestimmen, was in der Regel nur ungenau gelingt.

In der vorliegenden Arbeit soll der Ladezustand von $LiFePO_4$-Batterien exakt bestimmt werden, wofür zwei grundverschiedene Ansätze verfolgt werden. Der erste Ansatz beruht im Wesentlichen auf der Zustandsschätzung mit Hilfe von Bayesscher Statistik. Dabei wird die Mehrdeutigkeit in Zusammenhang mit der Zellruhespannung im Zuststandsraummodell integriert, und mit Hilfe einer sequenziellen Monte-Carlo-Methode werden der zeitliche Verlauf der Zustände, sowie der Modellparameter simulatan ermittelt. Alternativ basiert der zweite Ansatz auf der grundsätzlich neuen Idee, den Ladezustand mit den magnetischen Eigenschaften des Kathodenmaterials zu korrellieren. Dieser Ansatz ist im Wesentlichen durch die Rolle des Übergangsmetalls im $FePO_4$-Kristall begründet. Die Realisierbarkeit eines Ladungssensors, basierend auf der Bestimmung der magnetischen Materialeigenschaften des $LiFePO_4$-Kathodenmaterials, wird in dieser Arbeit anhand einer Machbarkeitsstudie untersucht. Folglich wird der Zusammenhang zwischen Lithierungsgrad und der magnetischen Suszeptibilität der $LiFePO_4$-Elektrode experimentell nachgewiesen und die benötigte magnetische Sensitivität eines entsprechenden Sensors bestimmt.

Acknowledgement

I'd like to express my deepest gratitude to following people for the guidance, support and encouragement I've received during the work with this thesis.

First I want to thank my supervisor Univ.-Prof. Dipl.-Ing. Dr.techn. Georg Brasseur for the scientific guidance as well as the freedom in the formulation of the topic.

Further I'm deeply thankful for the guidance I received from Univ.-Prof. Dr.phil. Heinz Krenn, who supported me with his extraordinary expertise in the field of magnetometry. His great commitment enabled the experimental evaluation by means of SQUID magnetometry. I very much appreciate his great enthusiasm with the topic.

I'm also very grateful to Assoc.Prof. Dipl.-Ing. Dr.techn. Roland Fischer, who inspired me to investigate the problem from the magnetic point of view. Moreover, his support by preparing samples enabled the experimental investigation of the battery's magnetic properties.

I also want to express special thanks to Stefan Lauterbach, who also provided samples for the experimental evaluation in the lab and supported me during these experiments.

Further I want to thank Dipl.-Ing. Dr.techn. Bernhard Schweighofer for providing me the current profiles of the driving cycles used in this thesis.

Finally, I wish to express my gratitude to the government of Styria for the financial support by funding the project "LIFE - SOC and SOH estimation for $LiFePO_4$ based batteries".

Contents

1. Introduction

1.1. Motivation

In the past few years, an increasing demand for portable energy storage systems has emerged. This is due to the fact that the markets for both portable consumer electronics as well as automotive high-power applications have steadily risen.

There were major achievements in the field of pervasive computing and the gradually extending infrastructure of information technology enables to continuously extend the field of applications for portable consumer electronics. Furthermore, the development of a middle class in emerging countries entailed a significant increase of sales figures for portable consumer electronics.

With respect to high-power automotive applications, the steadily increasing market share of e-mobility is not only caused by increasing wealth or the achievements of electric vehicle drive trains in recent years, but also by political reasons. Governments of developed and emerging countries face growing pressure to reduce CO_2 emissions as well as the constantly increasing air pollution in urban regions. It is a well-known fact that the traffic based on conventional mobility technologies significantly contributes to these emissions. Consequently, attention is drawn to find alternatives to the established mobility concepts based on conventional combustion engines. The field of e-mobility as a whole is nowadays generally accepted as such an alternative. Unfortunately, the energy storage is still one of the limiting factors which hampers the changeover from combustion engines to electric drive trains. Thus, it is not surprising that mobile energy storage systems have recently been subject of intense research.

By extending the field of applications for portable energy storage systems, also the requirements to the energy storage have grown with respect to storage capacity, specific power, safety and lifespan. Among the electrochemical energy storage systems, lithium ion (Li-ion) batteries proved to be the most promising candidates to meet the higher requirements. Hence, it is not surprising that the majority of electric vehicles nowadays utilize a storage system based on lithium ion technology. Equipped with such a battery system, the range of electric vehicles today reaches almost the scale of vehicles using conventional combustion engines.

First introduced in 1976 by Whittingham [1], extensive research efforts were made of the lithium ion technology to improve the storage capacity and broaden the range of applications toward more-energy consuming applications. Due to emerging markets of high-power automotive and storage applications, the available power became a significant parameter in the design of energy storage systems. Lithium ion technology turned out to be suitable to design both high-power and high-energy batteries, which is shown in the Ragone chart in Figure 1.1.

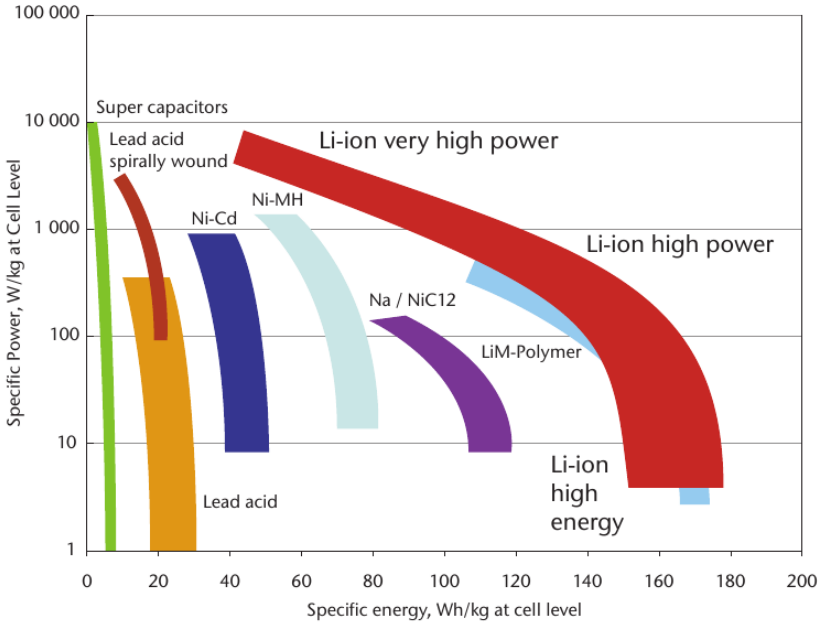

Figure 1.1.: Ragone chart comparing different rechargeable battery technologies with respect to specific power and specific energy. Modified from [2].

A key element which mainly determines the performance of a lithium ion battery is the active material of its positive electrode. Layered structures (e.g. $LiCoO_2$) are preferably used for high-energy batteries, while spinel oxides and olivines ($LiMPO_4$, M = Fe, Mn, Co or Ni) are considered as positive electrode active material for high-power systems [3]. Among the olivine cathode materials, lithium iron phosphate ($LiFePO_4$) is nowadays widely used in storage systems for high-power automotive applications. In addition to the distinctive specific power, $LiFePO_4$ batteries provide a feature which is of significant relevance for automotive applications. Due to the strong P-O bounds in $LiFePO_4$ positive electrode material, oxygen is prevented from internal release. In case of a battery's abuse, a thermal runaway is therefore less likely and thus associated with much less exothermic energy [4,5]. This circumstance proves to be of great importance since a persistent risk of mechanical deformation of the energy storage induced by traffic accidents exists in automotive applications.

Moreover, economical reasons suggest the usage of $LiFePO_4$ for high energy-consuming applications. The active material of the positive electrode contributes most to a battery's total mass and as a consequence also to the production costs. Compared to expensive active materials like e.g. $LiCoO_2$, $LiFePO_4$ shows high availability of excellent raw material and can be produced inexpensively.

So far, only the electrochemical and economical benefits of $LiFePO_4$ active material were pointed out. However, some problems arise from the user's perspective. Due to the characteristic potential of the $LiFePO_4$ electrode, the task of condition monitoring, for example estimating the state of charge (SOC) or the state of health (SOC), is extremely challenging. Especially for hybrid electric vehicle drive trains, this circumstance proves to be crucial. With respect to battery management, the SOC is a key quantity for battery management systems (BMS) and is not only required to quantify the stored energy level but also to provide maintenance tasks like cell balancing. The necessity for the latter arises from the fact that high-power bat-

tery systems consist of a large number of individual batteries which are connected in serial and parallel configurations.

Unfortunately, these individual batteries tend to wear out in an unbalanced manner. On the one hand, the temperature distribution in the battery system is not completely uniform, causing batteries to wear out faster when operated at higher temperature levels. On the other hand, the individual batteries differ slightly with respect to the electrochemical properties due to production tolerances and are therefore characterized by slightly different storage capacities. The impact of the mismatch of the storage capacities is best illustrated by an example. Consider the case of an energy storage system consisting of several mismatched batteries being connected in serial. During the operation, the mismatch of the individual storage capacities results in the situation that batteries with lower storage capacity perform at higher cycle rates. As a consequence, the weaker batteries wear out faster, which in turn further increases the mismatch of the storage capacities. Hence, this effect is self-increasing. In the worst case, individual batteries are operated at critical cell voltages (under- or overcharging). In any case, these batteries are destroyed, and in the case of overcharging, an immanent safety risk exists.

In order to circumvent this problem, it is necessary that battery management systems equalize the charge levels of the individual batteries from time to time. However, in order to efficiently provide this measure, battery management systems require an accurate estimate of the SOC of each individual battery. As mentioned before, in case of $LiFePO_4$ batteries, the determination of this quantity is challenging.

1.1.1. State of the Art in State of Charge Estimation

As already mentioned above, the battery's SOC is a key quantity and inter alia required by battery management systems to efficiently provide maintenance tasks. Since the SOC of a battery cannot be measured directly, it must be inferred from a directly accessible quantity.

Usually, the SOC of a battery is defined as the stored charge level normalized by the battery's storage capacity. Hence, the most intuitive approach is to simply integrate the battery's operating current and to normalize the result by the storage capacity. This approach is known as coulomb counting and causes two fundamental problems. Firstly, the initial condition must be known a priori. Secondly, the accuracy of the estimate decreases progressively. This circumstance is due to the fact that coulomb counting is an open loop method and consequently very prone to systematic errors of the current measurements. If the result of an operation mode is that the battery's end-of-charge voltage is periodically reached, e.g. by charging portable consumer electronics or electric vehicles, the estimate of the SOC can easily be corrected by $SOC = 1$ and the shortcomings associated with coulomb counting are of minor impact.

However, the situation is different if the battery is used for temporarily buffering smaller energy quantities. For example, consider the energy storage in a hybrid electric vehicle drive train. Depending on the control strategy, the battery is alternately used to provide the electrical power needed for acceleration or for recuperating the vehicle's kinetic energy during braking. Consequently, the SOC oscillates around a specific operating point. In this operation mode, the systematic error of the current measurements is of great relevance for the accuracy of the SOC estimate derived by

coulomb counting. This is caused by the integration of the bias component of the current measurement's systematic error. Thus, the deviation of the SOC estimate increases steadily.

In order to overcome the shortcomings of the coulomb counting method, it is desirable to incorporate a feedback path in the SOC estimator. Since the electrode potentials relate to the SOC, the battery's terminal voltage can be used for inference. However, due to the transport kinetics of the charged species, the battery's terminal voltage is not solely a static function of the SOC but also exhibits a transient contribution, depending on the operating current and the temperature, to name but a few. Consequently, the battery is treated as dynamic system and the SOC can be derived by state estimation techniques. The majority of reviews of SOC estimation in battery systems can be classified by means of the dynamic models used for the state inference.

The most immediate approach is to derive a dynamic model based on the underlying electrochemical principles. Unfortunately, due to the high complexity of the transport kinetics, this way of modeling proves to be extremely challenging and usually leads to a set of nonlinear coupled partial differential algebraic equations. In order to reduce the computational demands, dynamic battery models constructed by electrochemical principles usually consider only the dynamics along the axis perpendicular to the electrode/separator boundary surface (1D-spatial model). A common simplification is done by treating the particles of the battery's active material as spheres of a known diameter and to model the concentration of the charged species in the electrodes by single particle models [6–10]. Alternatively, dynamic models derived by equivalent circuits provide a much simpler set of equations. In contrast to electrochemical models, in most cases, one deals with linear ordinary differential equations. Hence, it is not surprising that equivalent circuit models are the most adopted models in practice. Various types of equivalent circuit models exists, and the majority of these models are of the same origin. Randels published an equivalent circuit modeling the kinetics of electrode reactions in 1947 [11]. This model is still the basis for equivalent circuit models nowadays. An overview of the most adopted equivalent circuit models can be found e.g. in [12–14]. For the sake of completeness, it should be mentioned that some authors proposed black-box models derived by artificial neural networks [15, 16] or fuzzy logic [17–19].

The diversity among the algorithms used for estimation is seldom pronounced. The majority of reviews of SOC estimation, extended Kalman filtering or unscented Kalman filtering is used for the state estimator. Since the dynamics of modern battery systems is usually not entirely modeled by the models used for state inference, adaptive approaches are increasingly becoming popular [20]. In most cases, a low order equivalent circuit model is used for the state inference by means of Kalman filtering and the parameters of the model are tracked by a recursive leasts square or a least mean squares estimator in order to cope with the battery's nonlinear dynamics [21, 22].

However, the performance of the SOC estimator strongly depends on the mapping between the SOC and the battery's open circuit voltage U_{OCV}. If charging/discharging entails a significant alternation of the open circuit voltage U_{OCV}, e.g. in the case of $LiCoO_2$ or $LiMn_2O_4$ batteries, the SOC can be estimated accurately by state inference incorporating the battery's terminal voltage. Unfortunately, this is not the case for $LiFePO_4$ batteries, since the mapping between the SOC and the battery's open circuit voltage is in wide ranges extremely flat and strongly influenced by hysteresis phenomena. As a consequence, the inverse mapping covers a long range of the possible SOC range, causing state-of-the-art SOC estimation methods to fail.

Hence, it is the goal of this thesis to investigate two different methods to determine the SOC of $LiFePO_4$ batteries. Firstly, a joint estimation framework is introduced, incorporating the transition of the open circuit voltage U_{OCV} induced by the hysteresis phenomena. Secondly, the feasibility of a radically different approach aiming to correlate the SOC with the magnetic properties of the positive electrode's active material is analyzed.

1.2. Definitions

Some terms are defined in several ways in the literature. Before proceeding with the electrochemical principles of $LiFePO_4$ batteries, the following terms should be clarified first.

Open Circuit Voltage

Throughout this thesis, the battery's open circuit voltage U_{OCV} is defined as the battery's terminal voltage at zero load after a theoretically infinite settling period. In other words, the battery's electrodes are assumed to be in the state of thermodynamical equilibria.

As mentioned before, the open circuit voltage U_{OCV} is greatly influenced by hysteresis phenomena. In this context, the open circuit voltage hysteresis defines the voltage gap between the open circuit voltage charge and discharge curve at the same charge level. The open circuit voltage charge and discharge curves are defined as the open circuit voltage U_{OCV} obtained by fully charging and fully discharging, respectively.

Nominal Capacity

Manufactures usually state the battery's nominal capacity C_n as a minimum guaranteed or typical value. In this thesis, as opposed to the name, the nominal capacity C_n denotes the maximum charge which can be stored in the battery.

State of Charge

Similar to the nominal capacity, the SOC is often defined as the normalized remaining charge level retrievable at certain load conditions. Hence, the SOC denotes the theoretically retrievable charge level normalized by the nominal (maximal) capacity. Consequently, $\mathrm{SOC} = 1$ and $\mathrm{SOC} = 0$ relate to the maximum and minimum values of the open circuit voltage charge and discharge curve, respectively.

1.3. The Lithium Iron Phosphate Battery

In this thesis, methods for determining the SOC of $LiFePO_4$ batteries are investigated. As already mentioned in the previous section, the task of determining the SOC by measurements of the battery's terminal U_{term} voltage proves to be challenging. This is due to the $LiFePO_4$ battery's characteristic mapping between the SOC and the open circuit voltage U_{OCV}. This section provides an brief overview of the phenomena associated with the open circuit voltage of $LiFePO_4$ batteries. However, it should be mentioned that this section (as well as the entire thesis) only touches upon the electrochemical principles associated with lithium insertion/depletion in batteries of this chemistry.

1.3.1. Working Principle

The working principle of rechargeable lithium ion batteries is based on the conversion between electrical and chemical energy regarding the redox reactions between a ionic-connected negative host electrode and a positive electrode[1] containing the charged species (lithium ions). In simplified terms, the working principle can be summarized as follows: During charging, a surface overpotential is applied to the electrodes, which implies that lithium ions are progressively depleted from the positive electrode's active material and move towards the negative electrode where they finally enter the host particles. Thus, the transport kinetics is influenced by the imposition of the electric potential difference between the electrodes (migration), the concentration gradient of solved lithium ions (diffusion) and bulk fluid motion (convection) [23]. As a consequence, the electric potentials of the electrodes change in such a way that the negative electrode's potential is decreased, whereas the positive electrode's potential is raised. This process is accompanied by the oxidation of the particles of the active material of the positive electrode and the reduction of the host particles of the negative electrode, which is associated with an external current density. The discharge process takes place in reverse order.

In the case of the battery chemistry investigated here, carbon (C_6) and $LiFePO_4$ serve as active material of the negative and positive electrode, respectively. Consequently, the redox equations of the reaction couples are given by

$$\mathrm{Li_0FePO_4 + yLi^+ + ye^- \overset{\text{discharge}}{\underset{\text{charge}}{\rightleftarrows}} Li_yFePO_4}, \tag{1.1}$$

$$\mathrm{Li_xC_6 \overset{\text{discharge}}{\underset{\text{charge}}{\rightleftarrows}} Li_0C_6 + xLi^+ + xe^-}. \tag{1.2}$$

Figure 1.2 schematically illustrates the working principle of the battery by an arrangement of a C_6 and $LiFePO_4$ electrode being surrounded by an electrolyte.

[1] In electrochemistry, it is common to denote the oxidizing electrode anode and the reducing electrode cathode. In the case of rechargeable batteries, this definition can be quite misleading since the electrodes change the role of reaction in dependence of the current direction. Therefore, it is common practice to define the terms anode and cathode from the perspective of an energy source. For the sake of simplicity, anode and cathode are in this thesis denoted as negative and positive electrode, respectively.

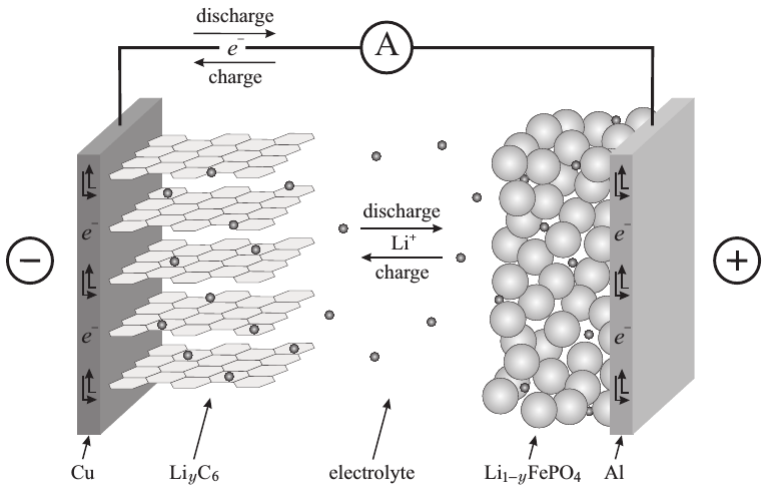

Figure 1.2.: Illustration of the working principle of an $LiFePO_4$ battery [24]. While charging Li^+-ions are detached from the $LiFePO_4$ particles and intercalate in the C_6 electrode. This is followed by the reduction of the C_6 particles of the negative electrode and the oxidation of the iron atom in the remaining $FePO_4$ crystal, which is associated with the current in the external circuit. The discharge process takes place in reverse order.

Let us take a closer look at the structure of the $LiFePO_4$ battery. Both electrodes possess a porous structure and are composed of a compound of particles of active material, binder and filler additives being coated on electrically well conducting metal foils. The metal foils are used to apply the surface overpotential to the electrodes' active material and to provide the external exchange current density by the external electric circuit. Hence, these metal foils are often denoted as current collectors. In lithium ion batteries, copper and aluminum are prevalently used for the current collector of the negative and positive electrode, respectively. The binder and filler particles are electrochemical inactive additives. Nevertheless, these materials are of great importance since they minimize the mechanical strain induced by the volume expansion associated with the lithium insertion in the active materials.

According to the redox equations shown above, C_6 and $LiFePO_4$ serve as intercalation[2] material for the negative and positive electrode, respectively. In order to minimize diffusion paths, the electrodes are structured as many-particle systems with an active material's particle size between 20 and 100 nm [25]. However, pure $LiFePO_4$ nanoparticles are not suitable for the use as active material in insertion batteries. The reason for that is that the electric conductivity of $LiFePO_4$ is too low to provide acceptable charging rates. In order to circumvent this problem, the $LiFePO_4$ nanoparticles are coated with an additional carbon layer. This measure significantly increases the electric conductivity within the structure of the positive electrode. Consequently, the surface overpotenial can be applied to a much larger number of $LiFePO_4$ particles.

In order to enable the transport of the charged species, an electrolyte is required. In most cases, the liquid electrolyte consists of $LiPF_6$ as conduction salt and an organic solvent. The solvent is often a combination of a linear and a cyclic carbonate (e.g. ethylene carbonate and dimethyl carbonate) which provide a better ionic

[2]Intercalation denotes a reversible inclusion or insertion of molecules or ions into a host system.

conductivity and a better formation of the solid electrolyte interphase (SEI) [26]. Nevertheless, the ionic conductivity is poor compared e.g. to aqueous electrolytes. Hence, the stretches of the ionic transport must be minimized to achieve acceptable charging rates. Consequently, the electrodes are stacked, only separated by an electrically isolating but ionic conducting separator membrane.

As indicated above, the ability of a good solid electrolyte interphase (SEI) formation is an essential decision criteria for the choice of the electrolyte. The quality of the SEI is essential for the function and lifespan of lithium ion batteries.

This circumstance is due to the fact that the operation of lithium ion batteries is actually far beyond the thermodynamical stability limits of the organic electrolyte. During initial charging, decomposition of the organic electrolyte occurs in the vicinity of the negative electrode. The products of decomposition adhere to the surface of the graphite particles and, thus, form a passivation layer which prevents the electrolyte from further decomposition. This passivation layer is known as solid electrolyte interphase which is due to the fact that the SEI is formed between the solid intercalation material and the liquid electrolyte and acts as an intermediate phase. The SEI consists of two films. The first consists of organic decomposition products and forms a thick and porous layer being permeable for the electrolyte. The second thin film is of inorganic decomposition products and electrolyte-impermeable [27]. Figure 1.3 schematically illustrates the composition and function of the SEI.

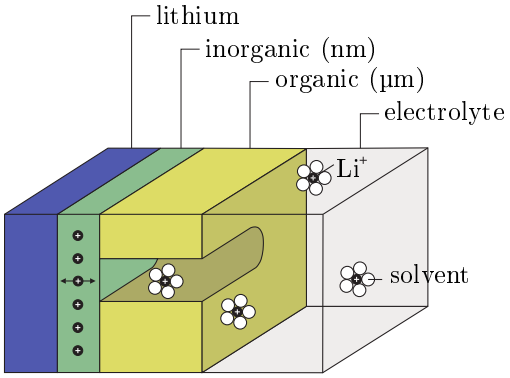

Figure 1.3.: Schematic illustration of the passivating surface film denoted as solid electrolyte interphase (SEI) on the negative electrode formed by products of decomposition of the organic electrolyte. Modified from [27].

Since the quality of the formation of the SEI is crucial for the performance and the lifespan of the battery, the formation of the SEI is provided by the manufacturers by means of initial cycling. Hence, lithium ion batteries are always dispatched in a charged condition.

1.3.2. Open Circuit Voltage Characteristics of $LiFePO_4$ Batteries

As previously stated, the $LiFePO_4$ battery's open circuit voltage U_{OCV} proves to be problematic if the task is to determine the SOC by means of voltage measurements. Hence, let us take a closer look at the phenomena which are associated with the open circuit potentials of the insertion electrodes in $LiFePO_4$ batteries.

The open circuit voltage of batteries utilizing $LiFePO_4$ active material shows an in wide ranges flat dependence on the SOC, which is characterized by three voltage plateaus. Additionally, hysteresis phenomena significantly influence the open circuit voltage U_{OCV}. See, for example, the experimentally determined open circuit voltage characteristic of an A123 26650m1B $LiFePO_4$ battery shown in Figure 2.1 in chapter 2. Since the terminal voltage U_{term} of a battery equals the difference of the potentials of the positive and the negative electrode, the course of the open circuit voltage U_{OCV} can be deduced by investigating the electrode potentials separately.

Negative Electrode Potential

As mentioned above, lithium ion batteries prevalently use graphite as intercalation material in the negative electrode. Depending on the order of the crystal structure, it is distinguished between hard and soft carbon graphite. Since this introducing chapter does not claim to provide an in-depth treatment of the electrochemical phenomena in lithium ion batteries, only the prevalent case of hard carbon graphite is described.

The crystal structure of hard carbon graphite insertion material is characterized by a layered lattice. The layers are formed by a planar network of carbon atoms which are symmetrically ordered in hexagonal patterns and the layers are arranged in such a way that every second layer is displaced by half of the crystallographic spacing. Consequently, this configuration minimizes electrostatic repulsion since every carbon atom points at the neighboring planes in the center of a hexagonal pattern. In the literature, this (prevalent) structure of graphite is denoted as AB configuration. Less common is the rhombohedral structure known as ABC configuration.

The three-dimensional structure is evoked by the van der Waals force. Consequently, the bound between the layers is relatively weak, which is beneficial for the intercalation of lithium ions between the layers. As a consequence, the lithation of the positive electrode is accompanied by a significant volume expansion of the graphite particles. The order in which layers in the graphite particle are filled first with lithium ions is defined by the staging mechanism which is schematically illustrated in Figure 1.4. The staging mechanism can be deduced from the energy which is required to "open" a new gap for intercalation. As depicted in Figure 1.4, the LiC_x stoichiometry of the stages I, II, III and IV is given as LiC_6, LiC_{12}, LiC_{18} and LiC_{30}, respectively. However, due to safety reasons stage IV is usually not reached in battery systems.

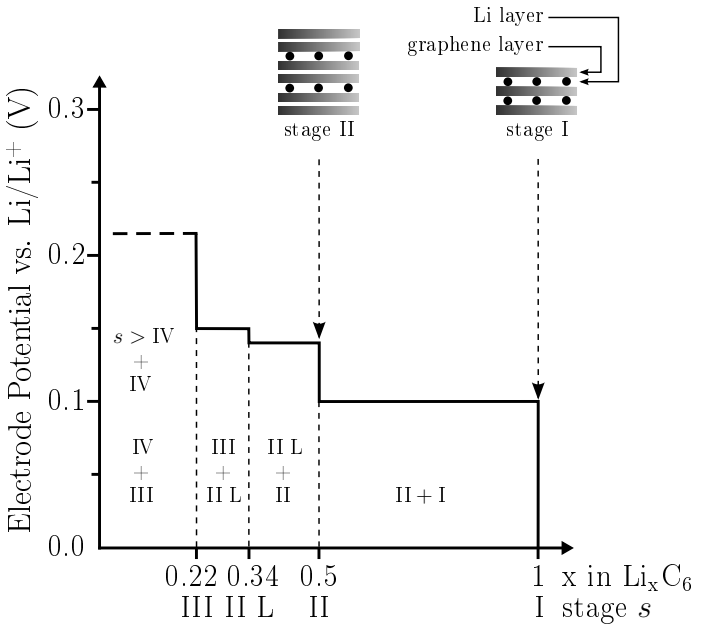

Figure 1.4.: Stage formation of a hard carbon graphite electrode potential versus a lithium reference electrode in the case of lithium intercalation induced by a small and constant current. Modified from Winter et al. [28].

In practice, the electrode potential of the negative electrode does not entirely match with the course shown in Figure 1.4. However, the characteristic plateaus of the battery's open circuit voltage U_{OCV} are caused by the staging phenomenon of the negative electrode.

Positive Electrode Potential

The reason why the voltage plateaus of the C_6 electrode are so remarkable in the $LiFePO_4$ battery's open circuit voltage characteristics is that the electrode potential of the positive electrode remains in wide ranges nearly constant. This is due to the positive electrode's flat potential profile which was identified in several reviews by a two-phase reaction with $LiFePO_4$ and $FePO_4$ end members (see e.g Matsui et al. [29] or Zaghib et al. [25]). The review of Zaghib et al. gives a good overview of the phenomena associated with the lithium insertion in olivine-based lithium batteries and was used as a basis for the following explanations.

For example, consider an intercalation electrode where a solution of guests intercalates in a host lattice. The potential variation of the redox couple in the host lattice in dependence of the composition x is given by

$$V(x) = -\frac{1}{zF}\frac{\partial(\Delta G)}{\partial x} + \text{const.} \tag{1.3}$$

where z denotes the number of electrons involved in the reaction, F the Faraday constant and ΔG is the variation of the Gibbs energy[3] of the system. Gibbs' phase

[3]In thermodynamics, the Gibbs energy denotes a thermodynamic potential which is used to

rule states that if a closed system is in the state of an thermodynamical equilibrium, the number of degrees of freedom of the system f is related to the number of independent components c, the number of phases p and the number of intensive variables n according to

$$f = c - p + n. \tag{1.4}$$

In the present case, $c = 2$ since the positive electrode can be treated as a binary system consisting only of $FePO_4$ and $LiFePO_4$. In electrochemical systems, the intensive variables are always pressure and temperature, hence $p = 2$. By further assuming isobar and isothermal conditions for experiments in the lab, the expression for the system's number of degrees of freedom simplifies to $f = 2-p$. Consequently, if only one phase exists in the host particle, the associated potential varies depending on the guest concentration. By contrast, if two phases are present in the host particle, the electrochemical potential is invariant with respect to the concentration of the guest species. Figure 1.5 schematically illustrates this circumstance with α and β denoting the width of the according single phase regions [30].

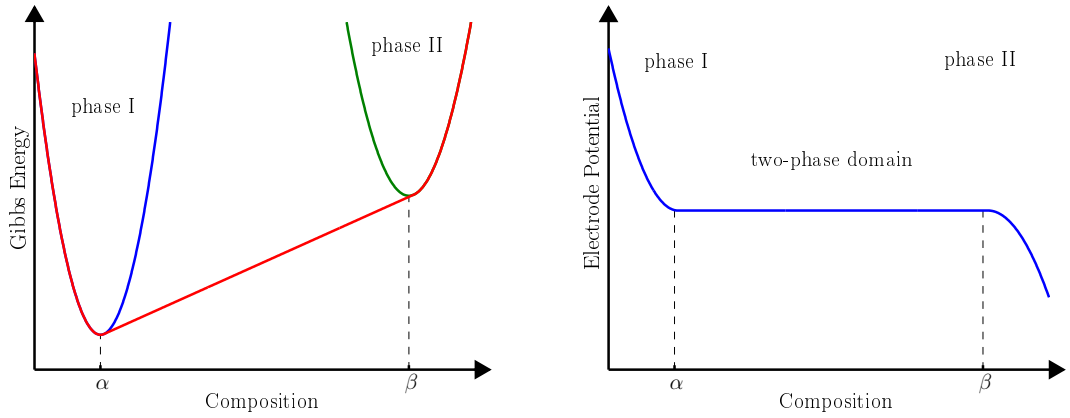

Figure 1.5.: Schematic illustration of the Gibbs' phase rule for a bulk two-phase system. The Gibbs energy depending on the guest concetration in the host lattice is shown on the left. The according electrode potential derived from the Gibbs energy is depicted on the right. Modified from Zaghib et al. [25].

It is a proven fact, that insertion/depletion in $LiFePO_4$ bulk material proceeds according to a two-phase process. Hence, the width of the nearly constant electrode potential is directly related with the width of the two-phase regions. As a consequence, the size of the host particles has an great influence on the width of the voltage plateau. This circumstance is in agreement with the review of Yamada et al. [30], in which a shrinking two-phase region was observed for nanoparticles.

The fact that the two-phase region dominates the insertion/depletion of lithium ions not only in the bulk material but also in nanoporous $LiFePO_4$ multi-particle

express the reversible work which may be performed by a thermodynamical system on isobar and isothermal conditions.

electrodes was confirmed by several reviews of this topic. However, the exact mechanism of insertion/depletion at the nanoscopic scale has not yet been fully understood and is still subject of intense research efforts.

The controversy within the scientific community encompasses at least four models of the insertion/depletion mechanism of the charged species which more or less coexist nowadays.

Among these models, the core-shell model (also known as shrinking core model) presented by Padhi et al. [31] was the first promising candidate to model the problem. Padhi and coworkers proposed the transportation of the lithium ions proceeds by an intercalation process depending on the radius of the host particle. With progressive delithation of the host particle, the $LiFePO_4/FePO_4$ interphase is assumed to move inwards as the outer region converts to the $FePO_4$ phase to incorporate the diffusion-limiting character of the $LiFePO_4$ electrode in the model. A slightly modified version of the core-shell was proposed by Andersson and Thomas [32] denoted as mosaic model, which considers the feasibility that the lithium ions intercalate/deintercalate at many sites of the Li_xFePO_4 nanoparticles.

Later, the core-shell model was adopted by Srinivasan and Newman [33], who demonstrated an asymmetry between the insertion and depletion process. The in situ X-ray diffraction study provided by Shin et al. [34] confirmed this circumstance. However, they reported that the results obtained in the lab are "significantly smaller than those predicted by the model." Hence, they concluded that the core-shell model may be inappropriate to model the behavior of the $LiFePO_4$ electrode.

A short time thereafter, based on experiments by means of electron loss spectroscopy and transmission electron microscopy, Laffont et al. [35] reported that Li_xFePO_4 nanoparticles always consist of an $FePO_4$ core, independent of the charging history. Based on their observations, they proposed the radial core-shell model, which is an anisotropic modification of the classical core shell model. The radial core-shell model takes into account that the insertion of the lithium ions starts at the edges of the particle but during delithation, the lithium ions are extracted from the middle first.

In 2008, Delmas et al. [36] surprised with a completely different approach which was derived by a X-ray diffraction and a high resolution transmission electron spectroscopy study, respectively. The results of the first study essentially confirmed the two-phase transformation, whereas the high resolution transmission electron spectroscopy study offered surprising results since the Li_xFePO_4 proved to either be fully lithated or fully delithated. Based on these results, Delmas and coworkers developed the domino-cascade model, which basically models the deintercalation process by a transversal elastic wave moving along the a-direction of the olivine Li_xFePO_4 crystal, while the lithium ions migrate along the b-direction. In their review, they explained that the elastic wave accelerates the phase transition by accelerating the displacement of the $LiFePO_4/FePO_4$ boundaries. They further remarked that "at the agglomerate scale, a core-shell is likely to occur." In 2011, Brunetti et al. [37] presented a study based on precession electron diffraction which essentially confirms the domino-cascade model presented by Delmas and coworkers.

Strongly linked to the insertion/depletion mechanism in the $LiFePO_4$ electrode is the phenomenon of open circuit voltage hysteresis. Unfortunately, since the insertion/depletion mechanism has not yet been entirely understood, it is not surprising that there are only a few reviews of this topic available. The controversy within the scientific community encompasses two different causes for the voltage gap between the charge and discharge potential of the $LiFePO_4$ electrode.

For example, the review Matsui et al. [29] concluded that the voltage gap between the charge and discharge potential may be caused by phases with extremely slow relaxation at the late stage of the electrochemical reaction for both the insertion and the depletion process. Furthermore, they proposed that the thermodynamical equilibrium may was not reached at the moment the open circuit voltage was sampled. In contrast to this theory, Dreyer and coworkers [38,39] presented an approach which is based on the presence of multiple thermodynamical equilibria, corresponding to the number of particles involved. They further claimed that the presence of these multiple thermodynamical equilibria is characteristic for all multi-particle insertion electrodes.

1.4. Contributions

As stated previously, the open circuit voltage characteristics of $LiFePO_4$ batteries prove to be crucial if the task is to determine the SOC of these batteries. This circumstance entails that the majority of state-of-the-art SOC determination methods exhibit poor performance. Therefore, the thesis focuses on this problem, whereby two approaches based on completely different principles are investigated.

The first approach is premised on Bayesian filtering and utilizes measurements of the operating current and the terminal voltage for state inference. Thereby, attention is drawn to the ambiguous mapping between the SOC and the open circuit voltage U_{OCV}. Based on experiments investigating the open circuit voltage characteristics of $LiFePO_4$ batteries, a dynamic model incorporating the influence of open circuit voltage hysteresis was developed. The hysteresis model enables not only to distinguish between the open circuit voltage charge and discharge curves but also models the transition of the open circuit voltage between the 2 curves, which is the case in applications which rely on small charge and discharge quantities. Hence, the ambiguous mapping between the SOC and the open circuit voltage is tackled by means of an additional nonlinear integrating state. Since the parameters of the used dynamics model are not known a priori, a sequential Monte Carlo method was utilized to estimate the states (and thus the SOC) and the model parameters simultaneously [40].

The second approach is based on the change of the battery's electromagnetic properties accompanied by charging/discharging. In an early stage, a change of the electric conductivity of the battery's negative electrode was suspected. A first experimental evaluation obtained promising results since the inductance of an air coil attached to an $LiFePO_4$ battery showed a nearly linear dependence on the SOC [41]. It turned out later that the change of inductance arose most likely due to the experimental setup as the sensitivity of the available measurement equipment was much too low to detect the alternation of the electromagnetic properties. The search for better equipped lab facilities concluded with a cooperation with the Institute of Physics at the University of Graz. By means of a there available superconducting

quantum interference device (SQUID) magnetometer, 2 studies were performed. In a first step, the magnetic moment of samples of differently concentrated mixtures of phase-pure $LiFePO_4$ and $FePO_4$ were investigated. The experiment revealed surprising results, since the magnetic moment of the samples with the lower lithium content showed the lower magnetic moment [42]. As mentioned in the previous section, $LiFePO_4$ and $FePO_4$ do not exist in phase-pure form in real batteries. Hence, the experiment was repeated and samples of the positive electrode of 9 identical but differently charged $LiFePO_4$ were extracted. The outcome of this second SQUID study essentially confirmed the results of the first and proved the feasibility to deduce the $LiFePO_4$ battery's SOC from the magnetic properties of the positive electrode [43].

1.5. Outline

The structure of this thesis is as follows: Chapter 2 presents the results of the experimental evaluation of the open circuit voltage characteristics of the investigated $LiFePO_4$ battery type. Based on these results, a model for the open circuit voltage incorporating open circuit voltage hysteresis will be derived.

In chapter 3, a joint estimation approach based on Rao-Blackwellized particle filtering will be described. After a short introducing section, the dynamics of the battery will be modeled by means of open circuit voltage model developed in chapter 2 and the performance of the estimator will be validated by simulations and real measurements.

Chapter 4 deals with a feasibility study for determining the $LiFePO_4$ battery's SOC based on magnetic principles. Therefore, the underlying theory will briefly be presented, followed by the discussion of the results of the 2 performed SQUID studies. Based on these findings, the required magnetic sensitivity of an induction sensor will be evaluated. Therefore, the total alternation of the magnetic **B**-field will be computed for the case of a homogeneous magnetization of a battery-like geometry.

Finally, the shortcomings and advantages of the findings presented in this thesis will be concluded in chapter 5. Additionally, a short outlook will be given which essentially specifies the required measures to successfully determine the SOC of $LiFePO_4$ batteries.

2. Open Circuit Voltage Modeling

As mentioned in chapter 1, the mapping between the SOC and the battery's open circuit voltage U_{OCV} is of significant relevance for the performance of the SOC estimator. Hence, the aim of this chapter is to develop a model of the open circuit voltage U_{OCV} incorporating the ambiguous mapping associated with open circuit voltage hysteresis.

As a requirement, the model of the open circuit voltage must cover the transition of the open circuit voltage U_{OCV} from one open circuit voltage curve to the other depending on charging/discharging. In order to meet this requirement, the open circuit voltage U_{OCV} is modeled not only as a function of the SOC but also as a second charge-dependent quantity. Since the charging history implicitly influences the open circuit voltage U_{OCV}, this quantity is represented by an additional dynamic state denoted as "hysteresis state" x_{H}. Later, it will be focused on the dynamic behavior of the hysteresis state but at this point it is only necessary that x_{H} is of a value between -1 and 1. The model of the open circuit voltage is given by

$$U_{\mathrm{OCV}}(\mathrm{SOC}, x_{\mathrm{H}}) = U_{\mathrm{OCV,avg}}(\mathrm{SOC}) + U_{\mathrm{OCV,diff}}(\mathrm{SOC}) x_{\mathrm{H}} \tag{2.1}$$

where $U_{\mathrm{OCV,avg}}(\mathrm{SOC})$ and $U_{\mathrm{OCV,diff}}(\mathrm{SOC})$ are given by

$$\begin{aligned} U_{\mathrm{OCV,avg}}(\mathrm{SOC}) &= 0.5(U_{\mathrm{OCV,ch}}(\mathrm{SOC}) + U_{\mathrm{OCV,dis}}(\mathrm{SOC})) \\ U_{\mathrm{OCV,diff}}(\mathrm{SOC}) &= 0.5(U_{\mathrm{OCV,ch}}(\mathrm{SOC}) - U_{\mathrm{OCV,dis}}(\mathrm{SOC})), \end{aligned}$$

respectively.

However, the functions $U_{\mathrm{OCV,ch}}(\mathrm{SOC})$ and $U_{\mathrm{OCV,dis}}(\mathrm{SOC})$ are not available in closed form, hence, an experimental determination of these functions is required. For this purpose, the open circuit voltage of an A123 26650m1-B $LiFePO_4$ was investigated. Initially, the battery was fully charged to the specified end-of-charge voltage of 3.6 V using a constant-current constant-voltage charging (CCCV)[1] procedure. To ensure a/an (almost) settled terminal voltage, an idle time of 24 hours was scheduled before performing charge and discharge experiments to obtain the functions $U_{\mathrm{OCV,ch}}(\mathrm{SOC})$ and $U_{\mathrm{OCV,dis}}(\mathrm{SOC})$, respectively.

Unfortunately, due to the long relaxation period (up to 72 hours [44]) of batteries utilizing $LiFePO_4$ active material, the experimental determination of the true open circuit voltage U_{OCV} by measuring the totally relaxed terminal voltage U_{term} is challenging. This circumstance is due to the fact that stepwise charging/discharging followed by the necessary extensive settling period after each charge action leads to an experimental duration for a sufficiently large number of open circuit voltage

[1] CCCV is a common charging procedure for Li-ion rechargeable batteries. Firstly, the battery is charged with a constant current until the battery's terminal voltage U_{term} reaches the end-of-charge voltage. Secondly, the terminal voltage is held constant until the (exponentially decreasing) charging current drops below a certain threshold.

samples over the years. Due to the phenomena of self-discharge and calendrical aging, the uncertainty with respect to the state of charge of the thus obtained measurements would increase with proceeding experimental duration.

In order to circumvent this problem, the battery was charged and discharged with a small constant current. A magnitude of 20 mA proved to be a reasonable trade-off between measurement time and accuracy since the magnitude of 60 mA yield similar results. Therefore, it is reasonable to assume that the transient contribution U_{trans} to the terminal voltage U_{term} and voltage drop across the internal resistance U_R is negligibly small. In order to accelerate the diffusion processes associated with charging/discharging, the experiments in the lab were carried out in a temperature stable cabinet at 40 °C. This measure mainly serves the purpose to minimize contributions to the terminal voltage U_{term} which are not attributable to the open circuit voltage U_{OCV}.

Figure 2.1 shows the measured approximated open circuit voltage charge curve $U_{\text{OCV,ch}}$ (solid) and open circuit voltage discharge curve in dependence of the state of charge[2]. Besides, due to the internal thermodynamical processes, the open circuit voltage U_{OCV} is implicitly influenced by the temperature. However, in the case of the investigated battery, this influence proved to be of minor significance. For instance, the terminal voltage U_{term} of the totally relaxed battery was measured in a temperature stable cabinet at 20 °C and 40 °C. The deviation between these measurements was less than 1.1 mV.

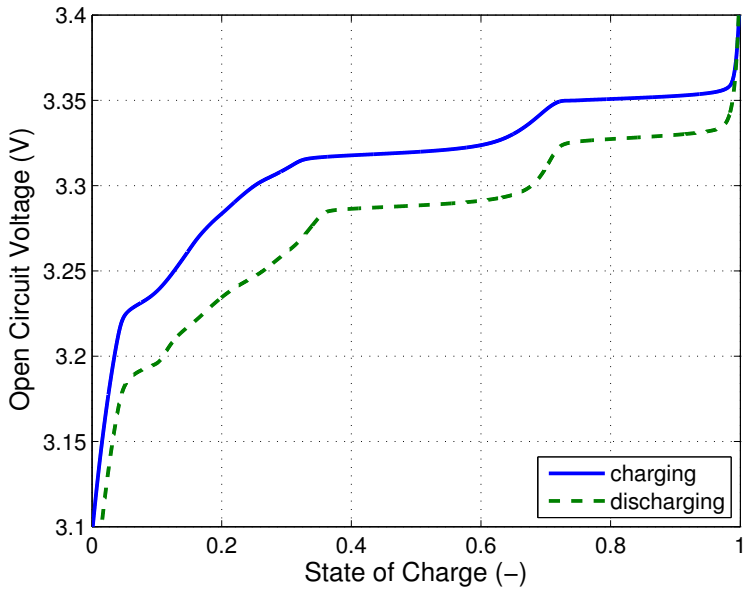

Figure 2.1.: Measured approximated open circuit voltage charge curve $U_{\text{OCV,ch}}$ (solid) and open circuit voltage discharge curve ($U_{\text{OCV,dis}}$) (dashed) of an A123 26650m1-B 2.5 Ah cylindrical $LiFePO_4$ battery.

[2]For reasons of simplicity, the same nomenclature is used for real and the measured approximated open circuit voltage charge and discharge curves. Since the model of the open circuit voltage is based on these curves, the same considerations apply to all functions related to the open circuit voltage model.

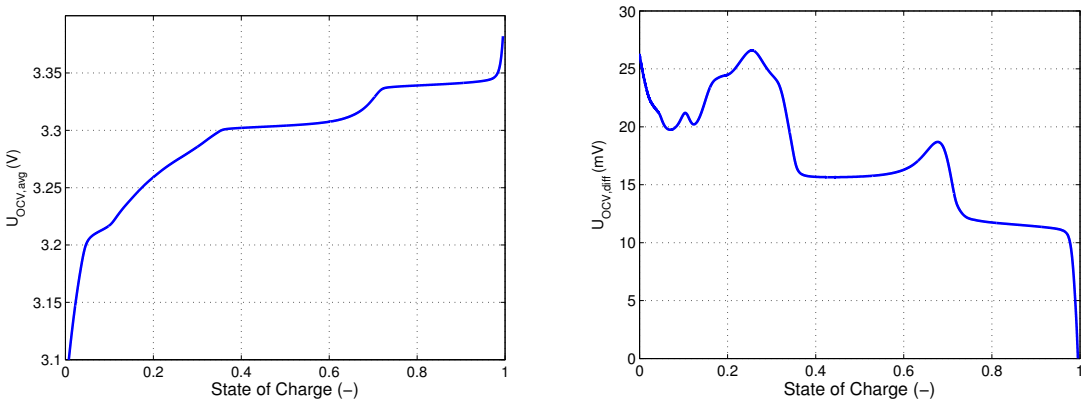

(a) $U_{\mathrm{OCV,avg}}(\mathrm{SOC})$ (b) $U_{\mathrm{OCV,diff}}(\mathrm{SOC})$

Figure 2.2.: Courses of the functions $U_{\mathrm{OCV,avg}}$ and $U_{\mathrm{OCV,diff}}$ in dependence of the SOC. The courses were determined by means of the measured approximated open circuit voltage charge and discharge curves.

2.1. Open Circuit Voltage Hysteresis

In order to complete the modeling of the battery's open circuit voltage, the dynamics of the hysteresis state x_{H} is described in this section. By investigating the battery's open circuit voltage charge and discharge curves, there were indications that the open circuit voltage U_{OCV} proceeds from one open circuit voltage charge curve to the other along an exponential-like function.

Unfortunately, reviews concerning hysteresis phenomena associated with the ambiguous mapping between the SOC and the open circuit voltage U_{OCV} are underrepresented compared to papers investigating the battery's short-term dynamics. This circumstance is not surprising since in order to investigate the mentioned hysteresis phenomena measurements of the open circuit voltage U_{OCV} at different charge levels are required. As mentioned before, these measurements are extremely time-consuming. Nevertheless, in order to investigate the influence of the hysteresis phenomena on the open circuit voltage U_{OCV}, an experimental study was carried out. The results essentially confirm the findings presented in [45].

The hysteresis phenomena were investigated by measuring the open circuit voltage U_{OCV} of nine charge/discharge cycles which are assumed to perform loop-shaped transitions from one open circuit voltage charge curve to the other. Thereby, each loop consists of 13 individual measurements of the open circuit voltage U_{OCV}. As a trade-off between accuracy and experimental duration, a settling time of 24 hours was kept after each individual charge/discharge action before the battery's terminal voltage U_{term} was measured in order to obtain a sample of the open circuit voltage U_{OCV}. By analogy with the investigations in the previous section, the experiments were carried out in a temperature stable environment at 40 °C to accelerate the thermodynamical processes associated with charging/discharging.

However, the problem of the exhaustive settling time proved to be challenging since the experimental duration is mainly determined by this quantity. By neglecting the time span required to charge/discharge the battery with the according state of charge, the time exposure for the experiment with the mentioned configuration is at least 117 days. Unfortunately, this fact evokes a series of problems since it is hard to provide the same experimental conditions over this long period.

Hence, the investigation of the open circuit voltage hysteresis was partitioned into three individual and simultaneously performed experiments. For this purpose, 12 A123 26650m1-B $LiFePO_4$ batteries were tested with respect to their nominal capacity C_n. A subset of three batteries which exposed the smallest difference with respect to the nominal capacity C_n was chosen for the experiment. Figure 2.3 depicts the testing procedure for investigating the hysteresis-related alternation of the open circuit voltage U_{OCV}. Each color represents an individual experiment, consisting of three hysteresis loops. Starting either on the upper or the lower open circuit voltage curve (circular unfilled markers), the batteries were charged (solid line) or discharged (dashed line) in seven steps by a total charge level corresponding to 10% of the battery's nominal capacity C_n. After the last sample (asterisk markers), the current direction was changed and the transition of the open circuit voltage U_{OCV} to the opposite direction was investigated with the same number of samples. For the sake of clarity, it should be mentioned that the loops shown in Figure 2.3 were obtained by simulation. The transition from one open circuit voltage curve to the other was assumed to be completed by taking the last sample, which is why the start and end markers overlap.

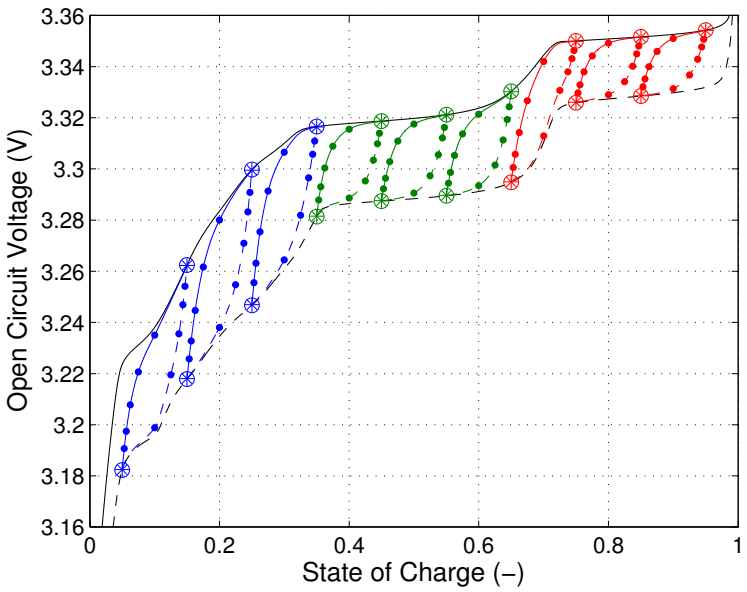

Figure 2.3.: Illustration of the test procedure to investigate the transition of the open circuit voltage U_{OCV} from one open circuit voltage curve to the other. Each color corresponds to an experiment investigating the open circuit voltage of an individual A123 26650m1-B $LiFePO_4$ battery. The unfilled circular and the asterisk markers denote start and end values, respectively. The filled markers represent intermediate measurements.

With the mentioned configuration, the duration of the experiments related to the investigation of the open circuit voltage hysteresis is reduced by the factor of three but still demands thirty-nine days. In order to cope with the challenges associated with the long test duration, highly accurate battery testing units were developed at the Institute of Electrical Measurement and Measurement Signal Processing. Since the development of these testing units is not within the scope of this thesis, interested parties are referred to Grubmüller [46]. For the sake of completeness, it should be mentioned that all battery tests related to charging and discharging were performed with these custom battery testing units.

The results of the first, second and third triple of investigated hysteresis loops are depicted in Figure 2.4, Figure 2.5 and Figure 2.6, respectively. The shown transitions of the open circuit voltage essentially confirm the assumption that the transition of the open circuit voltage proceeds along an exponential-like function from one open circuit voltage curve to the other. However, it is noticeable that the first and last sample of each individual transition curve show a distinct deviation with respect to the according open circuit voltage curve. There are several possible reasons for this circumstance. Firstly, the width of the true hysteresis loops may be larger than 10% of the battery's nominal capacity C_n. This scenario, however, is unlikely since the slope of the transitions appears to decline along the slope of the according open circuit voltage curve in the vicinity of the open circuit voltage plateaus. Secondly, the deviation is caused by the approximation of the open circuit voltage charge and discharge curves. The fact that the experimental evaluations of the open circuit voltage with constant currents of 20 mA and 60 mA yielded similar results contradicts this assumption. Third, the deviation is due to horizontal misalignments caused by the different nominal capacities of the investigated batteries. The misalignment of the fist loop shown in Figure 2.5 strongly indicates this circumstance.

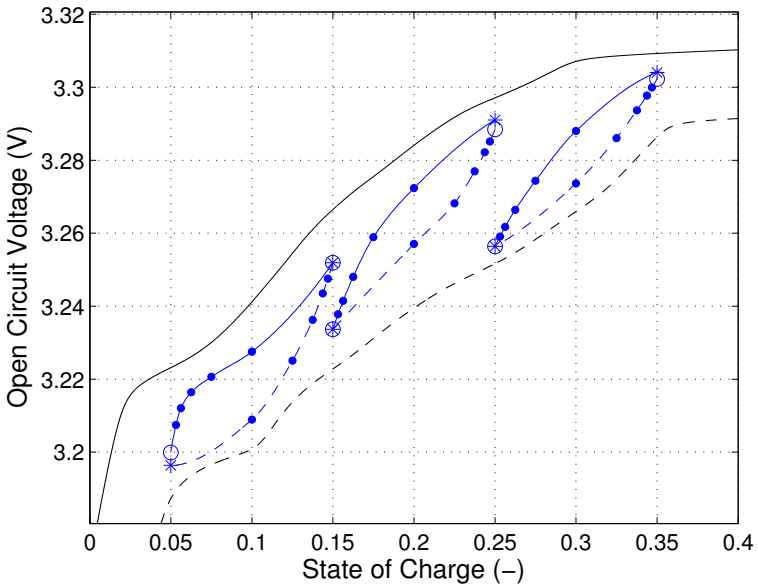

Figure 2.4.: Measured open circuit voltage U_{OCV} of the first triple of hysteresis loops with starting SOC values of 0.05, 0.15 and 0.25, respectively. The blue lines show the charge (solid) and discharge (dashed) transition, while the black lines correspond to $U_{\mathrm{OCV,ch}}$ and $U_{\mathrm{OCV,dis}}$.

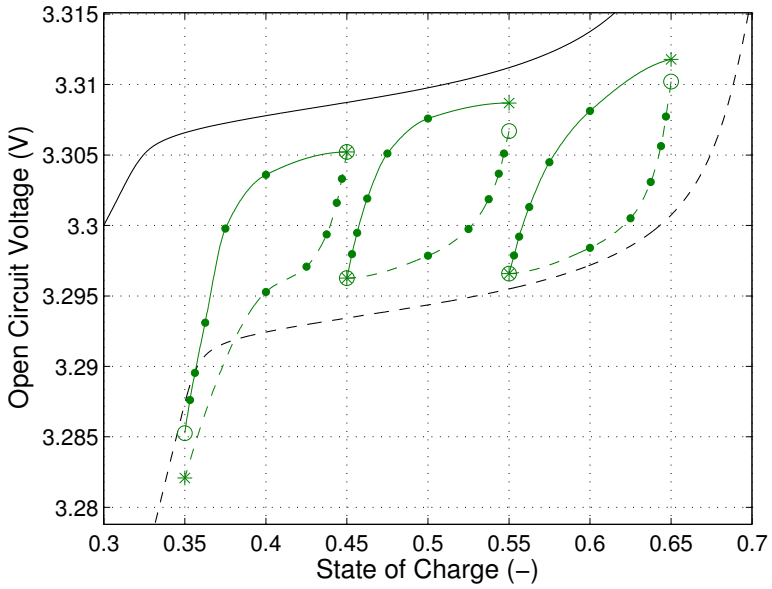

Figure 2.5.: Measured open circuit voltage U_{OCV} of the second triple of hysteresis loops with starting SOC values of 0.35, 0.45 and 0.55, respectively. The green lines show the charge (solid) and discharge (dashed) transition, while the black lines correspond to $U_{\mathrm{OCV,ch}}$ and $U_{\mathrm{OCV,dis}}$.

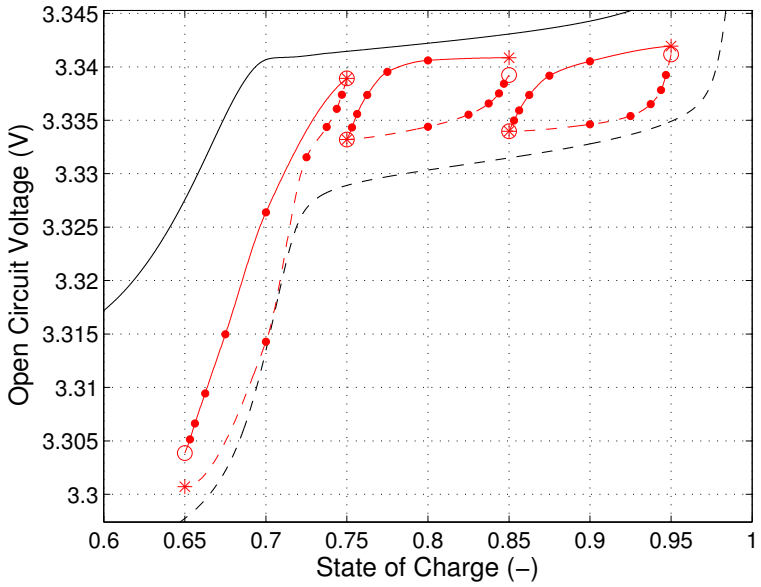

Figure 2.6.: Measured open circuit voltage U_{OCV} of the third triple of hysteresis loops with starting SOC values of 0.65, 0.75 and 0.85, respectively. The red lines show the charge (solid) and discharge (dashed) transition, while the black lines correspond to $U_{\mathrm{OCV,ch}}$ and $U_{\mathrm{OCV,dis}}$.

To summarize, since the the presented results relate to four individual experiments investigating four individual batteries, the source of the mentioned deviation in the

open circuit voltage cannot be clarified at this point. In the case of the hysteresis loops, this circumstance is of minor relevance since the presented investigation aimed to provide of an idea how the open circuit voltage behaves between the open circuit voltage charge and discharge curves. Nevertheless, it should be mentioned that the approximation of the open circuit voltage charge and discharge curves is indeed a source of uncertainty.

In order to complete the model of the open circuit voltage U_{OCV}, state update equations for the SOC and the hysteresis state x_{H} are required. According to the definition section in chapter 1, the SOC corresponds to the stored charge level, normalized by the nominal capacity C_n. Hence, the state update of the SOC is given by

$$\frac{d\mathrm{SOC}}{dt} = \frac{i(t)}{C_n}. \tag{2.2}$$

Based on the findings shown in Figure 2.4-2.6, the functions

$$x_{\mathrm{H}}^{+}(t) = -2e^{-\alpha\left(\int_{t_0}^{t} i(\tau)d\tau - Q_H\right)} + 1 \tag{2.3}$$

$$x_{\mathrm{H}}^{-}(t) = 2e^{\alpha\left(\int_{t_0}^{t} i(\tau)d\tau + Q_H\right)} - 1 \tag{2.4}$$

are used for the derivation of the hysteresis state x_{H} where α is a strictly positive parameter. Hence, the state space representation of the hysteresis state x_{H} is found by differentiation of these functions with respect of time according to

$$\frac{dx_{\mathrm{H}}}{dt} = \begin{cases} \alpha\left(1 - x_H(t)\right) i(t) & \text{if } i(t) \geq 0 \\ \alpha\left(1 + x_H(t)\right) i(t) & \text{if } i(t) < 0 \end{cases}. \tag{2.5}$$

The fact that x_{H} is not continuously differentiable is of minor significance since the estimation algorithm presented in the next chapter relies on a discrete dynamic model. With sample time T_s, the state update equation of the hysteresis state is given by

$$x_{\mathrm{H},k+1} = x_{\mathrm{H},k} + \alpha T_s \left(1 - \mathrm{sign}\ (i_k)\, x_{\mathrm{H},k}\right) i_k. \tag{2.6}$$

Obviously, eq. 2.6 corresponds to a nonlinear integrator which is bounded to ± 1 if the initial value is bounded to ± 1 and α is a strictly positive. If these requirements are fulfilled, the trajectory of the hysteresis state $x_{\mathrm{H},k}$ performs exponential loops for consecutive charge and discharge pulses. Since this nonlinear integrator utilizes only a one-dimensional space, the extension of state-of-the-art models by this additional dynamics comes at minor computational costs.

3. Bayesian Filtering for Battery Monitoring

As mentioned in chapter 1, a common way to estimate the SOC of a battery system is to infer the SOC from current and voltage measurements by applying Bayesian filtering methods. According to this approach this chapter deals with a Bayesian filtering approach, which considers the ambiguous mapping between the SOC and open circuit voltage U_{OCV} discussed in the previous chapter. Hence, a joint estimation framework based on a sequential Monte Carlo method will be used.

This chapter is structured as follows: First, the underlying principles of the used estimation framework will be presented in a short introducing section before the performance of the proposed estimator will be validated for both simulated and measured data records. In order to provide realistic load scenarios, the according current profiles of the battery's operating current will be derived by commonly used driving cycles for hybrid electric vehicles.

3.1. Prerequisites

The aim of this section is to offer the reader a rough overview of the principles of the used joint estimation framework utilizing Rao-Blackwellized particle filtering. Note that the explanations in this chapter cannot compete with a comprehensive description of sequential Monte Carlo integration used for identification and state inference.

3.1.1. Joint/Dual Estimation

With state estimation one often encounters the problem that the state space model required by the estimator is uncertain. Depending on the application, the degree of uncertainty can vary between some uncertain parameters of a potentially well-modeled process (gray-box models) and a priori completely unknown parameterization of a white-box model (e.g. a neural network). The goal of joint/dual estimation is to simultaneously estimate the states and the parameters. This approach might be motivated by different reasons. On the one hand, the parameters of the model are tracked in order to improve the state space representation and, thus, the accuracy of the state estimates. On the other hand, the approach of simultaneous state and parameter estimation might be only due to the system identification perspective as e.g. regression problems are conceivably solved more easily in the state space.

In any case, one faces the problem to estimate simultaneously the states and parameters of a dynamic system. Since the states and the parameters are functionally dependent on each other, an optimal solution for the estimates of the states and

the parameters does not exist.[1] Thus, only suboptimal estimators are available to tackle the problem of simultaneous state and parameter estimation. In the literature, the common algorithms can be divided into dual and joint estimation. Figure 3.1 schematically illustrates the fundamental differences the two concepts.

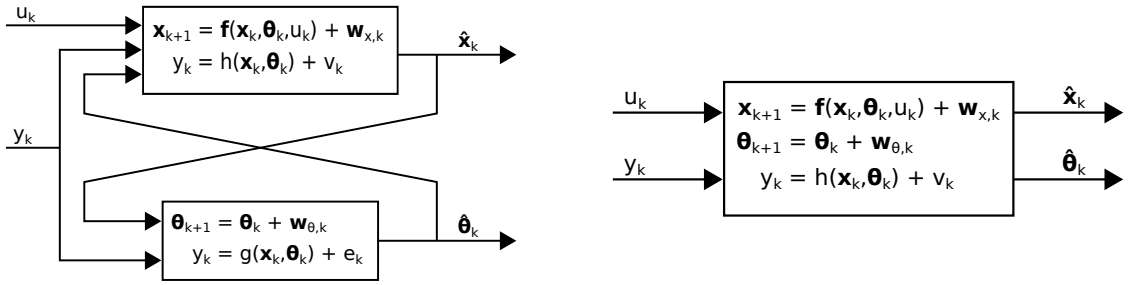

(a) Dual estimation (b) Joint estimation

Figure 3.1.: Illustration of the two concepts for simultaneously estimating the states $\mathbf{x}_k$ and the parameters $\boldsymbol{\theta}_k$ of a state space model.

For dual estimation, two separate estimators are used: one to estimate the states, and one for the parameters. Since the state process and the parameter process are functionally dependent on each other, the estimate of the states is fed back to the parameter estimator and vice versa. The role of the estimates can be interpreted as additional measurements. Consequently, the dimensionality of the state and parameter estimators only depend on the dimensionality of the state vector and the parameter vector, respectively.

The alternative approach is joint estimation, whereby the state and the parameter vector are augmented and the state update equation is (in most cases) expanded by a random walk model. Hence, the model order increases by the dimensionality of the parameter vector $\boldsymbol{\theta}$. As a result, the estimation is done by only one estimator which targets the augmented system. Since the augmented state space model is certainly nonlinear, this approach is compared to dual estimation much more restrictive with respect to the choice of the estimator.

Unfortunately, there is no common rule which approach should be pursued. From a practical point of view, the dual approach is often easier to implement since it is more likely that the problem can be tackled by (suboptimal) Kalman filtering (see e.g. Wan et al. [47–50]). Alternatively, by augmenting the parameters and the states, the corresponding statistics is entirely taken into consideration for the estimate of the state vector which is not the case for dual estimation. As for the approach for estimating the SOC of an $LiFePO_4$ battery presented herein, it was decided to constitute an estimator on the principle of joint estimation similar to the reviews by Gustafsson and Schön [51] or Schön et al. [52].

[1] In this context, the term "optimal" denotes the closed form solution in the Bayesian sense which basically corresponds to the expectation value with respect to the according posterior distribution.

3.1.2. Sequential Monte Carlo

Bayesian filtering denotes a probabilistic method for estimating the posterior distribution of the states of a hidden Markov model at time instant $\mathbf{x}_k$, based on all available observations $\mathbf{y}_{0:k}$ and some prior information about the initial states represented by a prior probability density function $p(\mathbf{x}_0)$. The estimate of the states is given by the conditional expectation value with respect to the posterior density $p(\mathbf{x}_k|\mathbf{y}_{0:k})$ according to[2]

$$\hat{\mathbf{x}}_k = \mathbb{E}\{\mathbf{x}_k|\mathbf{y}_{0:k}\} = \int \mathbf{x}_k p(\mathbf{x}_k|\mathbf{y}_{0:k}) d\mathbf{x}_k \tag{3.1}$$

where the posterior density is found by applying Bayes' rule according to

$$p(\mathbf{x}_k|\mathbf{y}_{0:k}) = \frac{p(\mathbf{y}_k|\mathbf{x}_k)p(\mathbf{x}_k|\mathbf{y}_{0:k-1})}{p(\mathbf{y}_k|\mathbf{y}_{0:k-1})}. \tag{3.2}$$

Since $p(\mathbf{x}_k|\mathbf{y}_{0:k-1})$ and $p(\mathbf{y}_k|\mathbf{y}_{0:k-1})$ are not directly accessible, these densities must be expressed in terms of accessible ones. By means of the Chapman-Kolmogorov equation, the prediction density $p(\mathbf{x}_k|\mathbf{y}_{0:k-1})$ can be expressed in terms of the state update density $p(\mathbf{x}_k|\mathbf{x}_{k-1})$ and the posterior density of the previous time instant $p(\mathbf{x}_{k-1}|\mathbf{y}_{0:k-1})$ according to

$$p(\mathbf{x}_k|\mathbf{y}_{0:k-1}) = \int p(\mathbf{x}_k|\mathbf{x}_{k-1}) p(\mathbf{x}_{k-1}|\mathbf{y}_{0:k-1}) d\mathbf{x}_{k-1}. \tag{3.3}$$

The probability density $p(\mathbf{y}_k|\mathbf{y}_{0:k-1})$ is found by marginalization and integration of the joint probability density $p(\mathbf{x}_k, \mathbf{y}_k|\mathbf{y}_{0:k-1})$ with respect to $\mathbf{x}_k$. By using the expression for the prediction density (eq. 3.3), $p(\mathbf{y}_k|\mathbf{y}_{0:k-1})$ can be expressed in terms of accessible probability densities and the expression for the posterior density is given by

$$p(\mathbf{x}_k|\mathbf{y}_{0:k}) = \frac{p(\mathbf{y}_k|\mathbf{x}_k) \int p(\mathbf{x}_k|\mathbf{x}_{k-1}) p(\mathbf{x}_{k-1}|\mathbf{y}_{0:k-1}) d\mathbf{x}_{k-1}}{\int p(\mathbf{y}_k|\mathbf{x}_k) \left(\int p(\mathbf{x}_k|\mathbf{x}_{k-1}) p(\mathbf{x}_{k-1}|\mathbf{y}_{0:k-1}) d\mathbf{x}_{k-1} \right) d\mathbf{x}_k}, \tag{3.4}$$

where $p(\mathbf{y}_k|\mathbf{x}_k)$ is the likelihood function and is defined by the observation model. Usually, the problem is tackled in a two-stage procedure. In the first step (time update), the prediction $p(\mathbf{x}_k|\mathbf{y}_{0:k-1})$ density is computed. In the second step (measurement update), the conditioning on the observation $\mathbf{y}_k$ is performed and the posterior density is computed.

Eq. 3.1 can be solved in closed form only if the following conditions are met: The prior density $p(\mathbf{x}_0)$ as well as the probability densities associated with the process and measurement noise are Gaussian. The state update and the observation model correspond to affine transformations. This circumstance is based on the fact that the Gaussian distribution is preserved by an affine transformation. Thus, the rules for operating with Gaussian probability densities (see Appendix A) can be applied and the integrals must not explicitly be solved. In such cases, the Kalman filter

[2]Since this chapter deals with probability density functions, the integral operators shown herein relate to definite integrations with respect to the support of the associated probability density functions. For the sake of clarity, the boundaries of these integrals are not shown.

optimally estimates the sequencing of the posterior density. Since this algorithm is highly prevalent these days, interested parties are referred to [53, 54] for an in-depth treatment of Kalman filtering. If the mentioned conditions are not met while in a certain sense "mild conditions" emerge, suboptimal estimators like the extended Kalman filter (EKF) or the unscented Kalman filter (UKF) are a good choice to provide an acceptable approximation of the sought expectation value. Unfortunately, in the case of the joint estimation approach presented in this thesis, these "mild conditions" are not met. Concerning the Bayesian filtering problem, the only option left is to estimate the expectation value of the posterior density with a Monte Carlo estimator. As the name suggests, Monte Carlo estimators are based on the principle of Monte Carlo integration, which is a pure simulation based approach to evaluate definite integrals by statistical sampling. In the literature, these samples are often referred to as particles which the denotation particle filtering is derived from. Interested parties should refer to according introducing literature (see e.g. [55–59]) for an in-depth treatment of particle filtering.

Monte Carlo Integration

Consider the multidimensional definite integral

$$I = \int_S g(\mathbf{x}) d\mathbf{x} \tag{3.5}$$

where $\mathbf{x} \in \mathbb{R}^n$ is a high-dimensional space and the function $g(\mathbf{x})$ is not integrable in closed form. If $g(\mathbf{x})$ can be divided into a product of an arbitrary test function $\varphi(\mathbf{x})$ and a probability density $\pi(\mathbf{x})$ with support S, the definite integral I is given by the expectation value of the test function $\varphi(\mathbf{x})$ with respect to the probability density $\pi(\mathbf{x})$. The key idea of Monte Carlo integration is to sample a set of N independent samples $\{\mathbf{x}_i\}_{i=1}^N$ generated by the density $\pi(\mathbf{x})$ and to approximate $\mathbb{E}_\pi\{\varphi(\mathbf{x})\}$ by the empirical average

$$\hat{I} = \frac{1}{N} \sum_{i=1}^{N} \varphi(\mathbf{x}_i). \tag{3.6}$$

By the Strong Law of Large Numbers, $\hat{I}$ converges almost surely to $\mathbb{E}_\pi\{\varphi(\mathbf{x})\}$ whereby the variance of the estimate is given by

$$\mathrm{var}(\hat{I}) = \frac{1}{N} \left(\int \varphi^2(\mathbf{x}) \pi(\mathbf{x}) d\mathbf{x} - I^2 \right). \tag{3.7}$$

Obviously, the dimension of the vector $\mathbf{x}$ does not influence the variance of the estimated integral. Therefore, Monte Carlo integration is the only feasible method in the case of high-dimensional integrals.

At first glance, the Monte Carlo approach appears to be straight forward and easy to implement. Unfortunately, this is not entirely true since direct sampling from the distribution associated with the target density $\pi(\mathbf{x})$ is in most cases infeasible. In situations when the computation time is of minor relevance, this problem can be tackled by Markov Chain Monte Carlo (MCMC) algorithms. However, in the case of particle filtering, the computational demand of the sampler plays a major role as the

approximation of the conditional expectation integral with respect to the posterior density $p(\mathbf{x}_k|\mathbf{y}_{0:k})$ is required at every time instant k. Hence, most implementations of the particle filter utilize a statistical sampler based on importance sampling.

Importance Sampling

The concept of importance sampling is premised on the approach to sample from an easily accessible distribution (proposal or importance distribution) instead of the target distribution. If the support of the proposal density $\gamma(\mathbf{x})$ is at least as great as the support of the target density, the target density can be partitioned according to

$$\tilde{\pi}(\mathbf{x}) = \tilde{w}(\mathbf{x})\gamma(\mathbf{x}) \tag{3.8}$$

where $\tilde{w}(\mathbf{x})$ corresponds to a weight function and $\tilde{\pi}(\mathbf{x})$ denotes the unnormalized target density. It is beneficial to use the notation $\pi(\mathbf{x}) = \frac{\tilde{\pi}(\mathbf{x})}{\alpha_\pi}$ since in many cases the target density is only known up to proportionality. The factorization of the target density is given by

$$\pi(\mathbf{x}) = \frac{\tilde{w}(\mathbf{x})\gamma(\mathbf{x})}{\int \tilde{w}(\mathbf{x})\gamma(\mathbf{x})d\mathbf{x}} \tag{3.9}$$

where the integral of the denominator corresponds to the normalization constant α_π and can be interpreted as the expectation value of the unnormalized weight function $w(\mathbf{x}) = \frac{\tilde{\pi}(\mathbf{x})}{\gamma(\mathbf{x})}$ with respect to the importance density $\gamma(\mathbf{x})$. By sampling a set of N independent samples $\{\mathbf{x}_i\}_{i=1}^N$ generated by this density, the normalization constant can be approximated by the empirical average

$$\hat{\alpha}_\pi = \frac{1}{N}\sum_{i=1}^{N}\frac{\tilde{\pi}(\mathbf{x}_i)}{\gamma(\mathbf{x}_i)}. \tag{3.10}$$

It can easily be shown that this estimator is unbiased with variance

$$\mathrm{var}(\hat{\alpha}_\pi) = \frac{\alpha_\pi^2}{N}\left(\int \frac{\pi^2(\mathbf{x})}{\gamma(\mathbf{x})}d\mathbf{x} - 1\right). \tag{3.11}$$

In a similar way, the expectation value $\mathbb{E}_\pi\{\varphi(\mathbf{x})\}$ and, thus, the sought integral is approximated according to

$$\hat{I}^{\mathrm{IS}} = \sum_{j=1}^{N}\underbrace{\frac{\frac{\tilde{\pi}(\mathbf{x}_j)}{\gamma(\mathbf{x}_j)}}{\sum_{i=1}^{N}\frac{\tilde{\pi}(\mathbf{x}_i)}{\gamma(\mathbf{x}_i)}}}_{=w_j}\varphi(\mathbf{x}_j) \tag{3.12}$$

where w_j denotes the j^{th} normalized weight. In the literature, the set $\{\mathbf{x}_i, w_i\}_{i=1}^N$ is often referred to as particle set or particle system. If the normalization constant α_π is not known, the importance estimate I^{IS} is biased. According to [56], in this case, the asymptotic variance is given by

$$\lim_{N\to\infty}\mathrm{var}\left(\hat{I}^{\mathrm{IS}}\right) = \frac{1}{N}\int \frac{\pi^2(\mathbf{x})}{\gamma(\mathbf{x})}\left(\varphi(\mathbf{x}) - I\right)^2 d\mathbf{x}. \tag{3.13}$$

Compared to the native Monte Carlo estimator, the variance of the estimator is not only influenced by the size of the sample set but also by the choice of the proposal distribution. Hence, the proposal distribution is a significant design parameter.

Figure 3.2 illustrates the concept of importance sampling. The blue line shows a multimodal unnormalized target distribution derived by a Gaussian mixture model. A Gaussian proposal distribution (green) was used to generate the particle system of 100 samples (red). The test function was set to $\varphi(x) = x$. The true expectation value of the test function with respect to the target density is $I = 0.833$. The result obtained by the importance sampling estimator is $\hat{I}^{\mathrm{IS}} = 1.09$.

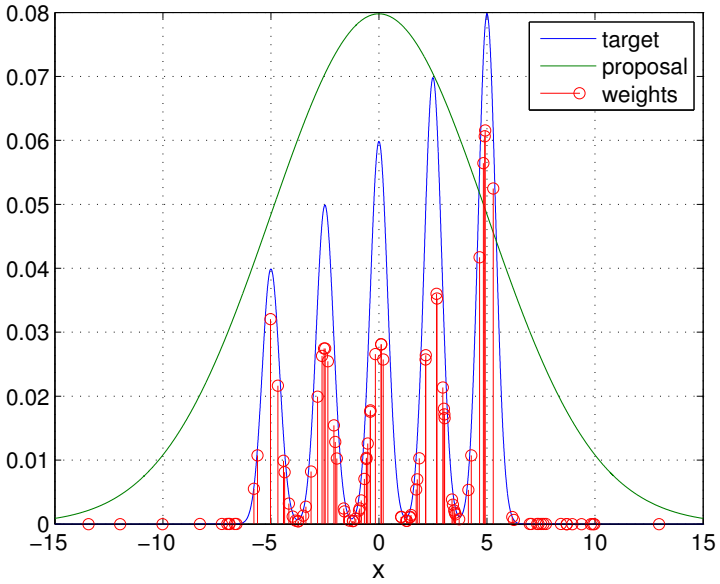

Figure 3.2.: Illustration of the principle of importance sampling. The blue line corresponds to the unnormalized target density $\tilde{\pi}(x)$. The samples and the associated normalized weights (red) were generated by means of a Gaussian proposal density $\gamma(x)$ (green line).

Sequential Importance Sampling

In most particle filter implementations, the sampler targets the posterior smoothing density $p(\mathbf{x}_{0:k}|\mathbf{y}_{0:k})$ instead of the posterior filtering density $p(\mathbf{x}_k|\mathbf{y}_{0:k})$. As for the computational demands, this circumstance is beneficial since the complexity of targeting $p(\mathbf{x}_{0:k}|\mathbf{y}_{0:k})$ is $\mathcal{O}(N)$ compared to $\mathcal{O}(N^2)$ for targeting the filtering distribution $p(\mathbf{x}_k|\mathbf{y}_{0:k})$ [60]. However, by targeting the smoothing posterior density, a fundamental problem arises. Obviously, the dimension of the posterior smoothing density increases every time instant k by the dimension of the state vector. Consequently, the computational complexity increases at least linearly, which makes native importance sampling infeasible to track the sequencing of the posterior mean values.

This problem is tackled by sequential importance sampling which admits a fixed computational complexity with each time step. This can be achieved by choosing

the proposal density at time step k to be of the structure

$$\gamma_k(\mathbf{x}_{0:k}) = \gamma_0(\mathbf{x}_0) \prod_{i=1}^{k} \gamma_i(\mathbf{x}_i|\mathbf{x}_{0:i-1}). \tag{3.14}$$

By plugging the proposal density $\gamma_k(\mathbf{x}_{0:k})$ in eq. 3.8, a sequential update formula can be derived for the weight function according to

$$\tilde{w}_k(\mathbf{x}_{0:k}) = \underbrace{\frac{\tilde{\pi}_{k-1}(\mathbf{x}_{0:k-1})}{\gamma_{k-1}(\mathbf{x}_{0:k-1})}}_{=\tilde{w}_{k-1}(\mathbf{x}_{0:k-1})} \frac{\tilde{\pi}_k(\mathbf{x}_{0:k})}{\tilde{\pi}_{k-1}(\mathbf{x}_{0:k-1})\gamma_k(\mathbf{x}_k|\mathbf{x}_{0:k-1})}. \tag{3.15}$$

Since only the conditional marginal proposal density $\gamma_k(\mathbf{x}_k|\mathbf{x}_{0:k-1})$ appears in eq. 3.15, it looks like that the Bayesian filtering problem is essentially solved by applying the sequential update scheme. Unfortunately, this is not true since the variance of the estimator increases exponentially with k.

This phenomenon is denoted as sample degeneracy or weight degeneracy problem in the literature. The problem in this context is that after some time steps all samples except for one will have negligible weight. It is certainly clear that the approximation of any integral by an empirical average, based on one single sample, is left to perform poorly. The tutorial by Doucet and Johansen [56] provides an intuitive toy example which illustrates the problem of sample degeneracy. One way which partially solves this problem is to introduce a mechanism for selection which is most commonly done by resampling. This introducing section refrains from treating the resampling step in detail. Interested parties should refer to e.g. [61–63] to gain an overview of the existing resampling strategies. However, it should be highlighted that the selection step must be performed either at each time step (e.g. the bootstrapping filter) or if the estimate of the effective sample size

$$\hat{N}_{\text{eff}} = \frac{1}{\sum_{i=1}^{N} (w_k^i)^2} \tag{3.16}$$

drops below a certain threshold.

Particle Filtering

Particle filtering is (at least in most implementations) nothing else than using the sequential Monte Carlo estimator by choosing the unnormalized target density $\tilde{\pi}_k(\mathbf{x}_{0:k}) = p(\mathbf{x}_{0:k}, \mathbf{y}_{0:k})$ and the normalization constant $\alpha_\pi = p(\mathbf{y}_{0:k})$. Hence, the sequential update scheme for the weight function (eq. 3.15) is given by

$$\tilde{w}_k(\mathbf{x}_{0:k}) = \tilde{w}_{k-1}(\mathbf{x}_{0:k-1}) \frac{p(\mathbf{y}_k|\mathbf{x}_{0:k}, \mathbf{y}_{0:k-1}) p(\mathbf{x}_k|\mathbf{x}_{0:k-1}, \mathbf{y}_{0:k-1})}{\gamma_k(\mathbf{x}_k|\mathbf{x}_{0:k-1}, \mathbf{y}_{0:k})} \tag{3.17}$$

where the more general notation $\gamma(\mathbf{x}_{0:k}, \mathbf{y}_{0:k})$ is used for the proposal density. Due to the properties of hidden Markov models, the update for i^{th} weight is given by

$$\tilde{w}_k^i = \tilde{w}_{k-1}^i \frac{p(\mathbf{y}_k|\mathbf{x}_k^i) p(\mathbf{x}_k^i|\mathbf{x}_{k-1}^i)}{\gamma_k(\mathbf{x}_k^i|\mathbf{x}_{0:k-1}^i, \mathbf{y}_{0:k})}. \tag{3.18}$$

This expression can be simplified if the state update density $p(\mathbf{x}_k^i|\mathbf{x}_{k-1}^i)$ is used as proposal density. In combination with the selection by multinomial resampling at each time step, this approach is known as bootstrapping (see e.g. Gordon et al. [64] or Candy [65]).

3.1.3. Rao-Blackwellization

Before explaining the concept of Rao-Blackwellization in detail, attention is drawn to the following two quotes which often appear in conjunction with Monte Carlo estimators in the literature and encourage Rao-Blackwellization.

> "Anyone who considers arithmetic methods of producing random digits is, of course, in a state of sin," John Von Neumann, 1951
>
> "The only good Monte Carlos are dead Monte Carlos", Trotter & Tukey, 1954

The conclusion which can be drawn from these quotes is not that Monte Carlo methods should not be taken into consideration, but what is more important: they should be avoided whenever it is possible. In other words, this means whenever an expression can be calculated in closed form, it should be calculated in closed form instead of using the purely random approach of Monte Carlo estimators. Of course, if one faces a nonlinear or/and non-Gaussian filtering problem, the closed form is in general intractable. However, the idea which was suggested by Doucet et al. [66] and Schön et al. [52] is to use the concept of Rao-Blackwellization to compute parts of the filtering problem analytically and, thus, reduce the variance of the estimator.

The Rao-Blackwell theorem says that if $\hat{\theta}(\mathbf{x}_{1:N})$ is an estimator for θ with finite variance and $T(\mathbf{x}_{1:N})$ is a sufficient statistic[3] for θ, then the estimator

$$\hat{\theta}_{\mathrm{RB}}(T) = \mathbb{E}\{\hat{\theta}(\mathbf{x}_{1:N})|T(\mathbf{x}_{1:N})\} \tag{3.19}$$

typically performs better than every other estimator. In other words, the estimator $\hat{\theta}_{\mathrm{RB}}(T)$ defines the lower bound of the mean squared error since

$$\mathbb{E}\left\{\left(\hat{\theta}_{\mathrm{RB}} - \theta\right)^2\right\} \leq \mathbb{E}\left\{\left(\hat{\theta} - \theta\right)^2\right\}. \tag{3.20}$$

At the beginning of this chapter, an estimator was already mentioned which employs this concept. If the Bayesian filtering problem is tractable in closed form, the Kalman filter denotes the minimum mean squared error estimator with the sufficient statistic being the mean and the covariance function derived by the Kalman filter equations.

The concept of Rao-Blackwellization in the context of nonlinear filtering, which is also known as marginalization, is illustrated by the following simple example.

Toy Example

Suppose the joint probability density $p(x, z)$ can be factorized according to

$$p(x, z) = p(z|x)p(x) \tag{3.21}$$

[3] A statistic is a measure of a sample's (certain) attribute which is calculated by applying a function to values of the sample. A statistic is said to be sufficient if there exists no other statistic calculated from the same sample which provides further information [67].

where $p(x)$ is an arbitrary probability density and the conditional probability density is assumed to be Gaussian $p(z|x) = \mathcal{N}(\mu_z(x), \sigma_z^2(x))$. In the present case, $p(x)$ is chosen to be a Gaussian mixture density given by

$$p(x) = \sum_{i=1}^{5} m_i \mathcal{N}(\mu_{x,i}, \sigma_{x,i}^2) \tag{3.22}$$

with mixture weights, mean values and standard deviations according to

$$\begin{aligned} \mathbf{m} &= [0.12, 0.16, 0.24, 0.24, 0.24] \\ \boldsymbol{\mu}_x &= [-3, -2, 0, 2, 3] \\ \boldsymbol{\sigma}_x &= [0.4, 0.6, 0.6, 0.6, 0.8]\,. \end{aligned}$$

Figure 3.3 illustrates the multimodal character of this probability density function. The functions for the conditional mean and the conditional standard deviation of $p(z|x)$ are given by

$$\mu_z(x) = 0.8 - e^{-0.4605(x+5)} \tag{3.23a}$$

$$\sigma_z(x) = 0.1e^{-\frac{x^2}{100}}. \tag{3.23b}$$

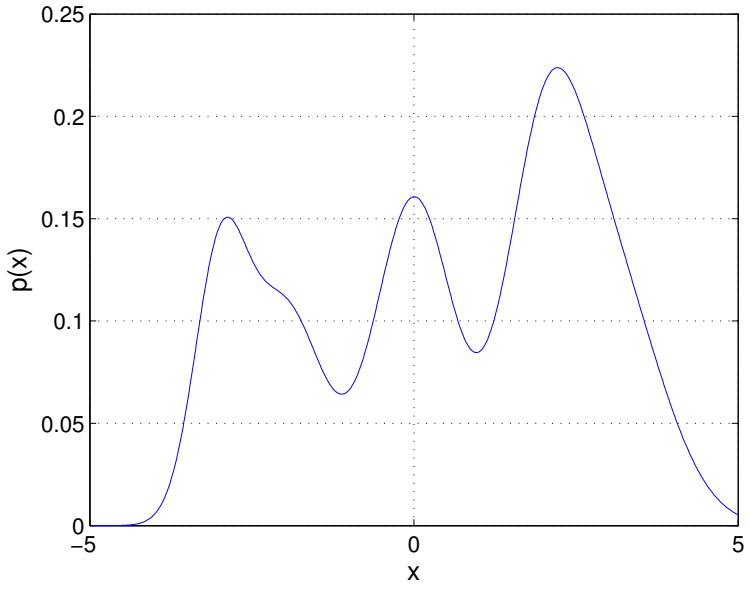

Figure 3.3.: Marginal probability density function $p(x)$ derived by a 5^{th} order Gaussian mixture model.

The joint probability density function $p(x, z)$ is visualized in Figure 3.4. Obviously, this function is non-symmetric and multimodal, whereby the modes are spread over a relatively wide range. This situation entails some serious problems if an optimization-based approach is pursued for estimation. For instance, the simplest case is considered and the mean values are estimated by means of a maximum likelihood estimator. Even though the problems associated with the non-convexity of $p(x, z)$ are solved, this approach yields to estimated mean values of

$\hat{x}_{\mathrm{MLE}} = 2.244$ and $\hat{z}_{\mathrm{MLE}} = 0.764$, which is exactly the location of the highest mode. The true expectation value[4] with respect to the test function $\varphi(x, z) = [x, z]^T$ is $\mathbb{E}\{\varphi(x, z)\} = [0.52, 0.668]^T$.

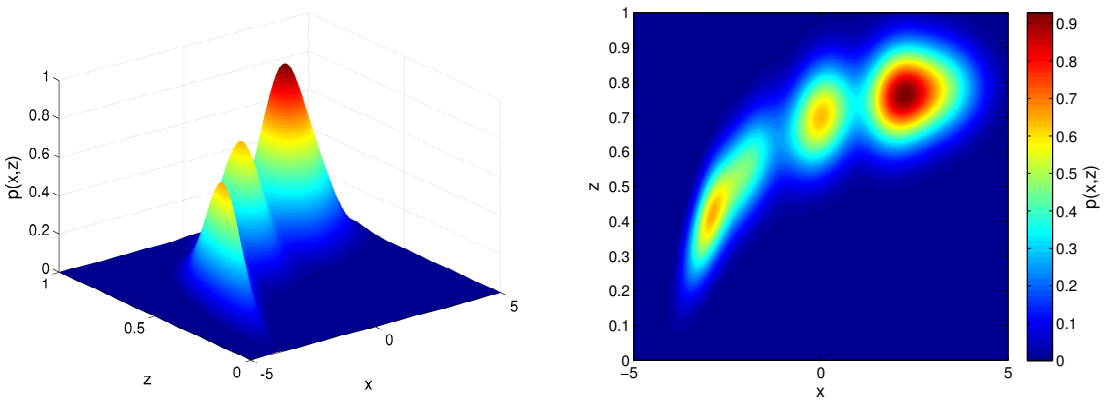

(a) Surface plot of $p(x, z)$ (b) Filled 2D contour plot of $p(x, z)$

Figure 3.4.: Visualization of the joint probability density function $p(x, z)$.

Hence, the problem is tackled by statistical sampling. Since this toy example is aimed to introduce the concept of Rao-Blackwellized particle filters, the statistical samples are provided by an importance sampler instead of an MCMC sampler. Of course, the latter would provide more accurate estimates.

Targeting the joint probability density function $p(x, z)$ with an importance sampler requires to sample N samples from an two-dimensional multivariate proposal density. For instance, consider a sample set of $N = 100$ samples. It is clear that importance sampling provides a poor approximation of the expectation integral with respect to the two-dimensional target density $p(x, z)$, if the particle set consists only of 100 samples. The key idea of Rao-Blackwellization is to tackle this problem by sampling from a different, lower dimensional target density. Recall the factorization of the joint probability density function $p(x, z)$ (eq. 3.21). It was claimed that the marginal probability density function $p(x)$ can be arbitrary but the conditional marginal probability density $p(z|x)$ is restricted to be Gaussian. Thus, instead of targeting the joint probability density function $p(x, z)$, the importance sampler can be used to target the marginal probability density function $p(x)$ by the particle approximation

$$p(x)dx \approx \sum_{i=1}^{N} w_i \delta_{X_i}(x). \tag{3.24}$$

Since the Rao-Blackwellized sampler utilizes only a one-dimensional sample space, the particle approximation of this target density is much denser (see Figure 3.5).

[4]The desired expectation value cannot be obtained by analytical integration. Thus, the attribute "true" is not entirely correct. However, due to the chosen structure of $p(x, z)$ and the fact that the normalization constant is known, the expectation integral can be accurately evaluated by numerical quadrature techniques. Usually, this comfortable situation is not met in practice.

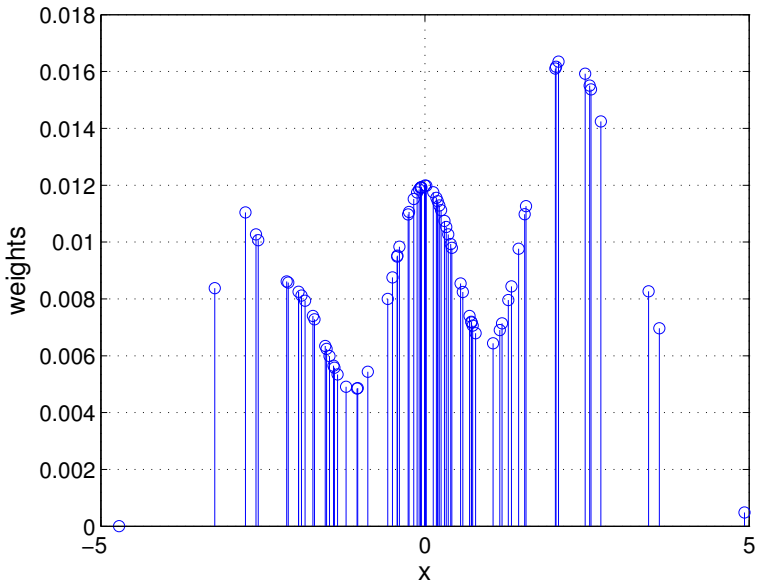

Figure 3.5.: Sampled particles and associated importance weights targeting the one-dimensional marginal probability density function $p(x)$.

The estimates of the Rao-Blackwellized importance sampler are derived by plugging the particle approximation of $p(x)$ (eq. 3.24) into the desired expectation integrals according to

$$\mathbb{E}\{x\} = \iint xp(z|x)p(x)dxdz \approx \sum_{i=1}^{N} w_i x_i \int p(z|x_i)dz = \sum_{i=1}^{N} w_i x_i \tag{3.25a}$$

$$\mathbb{E}\{z\} = \iint zp(z|x)p(x)dxdz \approx \sum_{i=1}^{N} w_i \int zp(z|x_i)dz = \sum_{i=1}^{N} w_i \mu_z(x_i). \tag{3.25b}$$

By comparing the Rao-Blackwellized estimators with the ones obtained by native importance sampling, two circumstances are striking. First, the Rao-Blackwellized estimator of $\mathbb{E}\{x\}$ appears formally the same as the according native importance sampling estimator. The only difference is that the samples $\{x_i\}_{i=1}^{N}$ were generated by targeting $p(x)$ instead of $p(x, z)$. Second, the Rao-Blackwellized estimator of $\mathbb{E}\{z\}$ is a sum of the weighted mean values of z conditioned on the according particle. This is basically the reason why $p(z|x)$ was initially restricted to be Gaussian. In the case of this toy example, $p(z|x)$ can be any probability density function as long as its mean function is evaluable. However, in the context of Bayesian filtering, the sequencing of the mean function of $p(z_k|x_{0:k}, y_{0:k})$ is tracked. Hence, to benefit from a (partly) closed form solution, $p(z_k|x_{0:k}, y_{0:k})$ must be Gaussian to be feasible for Kalman filtering.

The improvement of estimation accuracy by the Rao-Blackwellized setting is demonstrated in Figure 3.6, in which the results of a Monte Carlo analysis of 100 trails are shown. The blue lines correspond to the true expectation values, the green and the red line to the according native and Rao-Blackwellized importance estimates, respectively. Both estimators utilize a particle set of $N = 100$ samples. Apparently, the variance of the Rao-Blackwellized importance estimator is much smaller compared to the variance of the native importance estimator.

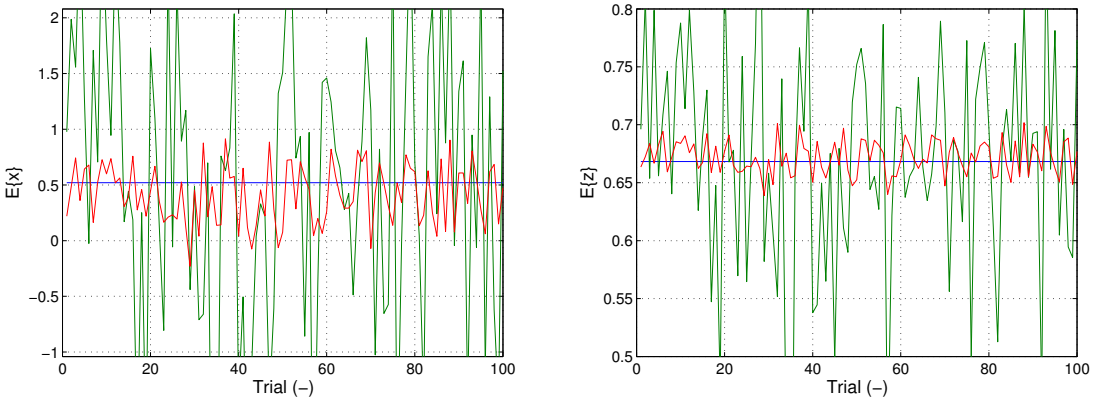

(a) True and estimated values of $\mathbb{E}\{x\}$

(b) True and estimated values of $\mathbb{E}\{z\}$

Figure 3.6.: Estimated and true values of $\mathbb{E}\{x\}$ and $\mathbb{E}\{z\}$. A Monte Carlo analysis of 100 trials was carried out to evaluate the performance of the native and the Rao-Blackwellized importance estimators. The blue lines indicate the true values of 0.52 and 0.668, respectively. The green lines correspond to the native importance estimators, while the red lines represent the results obtained by Rao-Blackwellized importance sampler.

Conditionally Linear Gaussian State Space Models

Before proceeding with the equations of the Rao-Blackwellized particle filter, it should be clarified first which class of nonlinear state space models can be taken into consideration for this framework. As mentioned before, the conditional marginal probability density function must be Gaussian. The class of nonlinear state space models which meet this requirement are conditionally linear Gaussian state space (CLGSS) models. Characteristic for this kind of state space models is that the state vector can be partitioned into a nonlinear and a conditionally linear part according to $\mathbf{x}_k = \left[(\mathbf{x}_k^{\mathrm{N}})^T, (\mathbf{x}_k^{\mathrm{L}})^T\right]^T$. Regarding the nonlinear states $\mathbf{x}_k^{\mathrm{N}}$, no restrictions with respect to the according state update equation and measurement equation apply. In contrast, the states $\mathbf{x}_k^{\mathrm{L}}$ are restricted to linearly enter both the state update equation and the measurement equation.

In general, different types of CLGSS models exist and differ with respect to the state update equation of the nonlinear states $\mathbf{x}_k^{\mathrm{N}}$. The joint estimation framework presented in this thesis is based on a mixed linear/nonlinear state space model (see see e.g [52, 68, 69]) with a functional form according to

$$\mathbf{x}_{k+1}^{\mathrm{N}} = \mathbf{f}_k^{\mathrm{N}}(\mathbf{x}_k^{\mathrm{N}}) + \mathbf{A}_k^{\mathrm{N}}(\mathbf{x}_k^{\mathrm{N}})\mathbf{x}_k^{\mathrm{L}} + \mathbf{w}_k^{\mathrm{N}} \tag{3.26a}$$

$$\mathbf{x}_{k+1}^{\mathrm{L}} = \mathbf{f}_k^{\mathrm{L}}(\mathbf{x}_k^{\mathrm{N}}) + \mathbf{A}_k^{\mathrm{L}}(\mathbf{x}_k^{\mathrm{N}})\mathbf{x}_k^{\mathrm{L}} + \mathbf{w}_k^{\mathrm{L}} \tag{3.26b}$$

$$\mathbf{y}_k = \mathbf{h}_k(\mathbf{x}_k^{\mathrm{N}}) + \mathbf{C}_k(\mathbf{x}_k^{\mathrm{N}})\mathbf{x}_k^{\mathrm{L}} + \mathbf{v}_k. \tag{3.26c}$$

The distributions of the process noise, the measurement noise and the prior distribution of the conditional linear process are given by

$$\left[(\mathbf{w}_k^{\mathrm{N}})^T, (\mathbf{w}_k^{\mathrm{L}})^T\right]^T \sim \mathcal{N}(\mathbf{0}, \mathbf{Q}_k(\mathbf{x}_k^{\mathrm{N}})) \tag{3.27a}$$

$$\mathbf{v}_k \sim \mathcal{N}(\mathbf{0}, \mathbf{R}_k(\mathbf{x}_k^{\mathrm{N}})) \tag{3.27b}$$

$$\mathbf{x}_0^{\mathrm{L}}|\mathbf{x}_0^{\mathrm{N}} \sim \mathcal{N}(\hat{\mathbf{x}}_{0|-1}^{\mathrm{L}}(\mathbf{x}_0^{\mathrm{N}}), \mathbf{P}_{0|-1}(\mathbf{x}_0^{\mathrm{N}})) \tag{3.27c}$$

where the covariance of the process noise is partitioned according to

$$\mathbf{Q}_k\left(\mathbf{x}_k^{\mathrm{N}}\right) = \begin{bmatrix} \mathbf{Q}_k^{\mathrm{NN}}(\mathbf{x}_k^{\mathrm{N}}) & \mathbf{Q}_k^{\mathrm{NL}}(\mathbf{x}_k^{\mathrm{N}}) \\ \left(\mathbf{Q}_k^{\mathrm{NL}}(\mathbf{x}_k^{\mathrm{N}})\right)^T & \mathbf{Q}_k^{\mathrm{LL}}(\mathbf{x}_k^{\mathrm{N}}) \end{bmatrix}. \tag{3.27d}$$

The initial distribution of the nonlinear states $\mathbf{x}_0^{\mathrm{N}}$ can be arbitrary.

Rao-Blackwellized Particle Filter (RBPF)

At this point, the equations of the Rao-Blackwellized particle filter can be derived. With the mentioned partition of the state vector, the minimum mean squared error estimates $\hat{\mathbf{x}}_{k|k}^{\mathrm{N}}$ and $\hat{\mathbf{x}}_{k|k}^{\mathrm{L}}$ are given by

$$\mathbb{E}\{\mathbf{x}_k^{\mathrm{N}}, \mathbf{x}_k^{\mathrm{L}} | \mathbf{y}_{0:k}\} = \iint \begin{bmatrix} \mathbf{x}_k^{\mathrm{N}} \\ \mathbf{x}_k^{\mathrm{L}} \end{bmatrix} p\left(\mathbf{x}_k^{\mathrm{N}}, \mathbf{x}_k^{\mathrm{L}} | \mathbf{y}_{0:k}\right) d\mathbf{x}_k^{\mathrm{N}} d\mathbf{x}_k^{\mathrm{L}}. \tag{3.28}$$

In order to benefit from the Rao-Blackwellized setting, this expectation integral is reformulated in such a way that the probability density function associated with the linear states $\mathbf{x}_k^{\mathrm{L}}$ is Gaussian. The posterior expectation value does not change if the joint filtering posterior probability density is expanded according to $p\left(\mathbf{x}_{0:k}^{\mathrm{N}}, \mathbf{x}_k^{\mathrm{L}} | \mathbf{y}_{0:k}\right)$ and the trajectory up to time step $k-1$ is subsequently integrated out of the expectation integral. Hence, marginalization of $p\left(\mathbf{x}_{0:k}^{\mathrm{N}}, \mathbf{x}_k^{\mathrm{L}} | \mathbf{y}_{0:k}\right)$ with respect to the conditionally states $\mathbf{x}_k^{\mathrm{L}}$ leads to the desired expectation integral according to

$$\mathbb{E}\{\mathbf{x}_k^{\mathrm{N}}, \mathbf{x}_k^{\mathrm{L}} | \mathbf{y}_{0:k}\} = \iint \begin{bmatrix} \mathbf{x}_k^{\mathrm{N}} \\ \mathbf{x}_k^{\mathrm{L}} \end{bmatrix} p\left(\mathbf{x}_k^{\mathrm{L}} | \mathbf{x}_{0:k}^{\mathrm{N}}, \mathbf{y}_{0:k}\right) p\left(\mathbf{x}_{0:k}^{\mathrm{N}} | \mathbf{y}_{0:k}\right) d\mathbf{x}_{0:k}^{\mathrm{N}} d\mathbf{x}_k^{\mathrm{L}}. \tag{3.29}$$

By targeting the marginal smoothing posterior density $p\left(\mathbf{x}_{0:k}^{\mathrm{N}} | \mathbf{y}_{0:k}\right)$ with a sequential importance sampler, the particle approximation

$$p\left(\mathbf{x}_{0:k}^{\mathrm{N}} | \mathbf{y}_{0:k}\right) d\mathbf{x}_{0:k}^{\mathrm{N}} \approx \sum_{i=1}^{N} w_{k,i} \delta_{\mathbf{x}_{0:k,i}^{\mathrm{N}}}(\mathbf{x}_{0:k}^{\mathrm{N}}) \tag{3.30}$$

is used to approximate the conditional expectation values according to

$$\hat{\mathbf{x}}_{k|k}^{\mathrm{N}} = \mathbb{E}\{\mathbf{x}_k^{\mathrm{N}} | \mathbf{y}_{0:k}\} \approx \sum_{i=1}^{N} w_{k,i} \mathbf{x}_{k,i}^{\mathrm{N}} \tag{3.31a}$$

$$\hat{\mathbf{x}}_{k|k}^{\mathrm{L}} = \mathbb{E}\{\mathbf{x}_k^{\mathrm{L}} | \mathbf{y}_{0:k}\} \approx \sum_{i=1}^{N} w_{k,i} \underbrace{\mathbb{E}\{\mathbf{x}_k^{\mathrm{L}} | \mathbf{x}_{0:k,i}^{\mathrm{N}}, \mathbf{y}_{0:k}\}}_{\hat{\mathbf{x}}_{k|k,i}^{\mathrm{L}}}. \tag{3.31b}$$

At a first glance, it looks like the estimate of the nonlinear states is independent from the linear states. However, eq. 3.31a shows an implicit dependency on the linear states since the conditional mean and covariance functions enter the update equation for the importance weights. Before focusing on the computation of the importance weights, the recursions for the computation of the conditional mean values $\hat{\mathbf{x}}_{k|k,i}^{\mathrm{L}}$ will be presented first [70].

Let us start to derive the update equations for the prediction and posterior mean and covariance functions by claiming that the conditional marginal posterior density at time instant $k = 0$ is a Gaussian probability density function according to $p(\mathbf{x}_0^{\mathrm{L}}|\mathbf{x}_0^{\mathrm{N}}, \mathbf{y}_0) = \mathcal{N}\left(\mathbf{x}_0^{\mathrm{L}}; \hat{\mathbf{x}}_{0|0}^{\mathrm{L}}(\mathbf{x}_0^{\mathrm{N}}), \mathbf{P}_{0|0}(\mathbf{x}_0^{\mathrm{N}})\right)$. Hence, according to the definition of the mixed linear/nonlinear state space model $p(\mathbf{x}_{k-1}^{\mathrm{L}}|\mathbf{x}_{0:k-1}^{\mathrm{N}}, \mathbf{y}_{0:k-1})$ is also Gaussian with mean and covariance functions $\hat{\mathbf{x}}_{k-1|k-1}^{\mathrm{L}}(\mathbf{x}_{0:k-1}^{\mathrm{N}})$ and $\mathbf{P}_{k-1|k-1}(\mathbf{x}_{0:k-1}^{\mathrm{N}})$, respectively. The state transition density function defined by the model (eq. 3.26 and eq. 3.27) is given by

$$p(\mathbf{x}_k^{\mathrm{N}}, \mathbf{x}_k^{\mathrm{L}}|\mathbf{x}_{k-1}^{\mathrm{N}}, \mathbf{x}_{k-1}^{\mathrm{L}}) = \mathcal{N}\left(\begin{bmatrix}\mathbf{x}_k^{\mathrm{N}}\\ \mathbf{x}_k^{\mathrm{L}}\end{bmatrix}; \boldsymbol{\alpha}_{k-1}(\mathbf{x}_{k-1}^{\mathrm{N}}), \mathbf{Q}_{k-1}(\mathbf{x}_{k-1}^{\mathrm{N}})\right) \tag{3.32a}$$

where the mean function at time step k is given by

$$\boldsymbol{\alpha}_k(\mathbf{x}_k^{\mathrm{N}}) = \begin{bmatrix}\mathbf{f}_{k-1}^{\mathrm{N}}(\mathbf{x}_{k-1}^{\mathrm{N}})\\ \mathbf{f}_{k-1}^{\mathrm{L}}(\mathbf{x}_{k-1}^{\mathrm{N}})\end{bmatrix} + \begin{bmatrix}\mathbf{A}_{k-1}^{\mathrm{N}}(\mathbf{x}_{k-1}^{\mathrm{N}})\\ \mathbf{A}_{k-1}^{\mathrm{L}}(\mathbf{x}_{k-1}^{\mathrm{N}})\end{bmatrix}\mathbf{x}_{k-1}^{\mathrm{L}}. \tag{3.32b}$$

Due to Markov properties of the state space model, the conditional probability density function $p(\mathbf{x}_k^{\mathrm{N}}, \mathbf{x}_k^{\mathrm{L}}|\mathbf{x}_{0:k-1}^{\mathrm{N}}, \mathbf{x}_{k-1}^{\mathrm{L}}, \mathbf{y}_{0:k-1})$ equals the state transition density. Since Gaussianity is preserved by affine transformations, this probability density function can be used in combination with $p(\mathbf{x}_{k-1}^{\mathrm{L}}|\mathbf{x}_{0:k-1}^{\mathrm{N}}, \mathbf{y}_{0:k-1})$ to derive the following conditional probability density function by applying lemma A.1.1 (see Appendix A)

$$p(\mathbf{x}_k^{\mathrm{N}}, \mathbf{x}_k^{\mathrm{L}}|\mathbf{x}_{0:k-1}^{\mathrm{N}}, \mathbf{y}_{0:k-1}) = \mathcal{N}\left(\begin{bmatrix}\mathbf{x}_k^{\mathrm{N}}\\ \mathbf{x}_k^{\mathrm{L}}\end{bmatrix}; \begin{bmatrix}\boldsymbol{\beta}_{k|k-1}^{\mathrm{N}}(\mathbf{x}_{0:k-1}^{\mathrm{N}})\\ \boldsymbol{\beta}_{k|k-1}^{\mathrm{L}}(\mathbf{x}_{0:k-1}^{\mathrm{N}})\end{bmatrix}, \mathbf{S}_{k|k-1}(\mathbf{x}_{0:k-1}^{\mathrm{N}})\right) \tag{3.33a}$$

with the mean functions

$$\boldsymbol{\beta}_{k|k-1}^{\mathrm{N}}(\mathbf{x}_{0:k-1}^{\mathrm{N}}) = \mathbf{f}_{k-1}^{\mathrm{N}}(\mathbf{x}_{k-1}^{\mathrm{N}}) + \mathbf{A}_{k-1}^{\mathrm{N}}(\mathbf{x}_{k-1}^{\mathrm{N}})\hat{\mathbf{x}}_{k-1|k-1}^{\mathrm{L}}(\mathbf{x}_{0:k-1}^{\mathrm{N}}) \tag{3.33b}$$

$$\boldsymbol{\beta}_{k|k-1}^{\mathrm{L}}(\mathbf{x}_{0:k-1}^{\mathrm{N}}) = \mathbf{f}_{k-1}^{\mathrm{L}}(\mathbf{x}_{k-1}^{\mathrm{N}}) + \mathbf{A}_{k-1}^{\mathrm{L}}(\mathbf{x}_{k-1}^{\mathrm{N}})\hat{\mathbf{x}}_{k-1|k-1}^{\mathrm{L}}(\mathbf{x}_{0:k-1}^{\mathrm{N}}) \tag{3.33c}$$

and covariance function

$$\begin{aligned}\mathbf{S}_{k|k-1}(\mathbf{x}_{0:k-1}^{\mathrm{N}}) &= \begin{bmatrix}\mathbf{A}_{k-1}^{\mathrm{N}}(\mathbf{x}_{k-1}^{\mathrm{N}})\\ \mathbf{A}_{k-1}^{\mathrm{L}}(\mathbf{x}_{k-1}^{\mathrm{N}})\end{bmatrix}\mathbf{P}_{k-1|k-1}(\mathbf{x}_{0:k-1}^{\mathrm{N}})\begin{bmatrix}\mathbf{A}_{k-1}^{\mathrm{N}}(\mathbf{x}_{k-1}^{\mathrm{N}})\\ \mathbf{A}_{k-1}^{\mathrm{L}}(\mathbf{x}_{k-1}^{\mathrm{N}})\end{bmatrix}^T + \mathbf{Q}_{k-1}(\mathbf{x}_{k-1}^{\mathrm{N}})\\ &= \begin{bmatrix}\mathbf{S}_{k|k-1}^{\mathrm{NN}}(\mathbf{x}_{0:k-1}^{\mathrm{N}}) & \mathbf{S}_{k|k-1}^{\mathrm{NL}}(\mathbf{x}_{0:k-1}^{\mathrm{N}})\\ \left(\mathbf{S}_{k|k-1}^{\mathrm{NL}}(\mathbf{x}_{0:k-1}^{\mathrm{N}})\right)^T & \mathbf{S}_{k|k-1}^{\mathrm{LL}}(\mathbf{x}_{0:k-1}^{\mathrm{N}})\end{bmatrix}.\end{aligned} \tag{3.33d}$$

By applying the rules for marginalization and conditioning for Gaussian multivariate probability densities (see lemma A.1.2 in Appendix A), the probability density functions

$$p(\mathbf{x}_k^{\mathrm{N}}|\mathbf{x}_{0:k-1}^{\mathrm{N}}, \mathbf{y}_{0:k-1}) = \mathcal{N}\left(\mathbf{x}_k^{\mathrm{N}}; \boldsymbol{\beta}_{k|k-1}^{\mathrm{N}}(\mathbf{x}_{0:k-1}^{\mathrm{N}}), \mathbf{S}_{k|k-1}^{\mathrm{NN}}(\mathbf{x}_{0:k-1}^{\mathrm{N}})\right) \tag{3.34}$$

and

$$p(\mathbf{x}_k^{\mathrm{L}}|\mathbf{x}_{0:k}^{\mathrm{N}}, \mathbf{y}_{0:k-1}) = \mathcal{N}\left(\mathbf{x}_k^{\mathrm{L}}; \hat{\mathbf{x}}_{k|k-1}^{\mathrm{L}}(\mathbf{x}_{0:k}^{\mathrm{N}}), \mathbf{P}_{k|k-1}(\mathbf{x}_{0:k-1}^{\mathrm{N}})\right) \tag{3.35a}$$

can be derived, whereby the mean and covariance functions of the conditional marginal prediction density $p(\mathbf{x}_k^{\mathrm{L}}|\mathbf{x}_{0:k}^{\mathrm{N}}, \mathbf{y}_{0:k-1})$ are given by

$$\hat{\mathbf{x}}_{k|k-1}^{\mathrm{L}}(\mathbf{x}_{0:k}^{\mathrm{N}}) = \boldsymbol{\beta}_{k|k-1}^{\mathrm{L}}(\mathbf{x}_{0:k-1}^{\mathrm{N}}) + \mathbf{L}_k(\mathbf{x}_{0:k-1}^{\mathrm{N}}) \left(\mathbf{x}_k^{\mathrm{N}} - \boldsymbol{\beta}_{k|k-1}^{\mathrm{N}}(\mathbf{x}_{0:k-1}^{\mathrm{N}})\right) \tag{3.35b}$$

$$\mathbf{P}_{k|k-1}(\mathbf{x}_{0:k-1}^{\mathrm{N}}) = \mathbf{S}_{k|k-1}^{\mathrm{LL}}(\mathbf{x}_{0:k-1}^{\mathrm{N}}) - \mathbf{L}_k(\mathbf{x}_{0:k-1}^{\mathrm{N}})\mathbf{S}_{k|k-1}^{\mathrm{NL}}(\mathbf{x}_{0:k-1}^{\mathrm{N}}) \tag{3.35c}$$

$$\mathbf{L}_k(\mathbf{x}_{0:k-1}^{\mathrm{N}}) = \left(\mathbf{S}_{k|k-1}^{\mathrm{NL}}(\mathbf{x}_{0:k-1}^{\mathrm{N}})\right)^T \left(\mathbf{S}_{k|k-1}^{\mathrm{NN}}(\mathbf{x}_{0:k-1}^{\mathrm{N}})\right)^{-1}. \tag{3.35d}$$

Obviously, the mean and covariance functions show similarities to the recursions obtained by a Kalman filter time update. This circumstance is not surprising since the conditional marginal posterior density is restricted to be Gaussian. However, there is a difference compared to standard Kalman filtering, namely the terms associated with $\mathbf{L}_k(\mathbf{x}_{0:k-1}^{\mathrm{N}})$, which arise from the conditioning on the nonlinear state trajectory. The predicted mean value obtained by evaluating the state transition equation of the linear state (eq. 3.26a) is corrected by a term which evaluates the prediction of the nonlinear states at time instant k. As for the conditional linear process, $\mathbf{x}_k^{\mathrm{N}}$ can be interpreted as an measurement. By analogy with Kalman filtering, $\mathbf{L}_k(\mathbf{x}_{0:k-1}^{\mathrm{N}})$ plays the role of a Kalman gain. Therefore, this correction is sometimes denoted as "additional or extra measurement update."

Of course, $\mathbf{x}_k^{\mathrm{N}}$ is not known, thus, the calculation of the conditional mean and the covariance function conditioned on the nonlinear trajectory is not directly possible. However, this circumstance is not problematic since according to eq. 3.31b, the expectation values conditioned on the samples of the nonlinear trajectory are required. Hence, the recursions derived in this section hold if the conditioning on the nonlinear trajectory $\mathbf{x}_{0:k}^{\mathrm{N}}$ is replaced by the conditioning on the samples of the nonlinear trajectory $\mathbf{x}_{0:k,i}^{\mathrm{N}}$. Consequently, this sample must first be provided by the sequential importance sampler before the time update recursion can be completed.

However, in order to simplify the equations, $\mathbf{x}_k^{\mathrm{N}}$ is assumed to be available and the derivation of the $p\left(\mathbf{x}_k^{\mathrm{L}}|\mathbf{x}_{0:k}^{\mathrm{N}}, \mathbf{y}_{0:k}\right)$ is completed first before dealing with the issue of sampling. For this purpose, a measurement update must be performed which essentially conditions the conditional prediction density on all available observations at time instant k. With respect to the calculation of the posterior mean and covariance functions, the fact that the state space model is Markovian proves to be beneficial. Since $p\left(\mathbf{y}_k|\mathbf{x}_{0:k}^{\mathrm{N}}, \mathbf{x}_k^{\mathrm{L}}, \mathbf{y}_{0:k-1}\right)$ equals $p\left(\mathbf{y}_k|\mathbf{x}_k^{\mathrm{N}}, \mathbf{x}_k^{\mathrm{L}}\right)$, which is defined by the measurement model (eq. 3.26c), the conditional measurement prediction density can be derived by applying lemma A.1.1 with the equivalents $p\left(\mathbf{x}_k^{\mathrm{L}}|\mathbf{x}_{0:k}^{\mathrm{N}}, \mathbf{y}_{0:k-1}\right) \widehat{=} p(\mathbf{x})$, $p\left(\mathbf{y}_k|\mathbf{x}_{0:k}^{\mathrm{N}}, \mathbf{x}_k^{\mathrm{L}}, \mathbf{y}_{0:k-1}\right) \widehat{=} p(\mathbf{z}|\mathbf{x})$ and $p\left(\mathbf{y}_k|\mathbf{x}_{0:k}^{\mathrm{N}}, \mathbf{y}_{0:k-1}\right) \widehat{=} p(\mathbf{z})$ according to

$$p\left(\mathbf{y}_k|\mathbf{x}_{0:k}^{\mathrm{N}}, \mathbf{y}_{0:k-1}\right) = \mathcal{N}\left(\mathbf{y}_k; \hat{\mathbf{y}}_k(\mathbf{x}_{0:k}^{\mathrm{N}}), \mathbf{U}_k(\mathbf{x}_{0:k}^{\mathrm{N}})\right) \tag{3.36a}$$

where the mean and the covariance functions are given by

$$\hat{\mathbf{y}}_k(\mathbf{x}_{0:k}^{\mathrm{N}}) = \mathbf{h}_k(\mathbf{x}_k^{\mathrm{N}}) + \mathbf{C}_k(\mathbf{x}_k^{\mathrm{N}})\hat{\mathbf{x}}_{k|k-1}^{\mathrm{L}}(\mathbf{x}_{0:k}^{\mathrm{N}}) \tag{3.36b}$$

$$\mathbf{U}_k(\mathbf{x}_{0:k}^{\mathrm{N}}) = \mathbf{C}_k(\mathbf{x}_k^{\mathrm{N}})\mathbf{P}_{k|k-1}(\mathbf{x}_{0:k-1}^{\mathrm{N}})\mathbf{C}_k^T(\mathbf{x}_k^{\mathrm{N}}) + \mathbf{R}_k(\mathbf{x}_k^{\mathrm{N}}). \tag{3.36c}$$

By applying again lemma A.1.1 with the density equivalents $p\left(\mathbf{x}_k^{\mathrm{L}}|\mathbf{x}_{0:k}^{\mathrm{N}}, \mathbf{y}_{0:k-1}\right) \widehat{=} p(\mathbf{x})$, $p\left(\mathbf{y}_k|\mathbf{x}_{0:k}^{\mathrm{N}}, \mathbf{y}_{0:k-1}\right) \widehat{=} p(\mathbf{z})$ and $p\left(\mathbf{x}_k^{\mathrm{L}}|\mathbf{x}_{0:k}^{\mathrm{N}}, \mathbf{y}_{0:k}\right) \widehat{=} p(\mathbf{x}|\mathbf{z})$, the conditional posterior density is given by

$$p\left(\mathbf{x}_k^{\mathrm{L}}|\mathbf{x}_{0:k}^{\mathrm{N}}, \mathbf{y}_{0:k}\right) = \mathcal{N}\left(\mathbf{x}_k^{\mathrm{L}}; , \hat{\mathbf{x}}_{k|k}^{\mathrm{L}}(\mathbf{x}_{0:k}^{\mathrm{N}}), \mathbf{P}_{k|k}(\mathbf{x}_{0:k}^{\mathrm{N}})\right) \tag{3.37a}$$

where the mean and covariance functions are given by

$$\hat{\mathbf{x}}^{\mathrm{L}}_{k|k}(\mathbf{x}^{\mathrm{N}}_{0:k}) = \hat{\mathbf{x}}^{\mathrm{L}}_{k|k-1}(\mathbf{x}^{\mathrm{N}}_{0:k}) + \mathbf{K}_k(\mathbf{x}^{\mathrm{N}}_{0:k})\left(\mathbf{y}_k - \hat{y}_k(\mathbf{x}^{\mathrm{N}}_{0:k})\right) \tag{3.37b}$$

$$\mathbf{P}_{k|k}(\mathbf{x}^{\mathrm{N}}_{0:k}) = \mathbf{P}_{k|k-1}(\mathbf{x}^{\mathrm{N}}_{0:k-1}) - \mathbf{K}_k(\mathbf{x}^{\mathrm{N}}_{0:k})\mathbf{C}_k(\mathbf{x}^{\mathrm{N}}_{k})\mathbf{P}_{k|k-1}(\mathbf{x}^{\mathrm{N}}_{0:k-1}) \tag{3.37c}$$

$$\mathbf{K}_k(\mathbf{x}^{\mathrm{N}}_{0:k}) = \mathbf{P}_{k|k-1}(\mathbf{x}^{\mathrm{N}}_{0:k-1})\mathbf{C}^T_k(\mathbf{x}^{\mathrm{N}}_{k})\mathbf{U}^{-1}_k(\mathbf{x}^{\mathrm{N}}_{0:k}). \tag{3.37d}$$

Apparently, these recursions are identical with those associated with the measurement update in standard Kalman filtering.

As mentioned before, the trajectory of the nonlinear states is not directly available and is, thus, sampled by a sequential importance sampler. For this purpose, the proposal density is partitioned similar to the equations of native particle filtering shown above, according to

$$\gamma_k(\mathbf{x}^{\mathrm{N}}_{0:k}|\mathbf{y}_{0:k}) = \eta_k(\mathbf{x}^{\mathrm{N}}_{k}|\mathbf{x}^{\mathrm{N}}_{0:k-1}, \mathbf{y}_{0:k})\gamma_{k-1}(\mathbf{x}^{\mathrm{N}}_{0:k-1}|\mathbf{y}_{0:k-1}) \tag{3.38}$$

where N samples are drawn according to $\mathbf{x}^{\mathrm{N}}_{k,i} \sim \eta_k(\mathbf{x}^{\mathrm{N}}_{k}|\mathbf{x}^{\mathrm{N}}_{0:k-1,i}, \mathbf{y}_{0:k})$. Hence, the i^{th} importance weight can be recursively updated according to

$$w_{k,i} = \frac{p\left(\mathbf{x}^{\mathrm{N}}_{0:k,i}|\mathbf{y}_{0:k}\right)}{\gamma_k\left(\mathbf{x}^{\mathrm{N}}_{0:k,i}|\mathbf{y}_{0:k}\right)} \propto \lambda_{k,i}\underbrace{\frac{p\left(\mathbf{x}^{\mathrm{N}}_{0:k-1,i}|\mathbf{y}_{0:k-1}\right)}{\gamma_{k-1}(\mathbf{x}^{\mathrm{N}}_{0:k-1,i}|\mathbf{y}_{0:k-1})}}_{=w_{k-1,i}} \tag{3.39a}$$

where the innovation term is given by

$$\lambda_{k,i} = \frac{p\left(\mathbf{y}_k|\mathbf{x}^{\mathrm{N}}_{0:k,i}, \mathbf{y}_{0:k-1}\right) p\left(\mathbf{x}^{\mathrm{N}}_{k,i}|\mathbf{x}^{\mathrm{N}}_{0:k-1,i}, \mathbf{y}_{0:k-1}\right)}{\eta_k(\mathbf{x}^{\mathrm{N}}_{k,i}|\mathbf{x}^{\mathrm{N}}_{0:k-1,i}, \mathbf{y}_{0:k})}. \tag{3.39b}$$

The innovation term can significantly be simplified if the one-step predictive density $p\left(\mathbf{x}^{\mathrm{N}}_{k}|\mathbf{x}^{\mathrm{N}}_{0:k-1}, \mathbf{y}_{0:k-1}\right)$ (see eq. 3.34) is chosen for the proposal density η_k. Essentially, this is directly analogous to the bootstrapping approach mentioned when discussing the native particle filter.

Finally, we are now in the position to determine approximations of the sought expectation values (eq. 3.31a and eq. 3.31b). The variance of the estimates is guaranteed lower than or equal to the variance obtained by a native particle filter. However, this gain in performance involves higher computational demands. This circumstance is due to the fact that with every time step N individual conditional posterior densities must be calculated, each of them conditioned on an individual trajectory of the nonlinear states $\mathbf{x}^{\mathrm{N}}_{0:k}$. In other words, at every time step, N Kalman filter-like algorithms must be computed. Since Rao-Blackwellized particle filtering utilizes a sequential importance sampling scheme and targets a smoothing posterior density, the algorithm suffers, similar to the native particle filter, from the sample degeneracy problem. Hence, resampling is necessary. In contrast to the native particle filter, prediction and a posterior mean vectors and covariances are associated with each individual particle. As a consequence, these quantities must be taken into consideration when the resampling step is done.

3.2. Validation Data

As already stated several times, the problems associated with the $LiFePO_4$ battery's characteristic flat and ambiguous mapping between the SOC and the open circuit voltage U_{OCV} prove to be challenging if the task is to estimate the battery's SOC in an application which relies on short and consecutive charge and discharge quantities. Since hybrid electric vehicle drive trains belong to this class of applications, driving cycles developed to examine the power flow in these drive trains are accordingly ideally suited to validate the performance of the proposed estimator, which will be shown in the upcoming section.

In order to meet the operating conditions in a hybrid electric vehicle drive train, the course of the battery's operating current, required for validation, is derived by the analysis of the power flow of an according drive train simulation. Thereby a backward simulation was performed by means of velocity profiles corresponding to the Braunschweig, Manhatten and ARTEMIS-urban driving cycle, respectively. This choice of velocity profiles is due to the fact that these driving cycles were developed to emulate the velocity profile of urban traffic situations. Since urban traffic is associated with short and consecutive acceleration and recuperation (braking) periods, the battery's open circuit voltage U_{OCV} is assumed to steadily move from one open circuit voltage curve to the other. This is exactly the desired behavior to validate the model of the open circuit voltage U_{OCV} presented in chapter 2. Figure 3.7 depicts the velocity profiles as well as the obtained courses of the battery operating current corresponding to the three investigated driving cycles.

For the simulation of the power flows, a simple drive train model was used which roughly models the dynamics of a Volvo 7900 hybrid electric bus. In order to cover a wide range of the battery's SOC, the following control strategy was chosen for the backward simulation. The simulation started with the battery being 80% charged. For the first period, the required power was preferably taken from the battery until the SOC drops below 30%. During this period, the power used for charging the battery was entirely generated by recuperation. Afterwards, the combustion engine was preferably used and the battery was on average charged. This control strategy entailed that the SOC on average changed from 80% to 30% and back to almost 80%, but performed oscillations which caused the open circuit voltage U_{OCV} permanently to move from one open circuit voltage curve to the other.

The courses of the battery's operating current derived by backward simulation will be later used for the validation of the proposed estimator. In a first step, the feasibility of the Rao-Blackwellized estimation framework will be investigated by means of a simulation study. Furthermore, the estimator's performance will be validated by means of measured data records which were obtained by the experimental evaluating the mentioned current courses in the lab. Similar to the experiments presented in the previous chapter, an A123 26650m1-B $LiFePO_4$ battery was investigated by means of the custom battery testing units developed at the Institute of Electrical Measurement and Measurement Signal Processing [46].

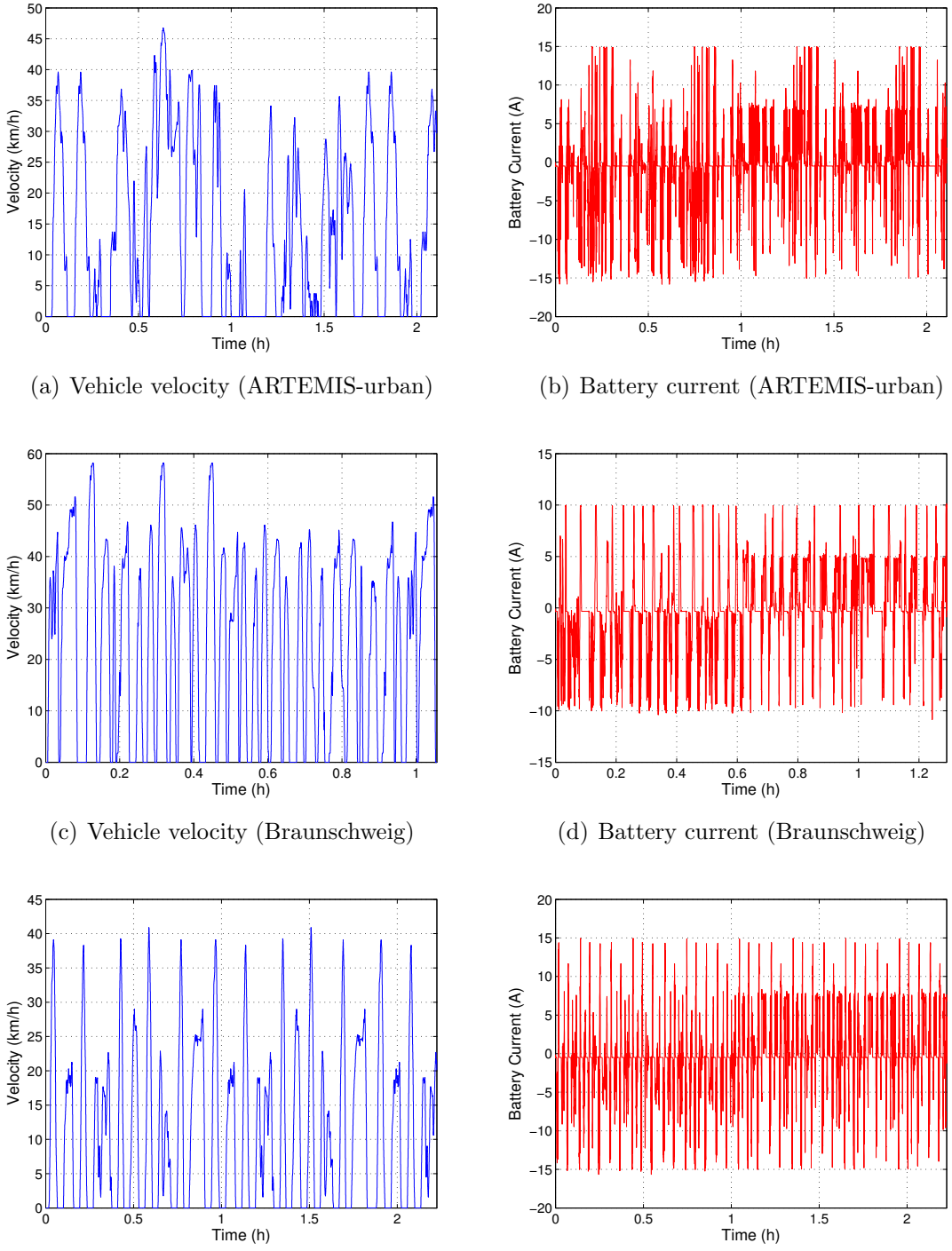

(a) Vehicle velocity (ARTEMIS-urban)

(b) Battery current (ARTEMIS-urban)

(c) Vehicle velocity (Braunschweig)

(d) Battery current (Braunschweig)

(e) Vehicle velocity (Manhatten)

(f) Battery current (Manhatten)

Figure 3.7.: Velocity profiles (left) and corresponding battery operating current (right) derived by power flow analyses of a hybrid electric vehicle drive train. The shown velocity profiles correspond to the ARTEMIS-urban, Braunschweig and Manhatten driving cycle and were used to perform backward simulations by means of a simplified dynamic model of the Volvo 7900 hybrid electric bus drive train.

3.3. Rao-Blackwellized Particle Filtering for Condition Monitoring

Dynamic Battery Model

In order to adopt the Rao-Blackwellized framework to the problem of SOC estimation, the battery's dynamics must be modeled by a conditional linear Gaussian state space model (CLGSSM). In section 2, it was highlighted that hysteresis phenomena have a distinct influence on the open circuit voltage U_{OCV}. Hence, this circumstance is considered to model the battery's terminal voltage according to

$$U_{\mathrm{term}} = U_{\mathrm{OCV}} + U_{\mathrm{trans}} \tag{3.40}$$

where eq. 2.1 is used to model the open circuit voltage and U_{trans} corresponds to the transient voltage contribution. The latter is obtained by a first order biproper linear subsystem. The parameters of this linear subsystem are allowed to vary with respect to time, which is in consistency with the adaptive approaches presented e.g. in [20–22,71,72] where the battery's transient dynamics is modeled by an RC-parallel circuit connected in series with an ohmic resistor. However, the interpretation of the linear subsystem by an equivalent circuit model can be quite misleading since the lumped components appear to be in an unphysical range. Consequently, it will be refrained from explicitly parameterizing equivalent circuits, and the model of the transient dynamics is parameterized by its eigenvalue β, the gain parameter γ and the feedthrough parameter d.

By defining $y(t) = U_{\mathrm{term}}(t)$ and $u(t) = i(t)$, the state space representation of the battery's dynamics in the discrete time domain is given by

$$\mathbf{x}_{k+1} = \begin{bmatrix} 1 & 0 & 0 \\ 0 & 1 & 0 \\ 0 & 0 & e^{\beta_k T_s} \end{bmatrix} \mathbf{x}_k + \begin{bmatrix} \frac{Ts}{C_n} \\ \alpha_k T_s \left(1 - \operatorname{sign}(u_k) x_{2,k}\right) \\ \gamma_k \left(1 - e^{\beta_k T_s}\right) \end{bmatrix} u_k \tag{3.41}$$

$$y_k = U_{\mathrm{OCV,avg}}(x_{1,k}) + U_{\mathrm{OCV,diff}}(x_{1,k}) x_{2,k} + x_{3,k} + d u_k \tag{3.42}$$

where T_s denotes the sampling period. The nominal capacity is given by C_n and the state vector $\mathbf{x}_k$ is composed of the SOC, the hysteresis state (see eq. 2.6) and a transient state associated with the linear time variant subsystem. In addition to the sample period T_s, the nominal capacity C_n is assumed to be known a priori. This assumption is due to the fact that by investigating the battery's open circuit voltage U_{OCV} (see section 2), the open circuit voltage charge and discharge curves were experimentally determined. For the given dynamic model, the difference of the charge levels associated with maximum and minimum open circuit voltage U_{OCV} equals the nominal capacity C_n. Admittedly, this is a slight abuse of notation since C_n represents rather a maximum value than a typical or minimum guaranteed value usually stated by the manufacturer. The other parameters are not known a priori and are assumed to vary with respect to SOC and temperature. In addition, the used dynamic model (and especially the linear subsystem) is too simple to cover the battery's entire nonlinear dynamics. In order to deal with these dependencies and imperfections, the unknown parameters are allowed to vary with respect to time and are incorporated in the estimation framework by the definition of the parameter

vector according to

$$\boldsymbol{\theta}_k = \left[\alpha_k T_s, e^{\beta_k T_s}, \gamma_k \left(1 - e^{\beta_k T_s}\right), d_k\right]^T. \tag{3.43}$$

Since the parameter vector linearly enters eq. 3.41 and eq. 3.42 and the random walk model used to update the parameter vector is linear, the proposed state space model is a conditional linear Gaussian space state model (GLGSSM) and can be rewritten in the desired form (see eq. 3.26a - eq. 3.26c) according to

$$\mathbf{x}_{k+1} = \underbrace{\begin{bmatrix} x_{1,k} + \frac{Ts}{C_n} \\ x_{2,k} \\ 0 \end{bmatrix}}_{\widehat{=}\mathbf{f}_k^{\mathrm{N}}} + \underbrace{\begin{bmatrix} 0 & 0 & 0 & 0 \\ (1 - \mathrm{sign}(u_k) x_{2,k})\, u_k & 0 & 0 & 0 \\ 0 & x_{3,k} & u_k & 0 \end{bmatrix}}_{\widehat{=}\mathbf{A}_k^{\mathrm{N}}} \boldsymbol{\theta}_k + \mathbf{w}_k^{\mathbf{x}} \tag{3.44}$$

$$\boldsymbol{\theta}_{k+1} = \underbrace{\mathbf{0}}_{\widehat{=}\mathbf{f}_k^{\mathrm{L}}} + \underbrace{\mathbf{I}}_{\widehat{=}\mathbf{A}_k^{\mathrm{L}}} \boldsymbol{\theta}_k + \mathbf{w}_k^{\boldsymbol{\theta}} \tag{3.45}$$

$$y_k = \underbrace{U_{\mathrm{OCV,avg}}(x_{1,k}) + U_{\mathrm{OCV,diff}}(x_{1,k}) x_{2,k} + x_{3,k}}_{\widehat{=}h_k} + \underbrace{\begin{bmatrix} 0 & 0 & 0 & u_k \end{bmatrix}}_{\widehat{=}\mathbf{C}_k} \boldsymbol{\theta}_k + v_k \tag{3.46}$$

where the state vector $\mathbf{x}_k$ and the parameter vector $\boldsymbol{\theta}_k$ correspond to the nonlinear states $\mathbf{x}_k^{\mathrm{N}}$ and linear states $\mathbf{x}_k^{\mathrm{L}}$, respectively. Hence, this formulation makes the problem of SOC estimation accessible for the Rao-Blackwellized framework for particle filtering shown in section 3.1.3.

Estimation Algorithm

Before proceeding with the validation of the performance of the proposed estimator, a proposal density must be chosen first. The choice

$$\eta_k(\mathbf{x}_{k,i} | \mathbf{x}_{0:k-1,i}, y_{0:k}) = p(\mathbf{x}_k | \mathbf{x}_{0:k-1}, y_{0:k-1}) \tag{3.47}$$

entails that the innovation term $\lambda_{k,i}$ (see eq. 3.39b) is reduced to

$$\begin{aligned} \lambda_{k,i} &= p\left(\mathbf{y}_k | \mathbf{x}_{0:k,i}, y_{0:k-1}\right) \\ &= \mathcal{N}\left(y_k; h_k\left(\mathbf{x}_{k,i}\right) + \mathbf{C}_k\left(u_k\right) \hat{\boldsymbol{\theta}}_{k|k-1,i}, \mathbf{C}_k\left(u_k\right) \mathbf{P}_{k|k-1,i} \mathbf{C}_k^T\left(u_k\right) + R_k\right). \end{aligned} \tag{3.48}$$

As mentioned before, this choice of the proposal density is directly analogous to the choice of the proposal density in bootstrapping. The benefits of this choice are obvious: Instead of the evaluation three probability density functions, only the measurement prediction density must be evaluated. Since the innovation term must be calculated for every individual particle, the reduction of the computational demands can be significant. Of course, this simplification has consequences since the 1-step predictive density might not be the best choice for the proposal density. This circumstance is due to the fact that the information of the current measurement y_k is not incorporated in this proposal density. In order to circumvent this problem, some authors suggest a construction of the proposal kernel based on local linearization of the measurement equation, incorporating the information of the current measurement (see e.g. Doucet [66] or Lindesten [70]). However, since this procedure significantly increases the computational demands of the algorithm, it will be refrained from adopting this concept for the proposal construction herein.

With respect to the expression of the update of the importance weights, eq. 3.39a is slightly modified given by

$$w_{k,i} \propto \lambda_{k,i}\kappa(\mathbf{x}_{k,i})w_{k-1,i} \tag{3.49}$$

where $\kappa(\mathbf{x})$ is an indicator function and is defined as

$$\kappa(\mathbf{x}) = \begin{cases} 1 & \text{if } 0 \leq x_1 \leq 1 \text{ and } -1 \leq x_2 \leq 1 \\ 0 & \text{else} \end{cases}. \tag{3.50}$$

This approach can be interpreted by incorporating prior knowledge in the recursion of the weight update. The SOC is per definition a positive quantity and limited to 1. Moreover, the hysteresis state is limited to ± 1. Violating the first condition is of minor relevance for the performance of the estimator since the missing values of $U_{\mathrm{OCV,avg}}$ and $U_{\mathrm{OCV,diff}}$ can be obtained by extrapolation. However, if the second condition is violated, the trajectory of the hysteresis state becomes unstable and quickly diverges. Although diverging paths correspond to small values of the measurement prediction density and are therefore replaced by the mutation step (resampling), it was observed that the Rao-Blackwellized particle filter converges to a highly biased estimate. The role of the indicator function $\kappa(\mathbf{x})$ can be interpreted by restricting the support of the measurement prediction density to valid values with respect to x_1 and x_2. By applying this measure, the Gaussianity of the measurement prediction equation is lost and the equations of the Rao-Blackwellized particle filter derived above do not hold anymore. In practice, this circumstance is of minor relevance, and by applying the explained measure, the performance of the estimator increases significantly.

The stability of the dynamic model $x_{2,k}$ is tightly coupled to $\theta_{1,k}$, thus, it is mandatory that $\theta_{1,k}$ takes a positive value. Since the estimate of the parameters implicitly implies Gaussian distributions, it is challenging to guarantee that this constraint will not be violated. Although the possibility of Kalman filtering with inequality constraints exists (see [73–76]), the computational demands would be immense for the Rao-Blackwellized particle filter framework, since an individual inequality constraint optimization problem must be solved for every particle at every single time step. By incorporating the indicator function, the N individual Kalman filter-like estimators used to adapt the parameter vector are hampered to estimate negative values for $\theta_{1,k}$ since negative values cause the individual trajectories of the hysteresis state to diverge quickly. According to the explanation above, zero weight is assigned to the corresponding particles while the diverging paths are replaced in the resampling step.

So far little attention was drawn to the resampling procedure. In accordance with the introducing section, it will be refrained from going into details of resampling. Interested parties may refer to [61–63]. Nevertheless, the necessity of resampling to avoid sample degeneracy is emphasized. In the present case, a resampling step is carried out if the effective sample size N_{eff} (see eq. 3.16) drops below a certain threshold N_t. As resampling procedure, systematic resampling was chosen for the proposed estimator since it is easy to implement, and the computational complexity is $\mathcal{O}(N)$. Algorithm 1 illustrates the concept of systematic resampling for the present case.

Algorithm 1 Systematic Resampling

pick a random sample $r_k \sim \mathcal{U}(0,1)$
calculate cumulative weight vector $\mathbf{q}$ and comparison vector $\mathbf{p}$
for $i = 1 : N$ **do**
  $q_i = \sum_{n=1}^{i} w_{k,i}$
  $p_i = \frac{i-1+r}{N}$
end for
initialize index candidate $l = 1$
for $i = 1 : N$ **do**
  while $q_l < p_i$ **do**
    $l = l + 1$
  end while
  set resampling index $j_i = l$
end for
resample state vectors, posterior mean values and posterior covariances
for $i = 1 : N$ **do**
  $\mathbf{x}_{k,i} = \mathbf{x}_{k,j_i}$
  $\boldsymbol{\theta}_{k|k,i} = \boldsymbol{\theta}_{k|k,j_i}$
  $\mathbf{P}_{k|k,i} = \mathbf{P}_{k|k,j_i}$
  assign uniform weight $w_{k,i} = \frac{1}{N}$
end for

3.3.1. Simulation Studies

In order to verify the suitability of the proposed estimation framework for SOC estimation of $LiFePO_4$ batteries, a simulation study was carried out. According to section 3.2, the current signal as well as the available temperature signals of the experimentally determined driving cycle records were used to simulate the battery's terminal voltage U_{term}. As mentioned before, the parameter vector $\boldsymbol{\theta}$ is assumed to vary with respect to the SOC and the temperature. The latter dependency can be argued that one of the main contributions to the transport of the charged species between the electrodes is diffusion. The rate of diffusion is strongly influenced by the ionic conductivity of the electrolyte which itself is strongly influenced by the temperature: the higher the temperature, the faster the transport of the charged species. In section 2, it was mentioned that the influence of the temperature on the battery's open circuit voltage U_{OCV} proved to be negligible for the investigated $LiFePO_4$ battery. Hence, it is assumed that the temperature dependency of the battery's terminal voltage U_{term} is entirely covered by the transient voltage contribution U_{trans}, represented by the linear subsystem.

Since it is not within the scope of this thesis to develop novel models for the temperature dependency of the terminal voltage U_{term}, a simple temperature model is used for simulation which is basically motivated by the principles of reaction kinetics expressed by the Arrhenius equation. Adopted to the linear subsystem, this dependency is incorporated by a temperature-dependent eigenvalue. By analogy with the widespread RC-models, this relates to an according time constant which is

modeled as a function of the temperature ϑ according to

$$\tau(\vartheta) = \exp\left(\ln(\tau_{20}) - \frac{\ln(0.5)}{\frac{293}{303} - 1}\right) \exp\left(\frac{\ln(0.5)}{\frac{\vartheta}{303} - \frac{\vartheta}{293}}\right) \tag{3.51}$$

where τ_{20} denotes the time constant at 20 °C and is chosen to be 12 s. Basically, eq. 3.51 provides that the time constant $\tau(\vartheta)$ is approximately halved per 10 °C increase of temperature. The functional relationship of the parameter vector $\boldsymbol{\theta}$ used for simulation is given by

$$\theta_{1,k} = 4e^{-4}\left(1 - x_{1,k}\right) \tag{3.52a}$$

$$\theta_{2,k} = \exp\left(-\frac{T_s}{\tau(\vartheta_k)}\right) \tag{3.52b}$$

$$\theta_{3,k} = 15e^{-3}\left(1 - \exp\left(-\frac{T_s}{\tau(\vartheta_k)}\right)\right) \tag{3.52c}$$

$$\theta_{4,k} = \frac{1e^{-3}}{\vartheta_k} \tag{3.52d}$$

where the hysteresis gain θ_1 is assumed to vary with respect to the SOC. θ_2 and θ_3 represent the eigenvalue and gain parameter of the linear subsystem, respectively. These parameters relate to the diffusion ratio and are therefore assumed to be functionally dependent on $\tau(\vartheta)$. By analogy with the widespread RC models, the feedthrough parameter θ_4 corresponds to a serial resistance. Since this parameter relates directly to the ionic conductivity, a reciprocal dependence on the temperature is assumed. To avoid confusion, it should be emphasized that these equations are solely used for simulation purposes and the proposed Rao-Blackwellized estimator utilizes a random walk model to update the estimate of the parameter vector $\boldsymbol{\theta}_k$.

Performance Evaluation for Unbiased Current Signals

In a first step, the performance of the proposed Rao-Blackwellized estimator was evaluated in the case of ideal measurements. For this purpose, the current signal obtained by the experimental evaluation of the three driving cycles (section 3.2) was directly used for the simulation of the trajectories of the state vector $\mathbf{x}_k$ and the terminal voltage U_{term} according to eq. 3.44 and eq. 3.46, respectively. For each experiment, the (cylindric) battery's temperature was measured on each face surface to approximately obtain the temperature on the current collector foils of both electrodes. The arithmetic average of these temperature signals and the simulated SOC were used to adapt the parameter vector $\boldsymbol{\theta}_k$.

As mentioned in the introducing section above, the Rao-Blackwellized particle filter uses the concept of sufficient statistics for estimating the conditionally linear states. Nevertheless, this estimator relies on statistical sampling. Thus, the estimator itself is a stochastic process and the performance of the estimator should also be accessed statistically. Hence, a Monte Carlo analysis was carried out to access the performance of the estimator for all three driving cycle records. Unfortunately, the size of every individual data record is huge and the proposed estimator is computationally costly. As a trade-off between computational demands and statistical power, the state and parameter courses were estimated in 50 individual trials for

every driving cycle record. Thereby, the size of the particle set was $N = 1000$ and the resampling threshold was set to $N_t = 900$. This size of the particle set proved to be reasonable for the initial conditions indicated below since attempts to solve the joint estimation problem by means of a significantly smaller particle set failed to converge. On the other hand, increasing the size of the particle set to multiples of thousands did not result in a noticeable improvement of the estimator's performance.

The estimator for the simulated terminal voltage was parameterized as follows. The i$^{\text{th}}$ initial particle $\mathbf{x}_{0,i} = \begin{bmatrix} x_{1,0,i} & x_{2,0,i} & x_{3,0,i} \end{bmatrix}^T$ was sampled according to

$$x_{1,0,i} \sim \mathcal{U}(0,1) \tag{3.53a}$$
$$x_{2,0,i} \sim \mathcal{U}(-1,1) \tag{3.53b}$$
$$x_{3,0,i} \sim \mathcal{N}(0,0.01)\,. \tag{3.53c}$$

This choice of the prior distribution of the particles relates to little prior knowledge since the support of the initial densities of the SOC $x_{1,0}$ and the hysteresis state $x_{2,0}$ are only limited to the valid range. With other words, with respect to $x_{1,0}$ and $x_{2,0}$, all possible values are equally likely to be sampled. The support of the prior distribution of the transient state $x_{3,0}$ is not known a priori. As the transient voltage contribution to the terminal voltage is expected to be in the range of millivolts, a zero-mean Gaussian distribution with a standard deviation of 100 mV is used for prior sampling.

The parameterization of the parameter prior distributions is less straightforward. On the one hand, there is little prior knowledge about the parameters available.[5] On the other hand, it is hardly possibly to restrict the support of the parameter distributions to valid ranges since the Rao-Blackwellized setting requires Gaussian distributions for the conditionally linear states. Hence, the prior mean values of the parameter vector are chosen according to

$$\boldsymbol{\theta}_{0|-1,i} = \begin{bmatrix} 0 & 0.9 & 0 & 0 \end{bmatrix}^T \tag{3.54a}$$

where the nontrivial value corresponds to a relatively slow relaxing transient state and proves to be necessarily nontrivial, positive and smaller than 1 to achieve convergence. The situation is even worse with respect to the according covariance matrix given by

$$\mathbf{P}_{0|-1,i} = \begin{bmatrix} 10^{-6} & 0 & 0 & 0 \\ 0 & 10^{-4} & 0 & 0 \\ 0 & 0 & 10^{-6} & 0 \\ 0 & 0 & 0 & 10^{-4} \end{bmatrix}, \tag{3.54b}$$

which was admittedly found through an empirical analysis. In native state estimation, little prior knowledge is usually expressed by large variance entries of the corresponding covariance matrix. However, in the case of the joint filtering problem presented herein, it was observed that the convergence rate drops rapidly if the prior

[5] Of course, the parameter courses are obtained by simulation and the initial conditions are therefore exactly known. However, the results of the simulation are used to prove the applicability of the RBPF estimator for SOC estimation. Thus, this prior knowledge is neglected since it is not available when the measured voltage course is investigated.

parameter covariance is too large. This is in agreement with the observations by Lindsten [70, 77] and is presumably caused by slow mixing properties of the used conditionally linear state space model [78–81].

The state and parameter process noise is assumed to be uncorrelated with constant state covariance given by

$$\mathbf{Q}_k^{\mathbf{xx}} = \begin{bmatrix} 10^{-8} & 0 & 0 \\ 0 & 10^{-8} & 0 \\ 0 & 0 & 10^{-6} \end{bmatrix} \tag{3.55a}$$

and time-variant parameter covariance according to

$$\mathbf{Q}_k^{\boldsymbol{\theta\theta}} = \begin{bmatrix} 10^{-12} + \frac{10^{-8}}{k} & 0 & 0 & 0 \\ 0 & 10^{-10} + \frac{10^{-6}}{k} & 0 & 0 \\ 0 & 0 & 10^{-10} + \frac{10^{-6}}{k} & 0 \\ 0 & 0 & 0 & 10^{-10} + \frac{10^{-6}}{k} \end{bmatrix}. \tag{3.55b}$$

The aim of the reciprocal time-dependent parts of the diagonal elements of $\mathbf{Q}_k^{\boldsymbol{\theta\theta}}$ is to add artificial dynamic evolution to the slow varying (or static) parameter states in order to achieve faster convergence of the parameter process. In the literature, this technique is often referred to as jittering or roughening (see e.g. Gordon et. al [64], Kitagawa [82] or Gustafsson and Schön [51]).

The last outstanding issue of the parameterization of the estimator is the variance of the Gaussian measurement noise v_k. In this context, the simulated terminal voltage was distorted by additive zero-mean white Gaussian noise with variance $R_k = 10^{-6}$, corresponding to relatively inaccurate voltage measurements. The choice of this measure is motivated by two facts. First, the direct usage of the simulated courses of the battery's terminal voltage is in contradiction to the actual purpose of simulation, namely validating whether the proposed estimator is applicable to estimate the SOC of real battery systems. Second, the used Rao-Blackwellized particle filter for joint estimation requires uncertain output measurements for its operation since the estimator tends to diverge quickly if the variance of the output measurement R_k is too small. This circumstance is due to the fact that according to eq. 3.48, the i$^{\text{th}}$ measurement prediction density $p\left(y_k|\mathbf{x}_{0:k,i}, y_{0:k-1}\right)$ is used to update the weight innovation term. If the parameter prediction covariance $\mathbf{P}_{k|k-1,i}$ decreases rapidly, the variance of this Gaussian density is mainly determined by the variance of the measurement noise R_k. As a consequence, if R_k is chosen to small, negligible importance weights are assigned to the particles which are not located in the immediate vicinity of the true state vector $\mathbf{x}_k$. Especially during the first recursions, the particles are (depending on their initial distribution) relatively widespread across the particle space. Thus, it is highly likely that there is no particle located in the immediate vicinity of the true state vector $\mathbf{x}_k$. In this case, negligible weight (zero due to machine precision) is assigned to all particles. As a consequence, the importance weights cannot be normalized anymore and the algorithm fails to assign a real number to the importance weights. Hence, the algorithm diverges since the weight update recursion can not be evaluated anymore and there are no particles left for the resampling procedure. Note that even if a few particles remain after the weight update, the number of these particles might not be large enough to avoid the

sample degeneracy problem by the selection step (resampling). Hence, increasing the measurement variance R_k entails that the measurement prediction density is broadened and the number of remaining particles is increased.

The results of the Monte Carlo studies assessing the performance of the proposed estimator for the simulated data assuming ideal current measurements are given below. The according SOC error courses, derived by the simulation of the state trajectories by means of the ARTEMIS-urban, the Braunschweig and the Manhatten driving cycle are shown in figures 3.8, 3.9 and 3.10, respectively. The blue lines depict the SOC error courses obtained by the individual estimation trials, while the red lines illustrate the average error course (solid) and the estimated 2σ confidence interval (dashed). With regard to the little prior knowledge gained through the parameterization of the estimator, the shown error courses promise a good detectability of the SOC. After a more or less slow converging period, the absolute value of the average error signal stays below 1% most of the time. According to the chosen prior distribution of the particles, every valid SOC value is equally likely sampled at the beginning of the recursion. Hence, the results prove that the proposed estimator is in principle capable of inferring the SOC from the simulated terminal voltage U_{term} despite the flat and ambiguous mapping between the SOC and the open circuit voltage U_{OCV}.

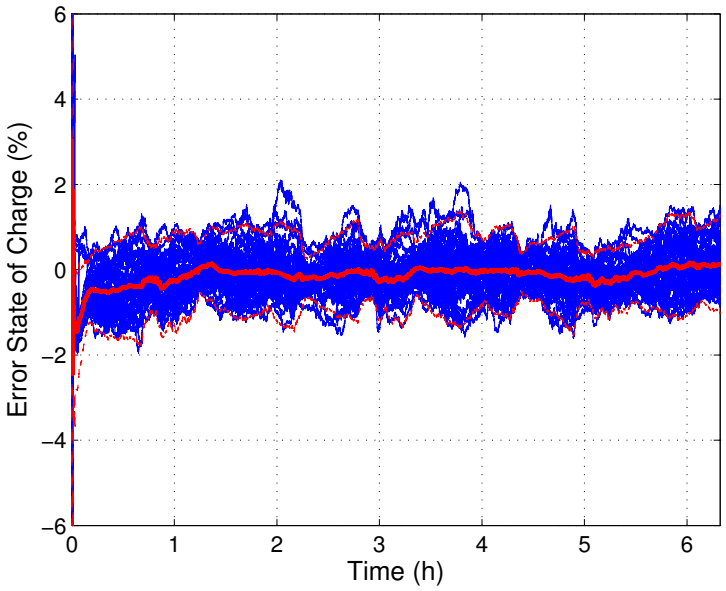

Figure 3.8.: Results of the Monte Carlo analysis to assess the performance of the RBPF estimator by estimating the course of the SOC simulated by means of an ideal current signal derived by the ARTEMIS-urban driving cycle. The blue lines show the individual error courses while the red lines depict the average error course (solid) and the estimated 2σ confidence interval (dashed) for 43 converging estimation trails.

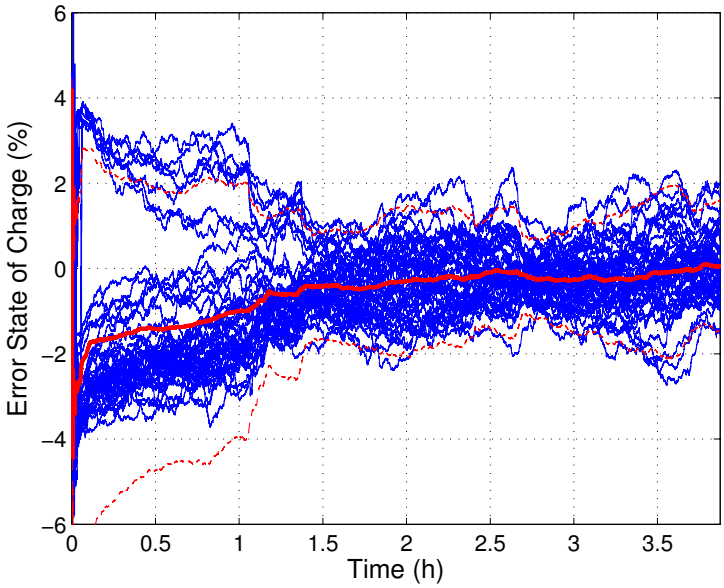

Figure 3.9.: Results of the Monte Carlo analysis to assess the performance of the RBPF estimator by estimating the course of the SOC simulated by means of an ideal current signal derived by the Braunschweig driving cycle. The blue lines show the individual error courses while the red lines depict the average error course (solid) and the estimated 2σ confidence interval (dashed) for 46 converging estimation trails.

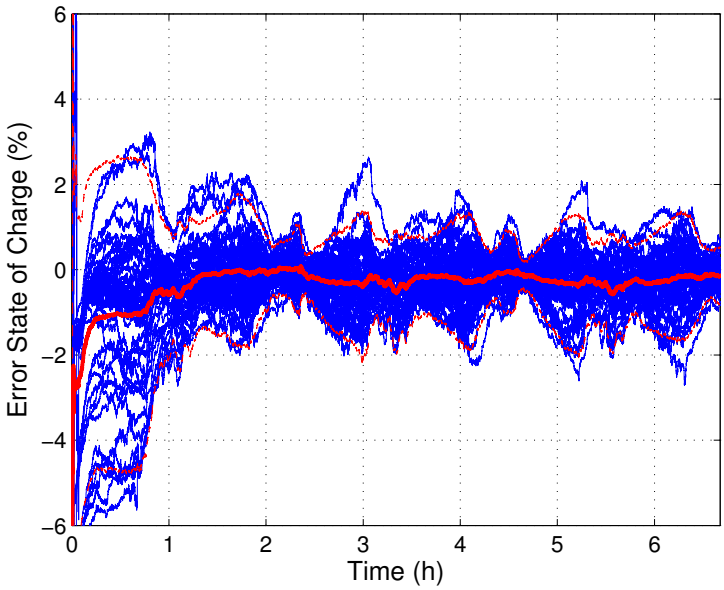

Figure 3.10.: Results of the Monte Carlo analysis to assess the performance of the RBPF estimator by estimating the course of the SOC simulated by means of an ideal current signal derived by the Manhatten driving cycle. The blue lines show the individual error courses while the red lines depict the average error course (solid) and the estimated 2σ confidence interval (dashed) for 48 converging estimation trails.

However, it should be mentioned that none of the three Monte Carlo studies concluded in converging estimates for all 50 trials. In case of the Monte Carlo analysis associated with the current signal derived from the ARTEMIS-urban driving cycle, the estimator failed to converge in seven trials. A slightly better convergence rate was obtained by the investigation of the Braunschweig driving cycle (four fails) and the Manhatten driving cycle (two fails). This result is not surprising since this estimator is based on statistical sampling and consequently suffers from the shortcomings of randomized estimators as mentioned in the introducing section. This is especially true for joint estimation since the parameter courses perform only small variations which correspond to relatively slow mixing properties of the state space model.[6] In addition, the random walk model used in the absence of alternatives is a poor update model for the simulated parameter courses. Both circumstances provide an explanation for the occasional divergence of the estimator.

However, it was observed that common to all of the "fail" cases is that the estimator diverges quickly after a few time steps. As far as engineering is concerned, there is, hence, the opportunity of simply restarting the estimator with new initial particles if the divergence of the estimator is detected.

Performance Evaluation for Inaccurate Current Measurements

The Monte Carlo analyses carried out above show that the proposed estimation framework is in principle capable of estimating the simulated SOC almost correctly independently of the charge/discharge quantities applied to the battery model. It was furthermore assumed that the true battery's operating current is available. However, this situation never occurs in practice and the battery's operating current $i(t)$ is obtained by measurements which are of course associated with a certain level of uncertainty. The accuracy of the measurement system might depend on various influences, like e.g. temperature or long-term drift, to name but a few. In addition to noise, the measurement suffers on a systematic error. Since the state update equation of the used state space model integrates the operating current, an immanent risk exists that the performance of the estimator is influenced by the systematic error of the current measurement.

In order to investigate the performance of the estimator in case of inaccurate current measurements, the current signal is distorted with a temperature-dependent systematic error due to both a bias and a gain component according to

$$i_{\mathrm{sens}}\left(i(t),\vartheta(t)\right)=\frac{0.1+10^{-4}\left(\vartheta(t)-20\right)}{0.1}i(t)+3\cdot10^{-4}\left(\frac{|\vartheta(t)-20|}{60}+1\right). \quad (3.56)$$

The battery testing unit used for the experiments in the lab measures the temperature of the shunt resistor to provide highly accurate current signals by correcting the temperature-induced drift of the measurements [46]. This offers the opportunity to feed a realistic temperature course (see e.g. Figure 3.11) to the senor model above in order to simulate low accurate current measurements.

[6] In the concluding chapter, it will explained which shortcomings appear in context with slow mixing systems and particle filtering.

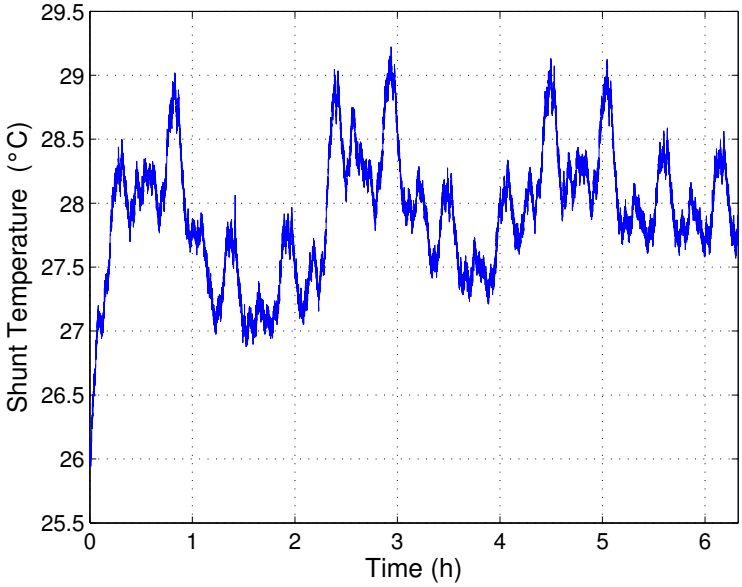

Figure 3.11.: Measured temperature of the shunt resistor during the experimental evaluation of the ARTEMIS-urban driving cycle.

Again, three separate Monte Carlo analyses were carried out to assess the performance of the proposed estimator in case of current measurements distorted by a significant systematic error. The same parameterization as before was used which yielded in the results shown in the figures below.

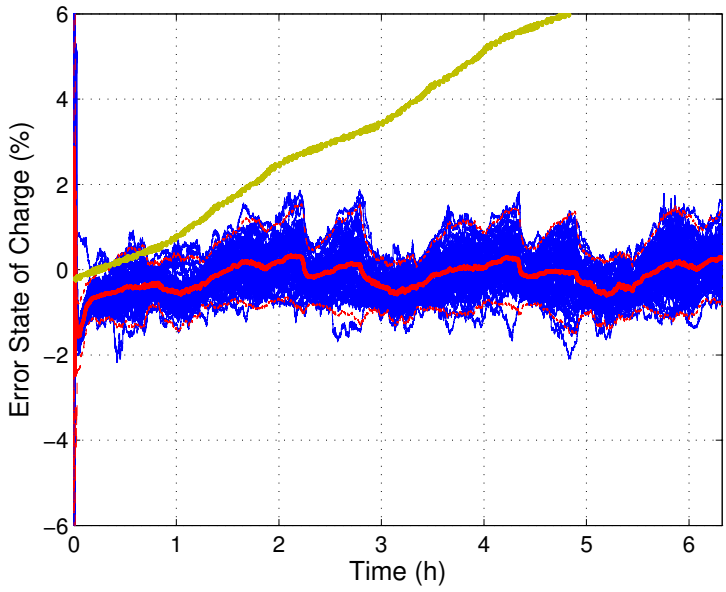

Figure 3.12.: Results of the Monte Carlo analysis estimating the simulated SOC (ARTEMIS-urban driving cycle) in the case of inaccurate current measurements. The blue lines show the individual error courses the red lines depict the average error (solid) and the corresponding 2σ confidence interval (dashed) for 47 converging trails. The yellow curve represents the SOC error obtained by coulomb counting.

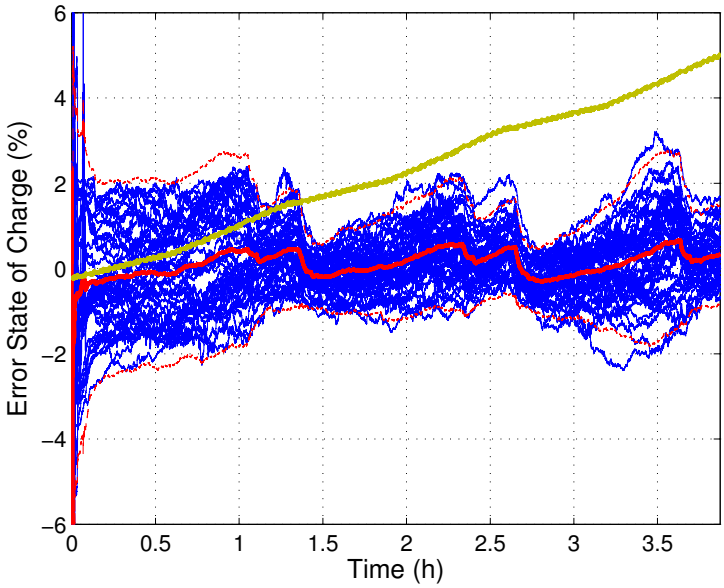

Figure 3.13.: Results of the Monte Carlo analysis estimating the simulated SOC (Braunschweig driving cycle) in the case of inaccurate current measurements. The blue lines show the individual error courses the red lines depict the average error (solid) and the corresponding 2σ confidence interval (dashed) for 43 converging trails. The yellow curve represents the SOC error obtained by coulomb counting.

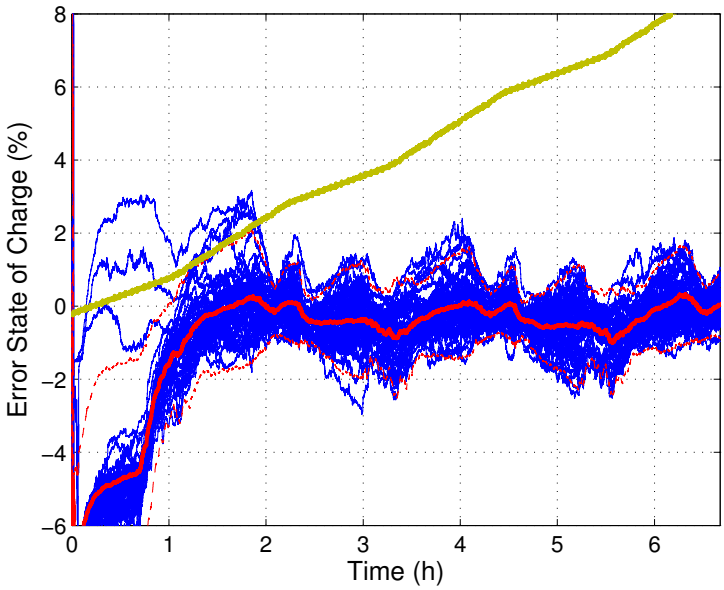

Figure 3.14.: Results of the Monte Carlo analysis estimating the simulated SOC (Manhatten driving cycle) in the case of inaccurate current measurements. The blue lines show the individual error courses the red lines depict the average error (solid) and the corresponding 2σ confidence interval (dashed) for 50 converging trails. The yellow curve represents the SOC error obtained by coulomb counting.

Apparently, the systematic error of the current measurements proves to be of minor relevance with respect to the performance of the estimator since both the average SOC errors as well as the associated 2σ confidence intervals appear to be in the same range, compared to results obtained due to the ideal current measurements. At a first glance, the only difference is that the average SOC error curves tend to oscillate in the case of the distorted current measurements. This behavior can be interpreted as follows: Due to the systematic error (and especially the bias component) of the current measurement, the SOC error steadily increases since the current error is integrated by the state update equation. This fact is exactly the reason for estimating the SOC by means of Bayesian filtering and, thus, to infer the states from the voltage measurements. Due to the in wide ranges flat characteristic of the open circuit voltage, it takes some time until the integral component of the SOC error reaches a certain level, while the associated particles are consequently weighted with negligible weight by evaluating the measurement prediction density $p\left(y_k|\mathbf{x}_{0:k,i}, y_{0:k-1}\right)$. In other words, the estimate of the SOC temporarily drifts due to the distorted current measurements but is corrected if the deviation exceeds a certain level.

In addition to the SOC error courses, the convergence rate of the estimator is also in the same range as before. The Monte Carlo analysis associated with ARTEMIS-urban driving cycle converges slightly better than before (three fails), while the convergence rate of the study utilizing the Braunschweig record is slightly worse (seven fails). In the case of the current profile derived by the Manhatten driving cycle, convergence was achieved for all 50 individual trials. However, it should be mentioned that the number of Monte Carlo trails is too low in order to draw any conclusion concerning the dependency of the current signal's accuracy on the convergence rate of the estimator.

The estimation results of all three states are exemplarily shown in Figure 3.15, 3.16 and 3.17, respectively, while the state and parameter courses of the most suitable ARTEMIS-urban trial is used for visualization.

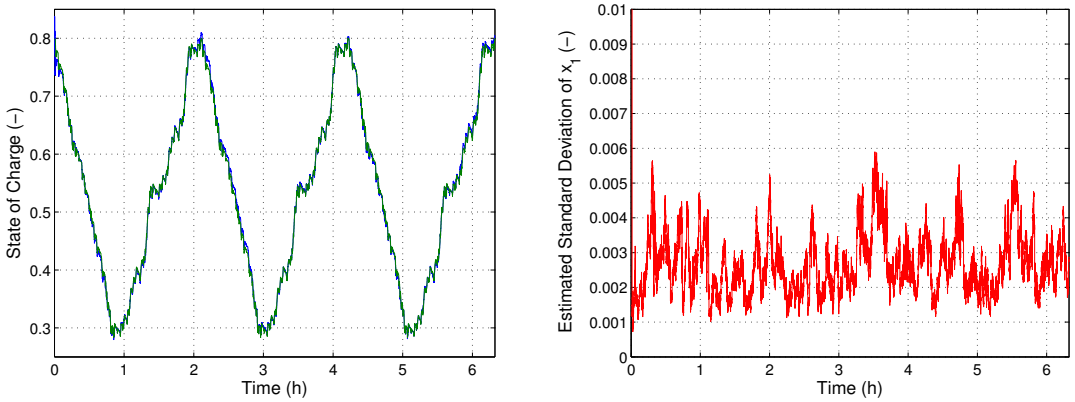

Figure 3.15.: Estimation results of the course of the state $x_{1,k}$ (SOC) of the simulated ARTEMIS-urban record for the case of inaccurate current measurements. Left: estimated (blue) and simulated (green) course of $x_{1,k}$. Right: estimated standard deviation of $x_{1,k}$.

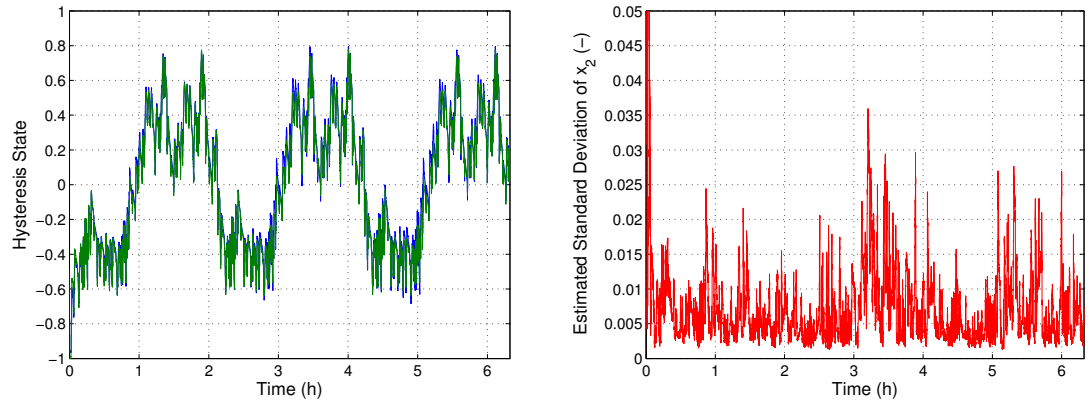

Figure 3.16.: Estimation results of the course of the state $x_{2,k}$ (hysteresis state) of the simulated ARTEMIS-urban record for the case of inaccurate current measurements. Left: estimated (blue) and simulated (green) course of $x_{2,k}$. Right: estimated standard deviation of $x_{2,k}$.

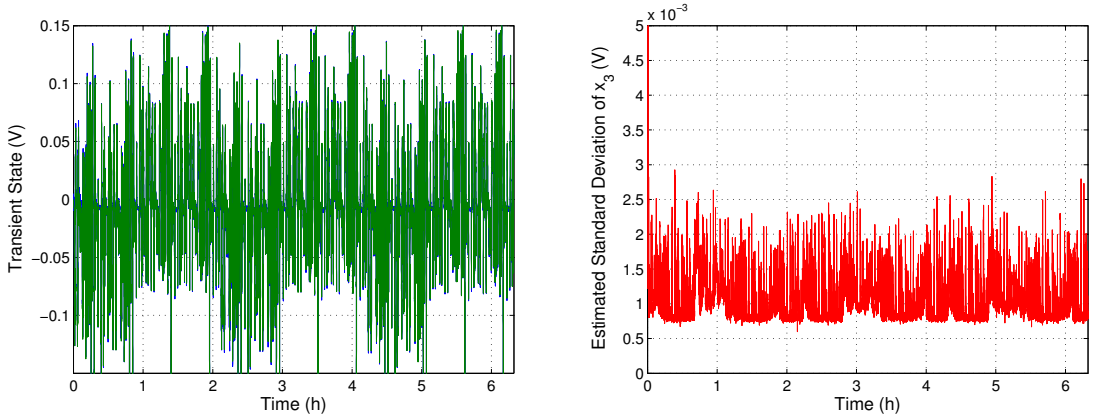

Figure 3.17.: Estimation results of the course of the state $x_{3,k}$ (transient state) of the simulated ARTEMIS-urban record for the case of inaccurate current measurements. Left: estimated (blue) and simulated (green) course of $x_{3,k}$. Right: estimated standard deviation of $x_{3,k}$.

As can be seen from the left figures, the estimates reach an acceptable level of accuracy for each component of the state vector $\mathbf{x}_k$ since the simulated courses (blue lines) nearly coincide with the estimated courses (green lines). The right figures show the corresponding courses of the estimated standard deviations of the state estimates which were derived by using the particle approximation to estimate the second central moment similar to eq. 3.31a.

Since the proposed estimator is based on the concept of joint estimation, the question is how accurate the estimates of the associated model parameters are. As can be seen from the figures below, the obtained parameter courses appear to be less accurate compared to the estimated state trajectories shown above.

This behavior is characteristic for the joint estimation framework and caused by the poor update model (random walk) for the parameter vector $\boldsymbol{\theta}_k$ (see eq. 3.45). Unfortunately, due to the absence of alternatives, the random walk model is (more or less) indispensable.

In the case of the gain parameter for the hysteresis state $\theta_{1,k}$ and the eigenvalue of the transient state $\theta_{2,k}$, the estimates appear to be at least in the range of the simulated courses. Apparently, the gain parameter of the transient state θ_2 proves to be detectable more easily since the estimator succeeded in tracking the simulated course of this parameter quite accurately.

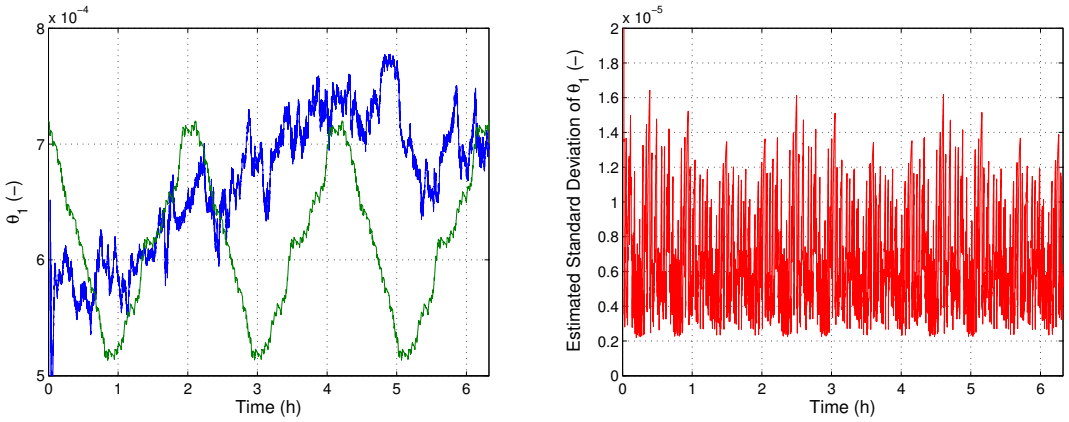

Figure 3.18.: Estimation results of the course of the parameter $\theta_{1,k}$ (gain hysteresis state) of the simulated ARTEMIS-urban record for the case of inaccurate current measurements. Left: estimated (blue) and simulated (green) course of $\theta_{1,k}$. Right: estimated standard deviation of $\theta_{1,k}$.

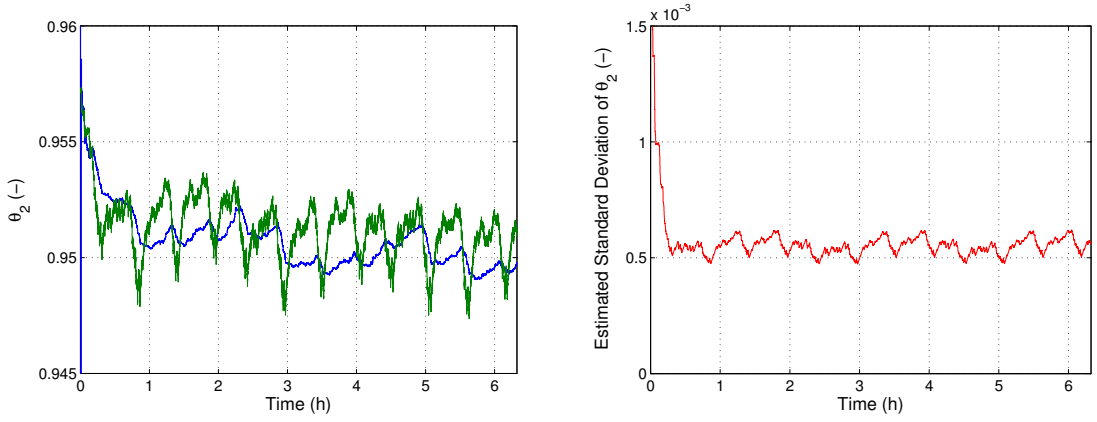

Figure 3.19.: Estimation results of the course of the parameter $\theta_{2,k}$ (eigenvalue transient state) of the simulated ARTEMIS-urban record for the case of inaccurate current measurements. Left: estimated (blue) and simulated (green) course of $\theta_{2,k}$. Right: estimated standard deviation of $\theta_{2,k}$.

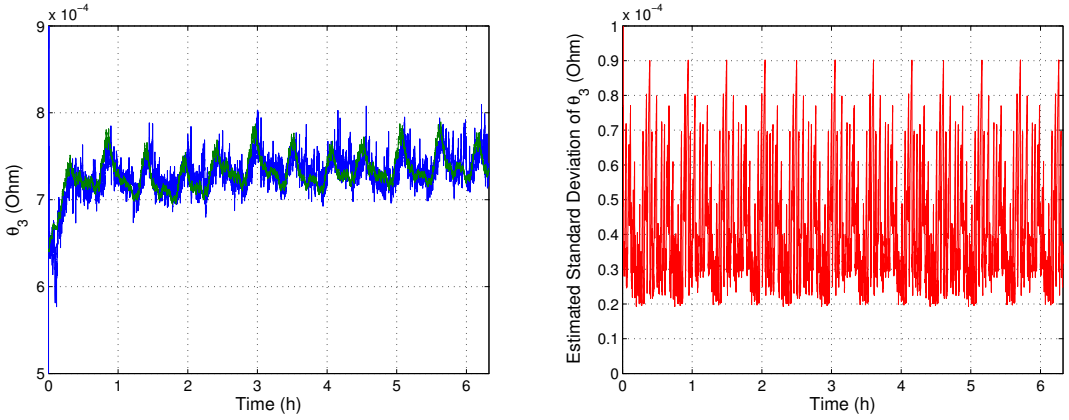

Figure 3.20.: Estimation results of the course of the parameter $\theta_{3,k}$ (gain transient state) of the simulated ARTEMIS-urban record for the case of inaccurate current measurements. Left: estimated (blue) and simulated (green) course of $\theta_{3,k}$. Right: estimated standard deviation of $\theta_{3,k}$.

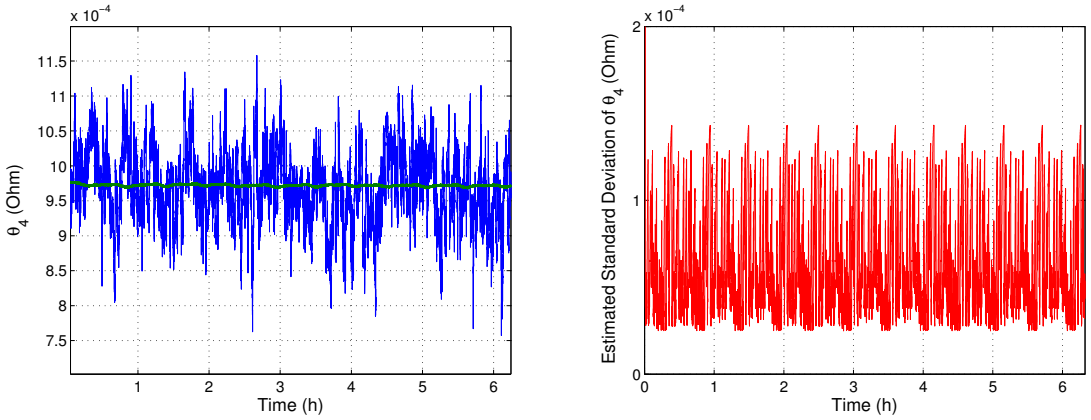

Figure 3.21.: Estimation results of the course of the parameter $\theta_{4,k}$ (feedthrough) of the simulated ARTEMIS-urban record for the case of inaccurate current measurements. Left: estimated (blue) and simulated (green) course of $\theta_{4,k}$. Right: estimated standard deviation of $\theta_{4,k}$.

The estimated course of the feedthrough parameter $\theta_{4,k}$ shows quite a number of variations on the true simulated course. Thus, the simulated course appears to be nearly constant in Figure 3.21, which is due to the fact that the feedthrough parameter is not associated with the internal dynamics and, scaled by the current sample at time step k, enters directly into measurement prediction density $p\left(y_k|\mathbf{x}_{0:k,i}, y_{0:k-1}\right)$. Depending on the current signal, as a consequence, this probability density varies significantly with respect to the dimension associated with the feedthrough parameter. Since this probability density is used for both the update of the importance weights and the measurement update step for the parameter process, the estimate of the parameter vector also fluctuates with respect to this dimension.

In principle, the results demonstrate a good detectability of the SOC in the case of distorted current measurements. The question which may arise is how sensitive the estimator on inaccurate voltage measurements is. With respect to noise, the performance of the estimator should be more or less invariant as long as the voltage measurements provide a certain signal-to-noise ratio and are at least "Gaussian-like" distributed. Remember, that the variance of the voltage measurements was parameterized relatively largely being $R = 10^{-6}$ in order to broaden the measurement prediction density $p\left(y_k|\mathbf{x}_{0:k,i}, y_{0:k-1}\right)$ and, thus, to increase the robustness of the estimator. Unfortunately, deviations of the voltage measurements induced by systematic errors are more critical. In this context, the flat characteristic dependence of the SOC on the open circuit voltage U_{OCV} proves to be problematic since the inverse mapping shifts the measurement prediction density $p\left(y_k|\mathbf{x}_{0:k,i}, y_{0:k-1}\right)$ used, inter alia, for the update of the importance weights far away from the location of the true SOC. As a consequence, the estimate is expected to be biased. This is especially true for the chosen parameterization of the estimator as with respect to the SOC $(x_{1,k})$ and the hysteresis state $(x_{2,k})$, the initial distribution of the particles is only restricted to valid ranges. Hence,the influence of the biased voltage measurements was not investigated.

3.3.2. Estimation Results

Encouraged by the results of the simulation studies, the next logical step is to evaluate the performance of the Rao-Blackwellized estimation framework for real measurements. For this purpose, the current profile derived by the ARTEMIS-urban driving cycle was used for the experimental evaluation of an A123 26650m1B $LiFePO_4$ battery. Consequently, the measured courses of the operating current and the terminal voltage were fed to the estimator.[7]

In contrast to the simulation studies, the less restrictive choice of the initial distribution of the particles does not work anymore. Since the battery was initially fully charged and discharged by a charge level of 0.5 Ah, corresponding to an initial SOC of approximately 80%, the components of the i^{th} initial particle associated with the SOC and hysteresis state were sampled according to

$$x_{1,0,i} \sim \mathcal{U}\left(0.5, 1\right) \tag{3.57a}$$

$$x_{2,0,i} \sim \mathcal{U}\left(-1, -0.5\right), \tag{3.57b}$$

which reflects the prior knowledge that the battery was initially at least half charged and the hysteresis state $x_{2,0}$ is expected to take an negative value due to the major discharge pulse immediately before the experiment. The initial distribution of the remaining component $x_{3,0,i}$ was unchanged $(\mathcal{N}\left(0, 0.01\right))$. Similarly, the previous choice of the prior parameter distribution was altered in order to achieve a converging

[7] Interested parties may wonder why the simulation studies were performed on all three driving cycles introduced in section 3.2, but in case of real measurements, the performance of the estimator is only evaluated by means of the data record obtained by testing the ARTEMIS-urban driving cycle. This circumstance is due to a mishap in conjunction with the empirical determination of the open circuit voltage charge and discharge curves. Since the driving cycles were tested with three different batteries, the open circuit voltage charge and discharge curves are required for all three batteries. Unfortunately, the data records of the batteries associated with the Braunschweig and Manhatten driving cycle were lost accidentally.

configuration. Hence, except for the initial mean value associated with the eigenvalue of the transient state, the mean vector was altered according to

$$\boldsymbol{\theta}_{0|-1,i} = \begin{bmatrix} 10^{-4} & 0.9 & 10^{-3} & 10^{-3} \end{bmatrix}^T . \tag{3.58a}$$

By analogy with the parameterization for the simulation studies, the prior parameter covariance was found by progressively decreasing the variance entries according to

$$\mathbf{P}_{0|-1,i} = \begin{bmatrix} 10^{-8} & 0 & 0 & 0 \\ 0 & 10^{-6} & 0 & 0 \\ 0 & 0 & 10^{-6} & 0 \\ 0 & 0 & 0 & 10^{-6} \end{bmatrix} . \tag{3.58b}$$

Except for the number of particles N and the threshold for resampling N_t, the remaining parameterization stayed unchanged. As for the first, the size of the particle set could be reduced to $N = 500$. This is presumably due to the fact that the modified parameterization provides much more prior information than before. The resampling threshold was set to $N_t = 500$ (bootstapping) since no substantial difference in the performance of the estimator was discovered compared to smaller values leading to a converging configuration.

Performance Evaluation for Unbiased Current Signals

Similar to the simulation studies, the performance of the estimator was evaluated in a first step by means of undistorted current measurements and 50 individual Monte Carlo trials. The outcome of this study is shown in the figure below.

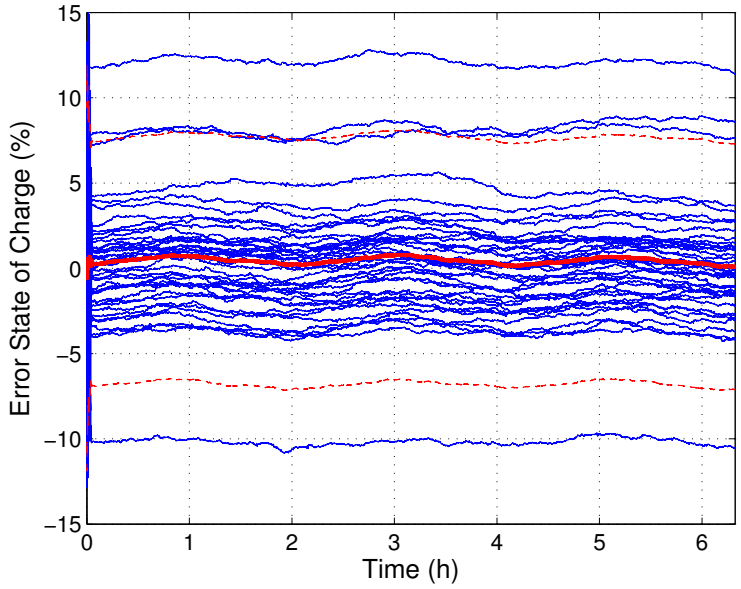

Figure 3.22.: Results of the Monte Carlo analysis to assess the performance of the RBPF estimator by means of the measured ARTEMIS-urban data record. The blue lines show the individual SOC error courses while the red lines depict the average error course (solid) and the estimated 2σ confidence interval (dashed) for 41 converging estimation trials.

The convergence of the estimator was not successful for all trials. In the case of 41 trials, the estimator converged after a few recursions, which is comparable to the convergence rate of the previous studies.

However, the obtained error curves do not fulfill the intended estimator accuracy. Although the average SOC error is in the same range as in the studies before, the estimator achieved significantly biased estimates in the case of 4 trails. At a first glance, this circumstance proves to be crucial since, in contradiction to the case of a diverging estimator, the detection of biased estimates is challenging. A closer look on the obtained results reveals that in most cases the estimator achieves acceptable accuracy with a SOC error being in the range of some percent. Hence, this information can be used in order to detect highly biased estimates and to simply restart the estimator if necessary.

In order to achieve this goal, the proposed estimator is modified and runs in two consecutive operating modes. Since the modification circumvents the problems associated with the significantly biased estimates, the attribute "enhanced" refers to this estimator.

The working principle of the proposed "enhanced" Rao-Blackwellized estimator is as follows: During a defined initial period ($k < N_{\mathrm{med}} N_{\mathrm{win}}$), the estimator is sequentially restarted and the settled SOC estimate is sampled.

In this context the term settled refers to the converged SOC estimate and should not be mistaken for the transient voltage contribution to the battery's terminal voltage. The parameters N_{med} and N_{win} denote the number of settled SOC samples and the duration of the individual settling periods, respectively. During the initial period, a cumulative charge information is calculated by means of coulomb counting. Since, the duration of the initial period is chosen to be sufficiently short, the influence of the systematic error of the current measurements on the cumulative charge information is negligible.

The cumulative charge information serves two purposes. First, the sampled settled SOC estimates can be related to the end of the initial period by correcting the according difference of the SOC. Second, the initial distribution of the uniformly distributed initial particles is corrected by adapting the according limits, which entails denser initial distributions for the initial particles related to the SOC and the hysteresis state. Finally, a median estimate is calculated by means of the N_{med} corrected SOC estimates and a upper and lower threshold can be computed. Algorithm 2 illustrates the initial period of the "enhanced" Rao-Blackwellized estimator.

Afterwards the operating mode is switched to the regular mode. At the first iteration in this operating mode, the current SOC estimate is compared to the previously computed median estimate. If the SOC estimate exceeds one of the two thresholds, the estimator is restarted whereby the distribution of the initial particles is adapted in the same way as mentioned before.

Algorithm 2 Initialization period of the "enhanced" RBPF estimator

Update cumulative charge information: $\Delta\text{SOC}_{k+1} = \Delta\text{SOC}_k + \frac{T_s}{C_n} i_k$
if $\text{mod}(k, N_{\text{win}}) == 0$ **then**
Calculate limits for uniformly distributed inital particles:

$$a_{x_1} = 0.5 + \Delta\text{SOC}_k,\ b_{x_1} = 1 + \Delta\text{SOC}_k$$
$$a_{x_2} = -1 + \Delta\text{SOC}_k,\ b_{x_2} = -0.5 + \Delta\text{SOC}_k$$

Truncate limits to valid ranges
Initialize RBPF estimator
end if
Calculate RBPF recursions
if $\text{mod}(k+1, N_{\text{win}}) == 0$ **then**
Sample SOC estimate: $\tilde{x}_{1,l} = \hat{x}_{1,k}$, $\Delta_l = \Delta\text{SOC}_k$
$l = l + 1$
end if
if $k == N_{\text{med}} N_{\text{win}} - 1$ **then**
Relate sampled SOC estimates to the last sample:
for $i = 1 : l$ **do**
$\tilde{x}_{1,i} = \tilde{x}_{1,i} + (\Delta_l - \Delta_i)$
end for
end if
Calculate median SOC estimate: $\text{SOC}_{\text{med}} = med\left(\{\tilde{x}_{1,1}, \ldots, \tilde{x}_{1,l}\}\right)$
Calculate upper and lower threshold:

$$\text{SOC}_u = \text{SOC}_{\text{med}} - \mu_{e_{\text{med}}} + 0.025$$
$$\text{SOC}_l = \text{SOC}_{\text{med}} - \mu_{e_{\text{med}}} - 0.025$$

Figure 3.23 shows a histogram of the median estimate error with respect to the true SOC at the end of the initial phase obtained by a Monte Carlo analysis of 50 trials investigating the ARTEMIS-urban driving cycle data record. $N_{\text{med}} = 10$ settled SOC samples were used for the median estimate whereby the settling duration was assumed to be less than $N_{\text{win}} = 200$ iterations. Apparently, the median estimator achieves acceptable accuracy with an error being bounded between -1 % and +1.4 %. For the given configuration, the median estimate is biased with a value of $\mu_{e_{\text{med}}} = +0.61$ %, depicted by the red line.

The initial period of one trail is shown in Figure 3.24. The green and blue lines show the true SOC and the SOC estimate, respectively. The settled SOC estimates (red markers) are used in combination with the cumulative charge information to compute the median SOC estimate at the end of the initial period (solid cyan line). The according threshold levels (dashed lines) are found by parameterizing an error band ±2.5 % with respect to the median estimate. As shown in Figure 3.23, the median estimates is biased. Hence, the thresholds are shifted by the empirical found error bias $\mu_{e_{\text{med}}} = +0.61$. Reducing the error band to significantly smaller values than ±2.5 % yields to a poor performance of the algorithm, since the acceptance probability rapidly drops if the error band is too small.

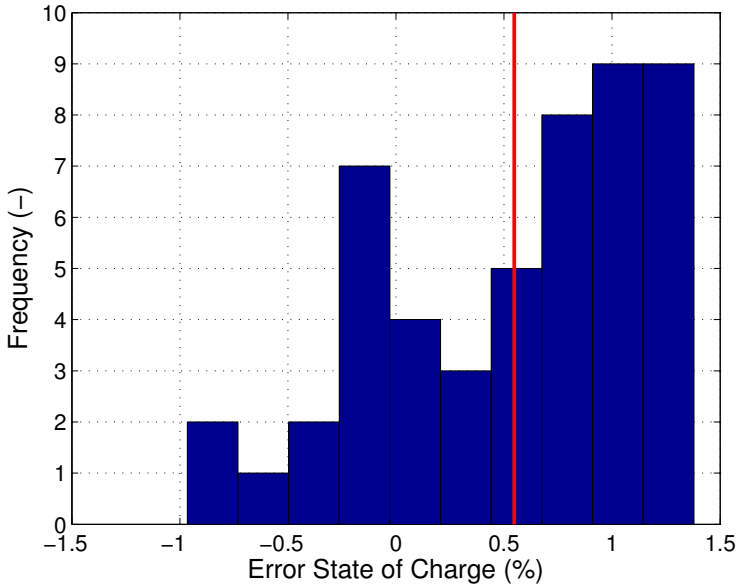

Figure 3.23.: Histogram of the deviation of the median SOC estimate with respect to the true SOC at $k = N_{\text{med}} N_{\text{win}} - 1 = 1999$. The results were obtained by means of a Monte Carlo analysis (50 trials) using the measured ARTEMIS-urban data record. The red line depicts the (sample) mean of the deviations of the median estimates.

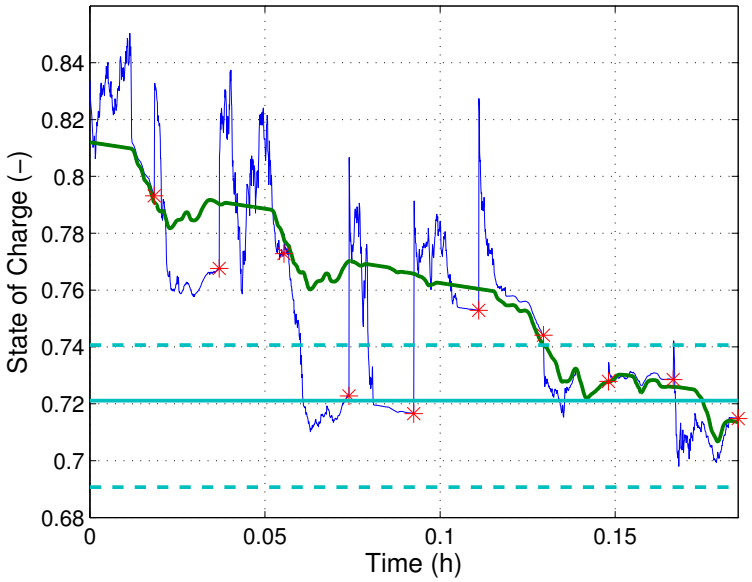

Figure 3.24.: Initial period of the "enhanced" Rao-Blackwellized estimator. The blue line shows the SOC estimate provided by the Rao-Blackwellized estimator started 10 times. The according settled SOC estimates (red markers) were sampled after 200 iterations. The true course of the SOC is shown by the green line, while the solid and dashed cyan lines depict the median estimate and the according threshold levels, respectively.

Figure 3.25 shows the SOC error plot of the mentioned Monte Carlo study. Apparently, the provided measure significantly improves the accuracy of the SOC estimator. As intended, significantly biased estimates can be ruled out. Moreover, the majority of the error is kept between -2 % and 2.5 %. This circumstance is also confirmed by the 2σ confidence interval depicted by the red dashed lines in Figure 3.25. Additionally, the convergence rate improved significantly, since all 50 trials converged. This fact can be explained by the adaptation of the initial distribution during the initial period and the resulting progressively denser distributed initial particles.

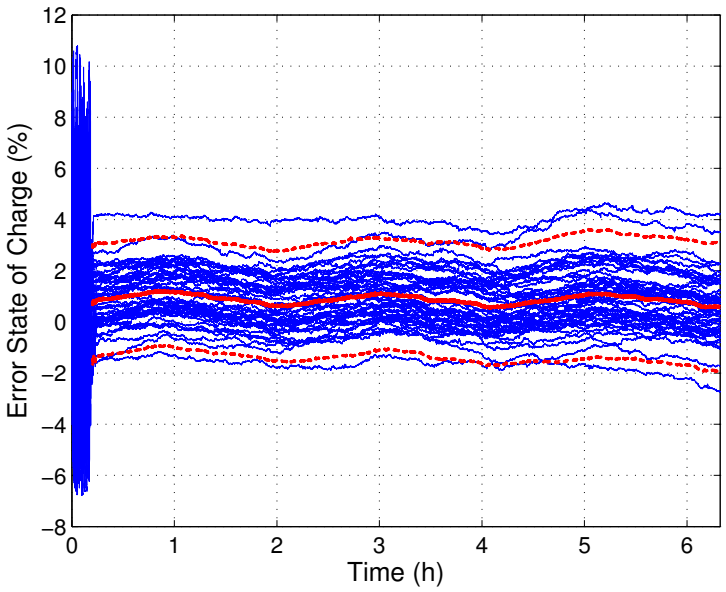

Figure 3.25.: Results of the Monte Carlo analysis to assess the performance of the "enhanced" RBPF estimator by means of the measured ARTEMIS-urban data record. 2000 iterations (666 seconds) were chosen for the initial period. Within this period, the algorithm was restarted 10 times. The blue lines show the individual SOC error courses, while the red lines depict the average error course (solid) and the estimated 2σ confidence interval of the remaining period.

Performance Evaluation for Inaccurate Current Signals

As demonstrated by the SOC error curves shown in Figure 3.25, the proposed "enhanced" Rao-Blackwellized estimation framework provides sufficiently accurate estimates of the battery's SOC. The question is if the proposed estimation framework overcomes also the problems associated with the systematic error of the current measurements. In order to answer this question, similar to the corresponding simulation study, the current measurements were distorted according to eq. 3.56 and the Monte Carlo analysis was repeated with the same parameterization as just before. The outcome of this study is shown in Figure 3.26.

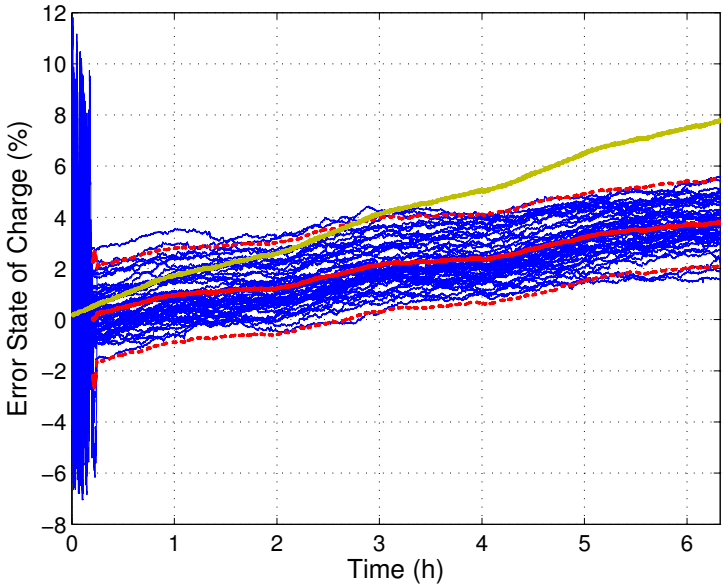

Figure 3.26.: Results of the Monte Carlo analysis to assess the performance of the enhanced RBPF estimator by means of the measured ARTEMIS-urban data record with artificially distorted current measurements. The blue lines show the individual SOC error courses while the red lines depict the average error course (solid) and the estimated 2σ confidence interval (dashed). The yellow curve represents the SOC error obtained by coulomb counting.

Similar to the previous results, the "enhanced" Rao-Blackwellized estimator prevents from significantly biased estimates. Furthermore convergence was achieved for all 50 trials. However, the influence of the systematic error of the current measurements is only partly compensated by the estimator. Compared to the SOC error obtained by coulomb counting, the slopes of the error curves are reduced. Nevertheless, the deviation of the SOC estimate may be significant after several hours. Hence, the proposed estimator fails to circumvent the shortcomings of the inaccurate current measurements. Consequently, the current measurement system has to provide a high accuracy, particularly avoiding integrator offset errors.

Let us take a closer look at the obtained estimates. Similar to the according simulation study, the figures below illustrate the estimated state and parameter trends as well as the corresponding standard deviations of the most suitable estimation trial.

As shown in Figure 3.27, only small deviations of the SOC estimate ($x_{1,k}$) are noticeable at the beginning of the regular estimation period. As mentioned before, the accuracy of the this estimate progressively decreases due to the systematic error of the current measurement. Moreover, the estimate of the according standard deviation is reduced by a factor of 5 and is presumably significantly underestimated.

The estimate of the hysteresis state $x_{2,k}$, (Figure 3.28) rapidly oscillates between the minimum and maximum value. This is presumably due to the fact that the corresponding hysteresis gain parameter $\theta_{1,k}$ (see Figure 3.30) appears to be much larger than expected. Of course, the true amount of charge which is required to move

entirely from one open circuit voltage curve to the other is not known and probably influenced, inter alia, by the SOC, the temperature or the operating current, to name but two. However, the shown course of the parameter $\theta_{1,k}$ corresponds with the given sample time T_s to less than 1% of the battery's nominal capacity C_n. According to the results obtained in section 2, this value is presumably too small.

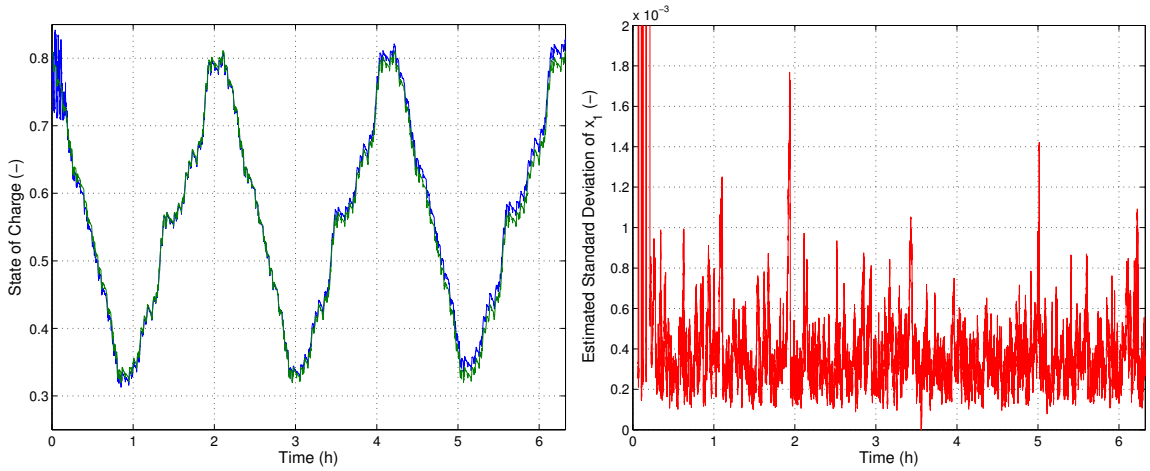

Figure 3.27.: Estimation results of the trajectory of the state $x_{1,k}$ (SOC) for the measured ARTEMIS-urban record with numerically distorted current measurements. Left: estimated (blue) and simulated (green) course of $x_{1,k}$. Right: estimated standard deviation of $x_{1,k}$.

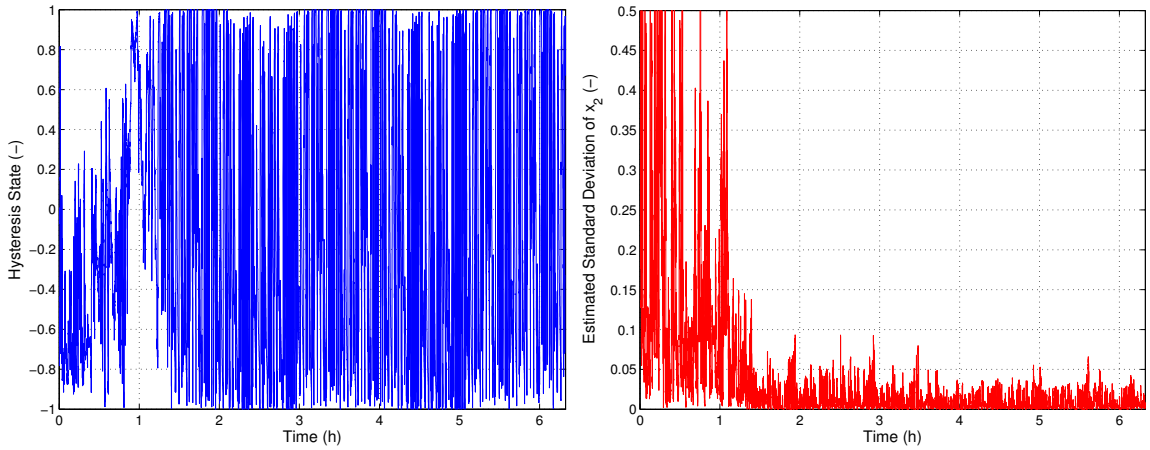

Figure 3.28.: Estimation results of the trajectory of the state $x_{2,k}$ (hysteresis state) for the measured ARTEMIS-urban record with numerically distorted current measurements. Left: estimated course of $x_{2,k}$. Right: estimated standard deviation of $x_{1,k}$.

Also less pleasing is the estimated trajectory of the transient state ($x_{3,k}$) shown in Figure 3.29. Although the estimate of the according eigenvalue $\theta_{2,k}$ appears to be in a realistic range, the estimate of $x_{3,k}$ does not exclusively exhibit the characteristic

transient behavior. By comparing Figure 3.27 and Figure 3.29, the dependence of the SOC on the estimate of the transient state is apparent. Metaphorically speaking, this can be interpreted in a way that the algorithm compensates the inaccurate estimates of the states associated with the open circuit voltage U_{OCV} by adapting the transient state which linearly enters into the expression for the terminal voltage U_{term}.

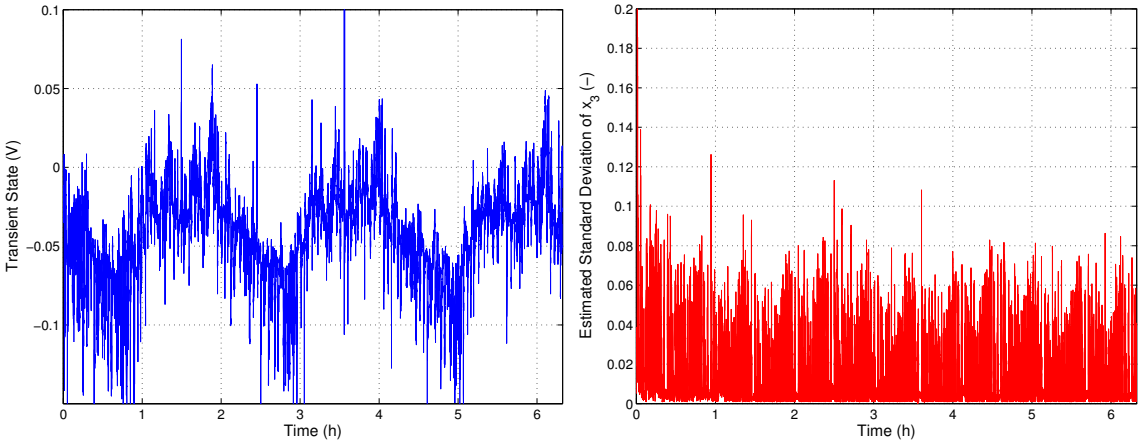

Figure 3.29.: Estimation results of the trajectory of the state $x_{3,k}$ (transient state) for the measured ARTEMIS-urban record with numerically distorted current measurements. Left: estimated course of $x_{3,k}$. Right: estimated standard deviation of $x_{3,k}$.

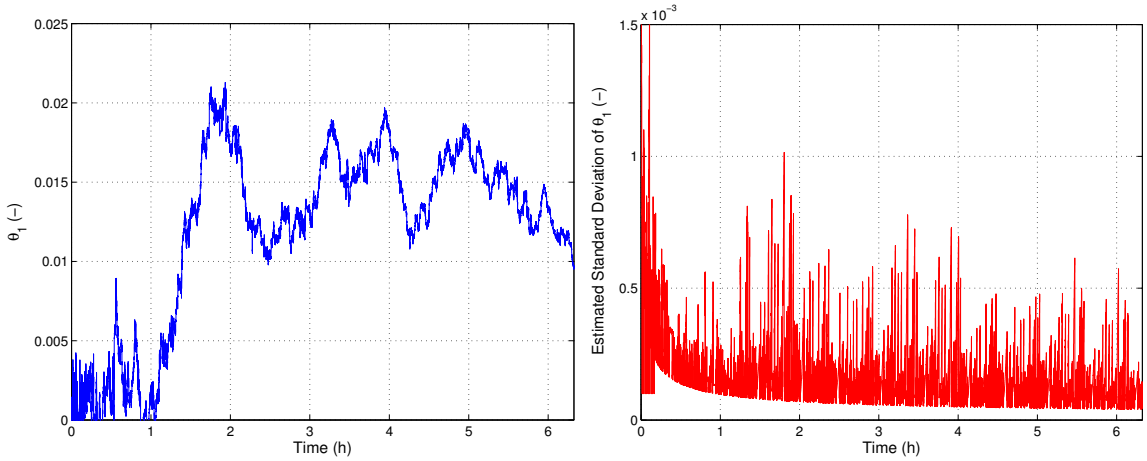

Figure 3.30.: Estimation results of the course of the parameter $\theta_{1,k}$ (hysteresis gain) for the measured ARTEMIS-urban record with numerically distorted current measurements. Left: estimated course of $\theta_{1,k}$. Right: estimated standard deviation of $\theta_{1,k}$.

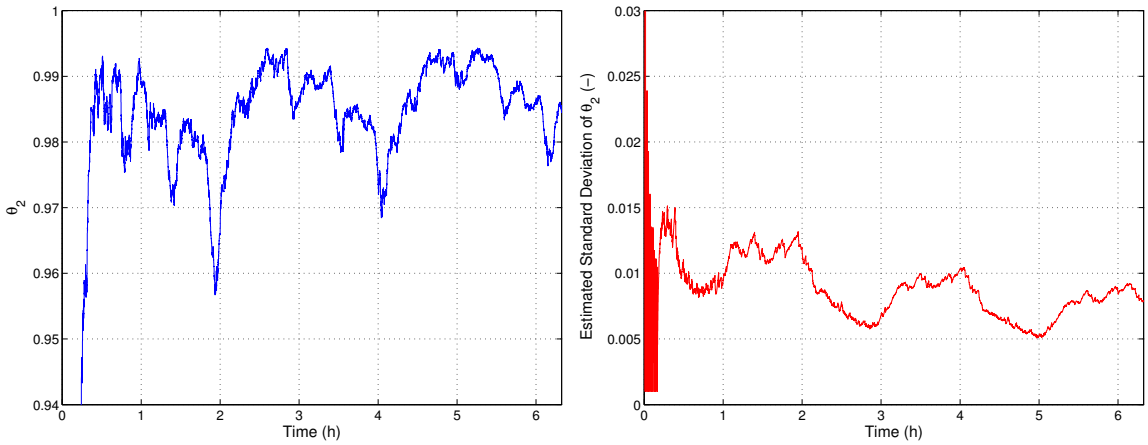

Figure 3.31.: Estimation results of the course of the parameter $\theta_{2,k}$ (eigenvalue transient state) for the measured ARTEMIS-urban record with numerically distorted current measurements. Left: estimated course of $\theta_{2,k}$. Right: estimated standard deviation of $\theta_{2,k}$.

Due to the shortcomings associated with the estimate of the transient trajectory $x_{3,k}$, it is not surprising that the estimated course of the current gain parameter of the transient state $\theta_{3,k}$ is also less convincing. As illustrated in Figure 3.32, the adaptation of this parameter is associated with large temporal variations. Since there is no indication that the kinetics of the charge transport in the battery alters that rapidly, this parameter is presumably estimated inaccurately, which is also indicated by the according estimated standard deviation. Another striking aspect is that the estimate appears in an unphysical range as also negative values are detected. However, negative values of this parameter can be ruled out since otherwise the power dissipation associated with charging/discharging would be negative.

Moreover, the same situation is encountered with respect to the feedthrough parameter $\theta_{4,k}$ (see Figure 3.33). Since, this quantity directly enters scaled by the operating current the expression for the terminal U_{term}, the algorithm presumably compensates deviations of the estimated open circuit voltage by preferably adapting this parameter similar to the considerations with respect to the transient state. However, this behavior is characteristic for biproper systems, which was already mentioned when discussing the results obtained by simulation (see Figure 3.21).

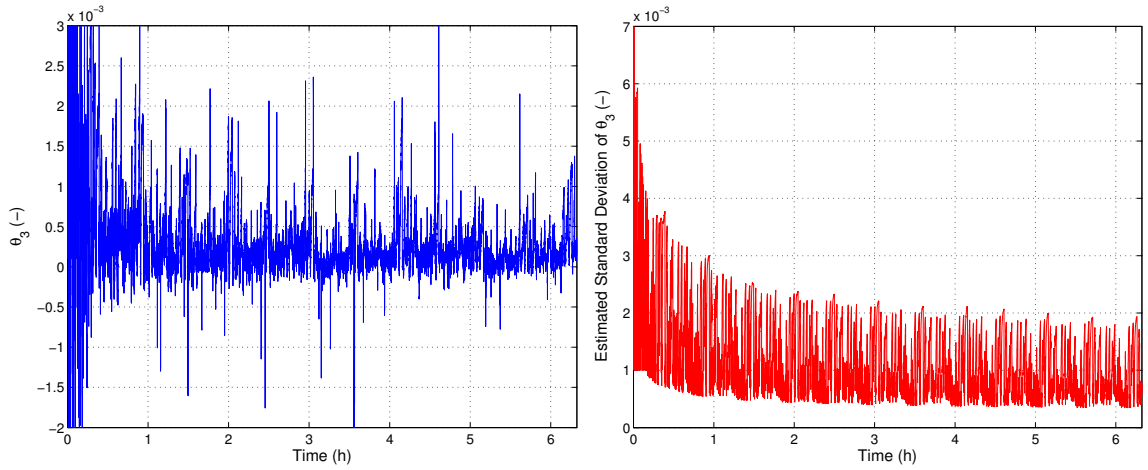

Figure 3.32.: Estimation results of the course of the parameter $\theta_{3,k}$ (gain transient state) for the measured ARTEMIS-urban record with numerically distorted current measurements. Left: estimated course of $\theta_{3,k}$. Right: estimated standard deviation of $\theta_{3,k}$.

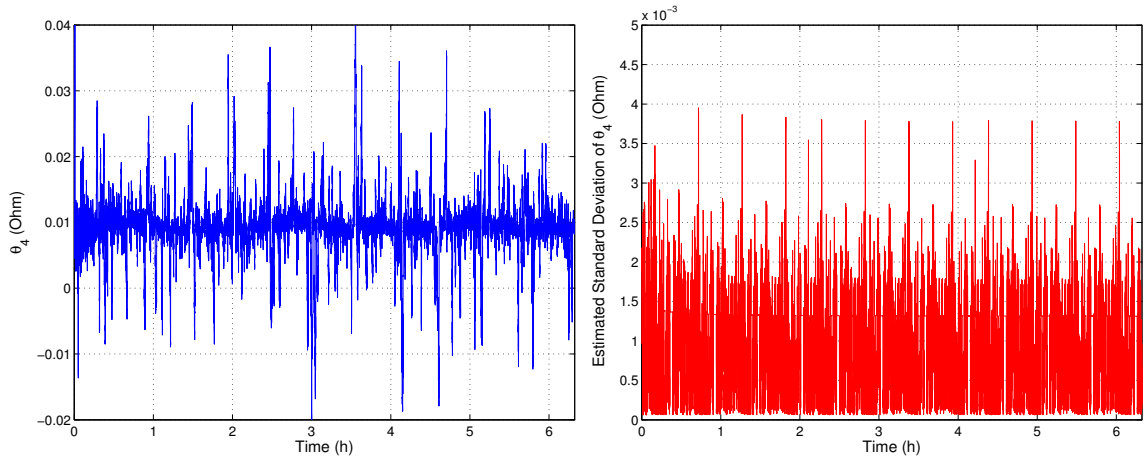

Figure 3.33.: Estimation results of the course of the parameter $\theta_{4,k}$ (feedthrough) for the measured ARTEMIS-urban record with numerically distorted current measurements. Left: estimated course of $\theta_{4,k}$. Right: estimated standard deviation of $\theta_{4,k}$.

Finally, the findings presented in this chapter should be summarized. Based on simulation studies emulating realistic operating conditions it was shown that the Rao-Blackwellized particle is capable to estimate the SOC accurately independent of the charge quantities associated with charging/discharging. The experimental evaluation of the proposed estimator, presented in [40] essentially confirmed the performance of the proposed estimator whereby a detailed statistical analysis of the performance of the estimator was omitted in this review. However, the Monte Carlo analysis performed in this thesis demonstrated that the proposed Rao-Blackwellized particle filter suffers from some shortcomings, since in some cases inaccurate estimates were achieved.

In order to circumvent this problem, a modification of the proposed estimator was suggested. The "enhanced" Rao-Blackwellized estimator circumvents the problem. This circumstance was confirmed by another Monte Carlo analysis.

The Monte Carlo analysis investigating the performance of the "enhanced" Rao-Blackwellized estimator revealed in case of biased current measurements in bad results, since the influence of the systematic error of the current measurement proved to be only partly compensated by the estimator. Hence, high accurate current measurements are required in order to achieve an acceptable level of accuracy. Moreover, the estimates of the hysteresis state and the transient state as well the estimates of the parameters proved to be less convincing. This circumstance is due to the fact that the battery's dynamics, and in particular the transient dynamics, is presumably poorly modeled by the used dynamic model.

However, at this point the discussion of the estimator's performance is postponed to the concluding chapter and the reader's attention is drawn to the upcoming chapter. In contrast to estimating the battery's SOC by Bayesian filtering, a completely different approach is introduced in chapter 4, namely by investigating whether the SOC can be determined by magnetic sensing.

4. Magnetism vs. SOC – A Feasibilty Study

In chapter 4, a Bayesian joint filtering framework was proposed to estimate the SOC of $LiFePO_4$ batteries by means of a sequential Monte Carlo method. Simulation studies carried out in a first step yielded promising results for accurately estimating the SOC independent of the charge quantities associated with charging/discharging. However, the experimental evaluation of the proposed estimation framework resulted in less accurate estimates in case of significantly biased current measurements.

The approach introduced in this chapter is based on a completely different principle. Instead of current and voltage measurements the magnetic properties of the positive electrode are utilized to constitute a relationship with the battery's SOC. This approach is mainly motivated by the role of the Fe atom in the $LiFePO_4$ particle. The Fe-stoichiometry and its state of oxidation is proportional to the number of lithium ions removed/inserted in the positive electrode's active material.

In the periodic table, iron belongs to the group of transition metals. Characteristic of these elements is that their electron configuration includes partially filled d orbitals. As a consequence, an alteration of the electron configuration by means of oxidation/reduction entails a significant modification of the element's intrinsic magnetic moment. Since the positive electrode of the $LiFePO_4$ battery is (except for the current collector foil) a nanoporous compound of carbon-coated $LiFePO_4$, binder and filler particles, the magnetic susceptibility of the battery's positive electrode is directly influenced by the battery's SOC. Note that this relationship is not solely a property of $LiFePO_4$ batteries but of all battery chemistries using transition metals for the positive electrode (e.g. $LiCoO_2$ or $LiMn_4O_2$). Chernova et al. [83] pointed out the connection between magnetism and the electronic and atomic structures of solids used in modern batteries. They suggest that the SOC is determinable by magnetic sensing which circumvents the problems associated with biased current measurements and the $LiFePO_4$ battery's characteristic open circuit voltage.

This chapter mainly describes a feasibility study to prove whether the SOC can be determined by induction sensors in case of a homogeneous magnetized battery. Thereby, the content of this chapter is organized as follows: First, a short introduction to magnetism in condensed matter is provided. Afterwards, the results of two SQUID studies are presented, whereby the magnetic susceptibility is investigated by means of both $LiFePO_4$ powder samples and samples examined from differently charged $LiFePO_4$ batteries. Finally, the required magnetic sensitivity of an induction sensor is determined based on the example of a commercially widespread battery package.

4.1. A Brief Introduction to Magnetism of Condensed Matter

As mentioned before, in order to expose the motivation of magnetic-based SOC sensing, a brief introduction to magnetism in condensed matter is provided first. Clearly, the explanations herein cannot compete with a comprehensive description of magnetism of condensed matter and are restricted to the special case of paramagnetic ions in octahedral environments. Since magnetism of condensed matter relies on quantum mechanical phenomena, the corresponding operators are used without reference to the underlying theory. This circumstance applies especially for the electron spin and all operators associated with this quantity. For an in-depth treatment of magnetism in condensed matter interested parties may refer e.g. to [84–86]. The latter was used as reference textbook for the following explanations.

4.1.1. Magnetic Moments

As mentioned above, magnetism in condensed matter is mainly derived from quantum mechanical principles. Nevertheless, let us start by introducing the fundamental quantity, the magnetic moment $\boldsymbol{\mu}$, by applying the laws of classic physics in order to gain a first insight into magnetic moments. In classic electromagnetism, the magnetic moment induced by a current I in a loop of finite size is given by

$$\boldsymbol{\mu} = I \oint_S \mathbf{dS}. \tag{4.1}$$

Since current occurs by the motion of charged particles which possess mass, the magnetic moment is associated with the angular momentum $\mathbf{L}$ of these particles according to $\boldsymbol{\mu} = \gamma \mathbf{L}$, with γ being a known constant and in the literature often referred to as the gyromagnetic ratio. In a magnetic $\mathbf{B}$-field, a torque $\mathbf{T} = \boldsymbol{\mu} \times \mathbf{B}$ is exerted and the energy of the magnetic moment is given by $E = -\boldsymbol{\mu} \cdot \mathbf{B}$. If no angular momentum is present, the magnetic field aligns the magnetic moment towards its direction turning the energy of the magnetic moment into a minimum value. However, this is not the case and since torque is equal to the temporal alteration of the angular momentum, the relationship between the magnetic moment $\boldsymbol{\mu}$ and the magnetic $\mathbf{B}$-field is given by

$$\dot{\boldsymbol{\mu}} = \gamma \boldsymbol{\mu} \times \mathbf{B}. \tag{4.2}$$

By solving this system of ordinary differential equations for the case of a magnetic $\mathbf{B}$-field being aligned with the z-axis ($\mathbf{B} = B\mathbf{e}_z$), the components of the magnetic moment $\boldsymbol{\mu}$ are given by $\mu_x(t) = |\boldsymbol{\mu}| \sin(\theta) \cos(\omega t)$, $\mu_y(t) = |\boldsymbol{\mu}| \sin(\theta) \sin(\omega t)$ and $\mu_z(t) = |\boldsymbol{\mu}| \cos(\theta)$, respectively. Obviously, the magnetic moment $\boldsymbol{\mu}$ precesses around the magnetic $\mathbf{B}$-field with precession angle θ and precession frequency $\omega = \gamma B$. The latter is often called Larmor precession frequency in the literature.

The question is now how these relationships are incorporated in the magnetism of matter. One may think of the simplest case in which one electron with charge $-e$, mass m_e and velocity $\mathbf{v}$ performs a circular orbit around a hydrogen nucleus. Consequently, this corresponds to a current $I = -e|\mathbf{v}|/2\pi$. Moreover, if the electron is in ground state, the magnitude of its angular momentum must be equal to the

reduced Planck constant $\hbar$, while the magnitude of the magnetic moment of the precessing electron is given by

$$\mu = -\frac{e\hbar}{2m_e} \equiv -\mu_{\mathrm{B}} = -9\,274 \cdot 10^{-24}\ \mathrm{Am}^2. \tag{4.3}$$

It is not surprising that this result is utilized to define a measure of a quantized magnetic moment and that the Bohr magneton μ_{B} was established as convenient unit for expressing electron magnetic dipole moments.

4.1.2. Isolated Magnetic Moments

As already mentioned several times, magnetism in matter is mainly derived by quantum mechanical principles. As a consequence, classic physics is insufficient to provide an accurate mathematical formulation of the phenomena associated with magnetism. This is due to the fact that additionally to the orbital angular momentum, electrons possess an intrinsic momentum called spin. Both moments depend on the state occupied by the electrons and are hence quantized quantities with quantum numbers l, m_l, s and m_s, and m_l and m_s are defined by the quantum numbers l and s, respectively. Consequently, the possible values of these quantities are given by the sets $m_l = \{-l, -l+1, ..., l-1, l\}$ and $m_s = \{-\frac{1}{2}, \frac{1}{2}\}$[1].

By means of the quantum numbers l and m_l, the magnitude of the orbital momentum's contribution is $\sqrt{l\,(l+1)}\mu_{\mathrm{B}}$. The according component along a fixed axis (e.g. z-axis similar to the assumption before) is given by $-m_l\mu_{\mathrm{B}}$. Similarly, the quantum numbers s and m_s are used to constitute a relationship with the spin's contribution to the magnetic moment. The according magnitude equals $\sqrt{s\,(s+1)}g\mu_{\mathrm{B}}$ and the component along the fixed axis is $-m_s g\mu_{\mathrm{B}}$, while $g \approx 2$ is a constant and often referred to as g-factor for the spin-momentum.

Next, the magnetic properties of atoms shall be examined, whereby the interactions between different atoms and their environments are ignored. Hence, it is assumed that the atoms appear to be isolated. In addition, effects like the spin-orbit interaction are not taken into account. The Hamiltonian[2] provides an informative insight for the interaction of the magnetic moment of an atom with a magnetic **B**-field and is given by eq. 4.4 where N_e is the number of electrons, **S** denotes the spin operator, $\mathbf{p}_i$ is the i^{th} momentum without the presence of the magnetic field and V_i is a potential energy function associated with the i^{th} electron. **A** denotes the magnetic vector potential and the term $\mathbf{p}_i + e\mathbf{A}(\mathbf{r}_i)$ defines the canonical momentum of the i^{th} electron.

$$\hat{\mathcal{H}} = \left(\sum_{i=1}^{N_e} \frac{||\mathbf{p}_i + e\mathbf{A}(\mathbf{r}_i)||_2^2}{2m_e} + V_i \right) + g\mu_{\mathrm{B}}\mathbf{S} \cdot \mathbf{B} \tag{4.4}$$

[1] For the sake of completeness, the possible values for the magnetic spin quantum number m_s are $s, (s-1), ..., -s$. Since $s = \frac{1}{2}$ for electrons, this set is reduced to two possible values.

[2] The Hamiltonian $\hat{\mathcal{H}}$ defines a sum of operators corresponding to the kinetic and potential energy of a system. In quantum-mechanics the state of a system is described by a wave function ψ, which can be evaluated by solving Schrödinger's equation. The solution of this partial differential equation is mainly determined by the corresponding Hamiltonian and boundary conditions.

By using the gauge $\mathbf{A}(\mathbf{r}) = \frac{1}{2}(\mathbf{B} \times \mathbf{r})$, the definition for the total angular momentum $\mathbf{L} = \frac{1}{\hbar}\sum_{i=1}^{N_e} \mathbf{r}_i \times \mathbf{p}_i$ and the rules for permuting a scalar triple product according to $\mathbf{a} \cdot (\mathbf{b} \times \mathbf{c}) = \mathbf{b} \cdot (\mathbf{c} \times \mathbf{a})$, the Hamiltonian can be split up into three terms according to

$$\hat{\mathcal{H}} = \left(\sum_{i=1}^{N_e} \frac{||\mathbf{p}_i||_2^2}{2m_e} + V_i \right) + \underbrace{\mu_\mathrm{B}(\mathbf{L} + g\mathbf{S}) \cdot \mathbf{B}}_{\text{paramagnetic term}} + \underbrace{\frac{e^2}{8m_e} \sum_{i=1}^{N_e} ||\mathbf{B} \times \mathbf{r}_i||_2^2}_{\text{diamagnetic term}}. \tag{4.5}$$

The first part on the right-hand side of eq. 4.5 describes the bare Hamiltonian without the presence of a magnetic field, the second term defines the paramagnetic contribution, and the third term arises from the diamagnetic moment of the system. In the case of a linear and isotropic material, the magnetization[3] is equal to $\mathbf{M} = \chi\mathbf{H}$ where χ is a dimensionless scalar quantity called the magnetic susceptibility. If the paramagnetic term dominates, the magnetic susceptibility is positive and the matter is said to show paramagnetic behavior. In this case, the temperature has a significant influence on the magnetic susceptibility. Although $\mu_\mathrm{B}(\mathbf{L} + g\mathbf{S}) \cdot \mathbf{B}$ often exceeds the field-free Hamiltonian, it sometimes vanishes. This is the case if the atom does not posses unfilled shells. Hence, the remaining contribution to the Hamiltonian is the diamagnetic term. Without further treatment, the magnetization induced by diamagnetism displays a negative value and is only marginally influenced by the temperature. Since the approach introduced in this chapter deals with a paramagnetic material, only this case is considered.

4.1.3. Paramagnetism

So far, it has been assumed that the atoms possess zero magnetic moment unless a magnetic field is applied. However, this is not the case in general, and atoms with unpaired electrons show a magnetic moment even in the absence of a magnetic field. In the case of paramagnetic material, these moments point into random directions since neighboring atoms interact only very little with each other. From this point of view, the influence of the temperature on the magnetic susceptibility is obvious. The application of a magnetic field lines up the spins, while an increase of temperature ϑ will randomize them. Consequently, the magnetization of paramagnetic material is approximately proportional to the ratio B/ϑ (ϑ in Kelvin), which can be easily demonstrated by applying the principles of statistical mechanics[4]. For this purpose, the operator for the total angular momentum $\mathbf{J} = \mathbf{L} + \mathbf{S}$ is introduced. Since $\mathbf{L}$ and $\mathbf{S}$ are defined by the quantum numbers l and s, respectively, the operator $\mathbf{J}$ and the component of the magnetic moment along a fixed axis are similarly determined by the quantum numbers J and m_J. With the definitions mentioned above, the influence of the temperature ϑ on the magnetic susceptibility can now be derived

[3] Since matter consists of a large number of atoms associated with magnetic moments, the magnetization $\mathbf{M}$ was introduced to provide a macroscopic measure and is defined as the magnetic moment per unit volume.

[4] In the case of a paramagnetic material, the magnetization is aligned to the magnetic field. For the explanations herein, it suffices to consider only the magnitudes B, H and M of the field vectors $\mathbf{B}$, $\mathbf{H}$ and $\mathbf{M}$.

by using the partition function

$$Z = \sum_{m_J=-J}^{J} e^{\frac{m_J g_J \mu_B B}{k_B \vartheta}} \tag{4.6}$$

where J is the angular atomic momentum, k_B denotes the Boltzmann constant and g_J is the Landé g-factor defined as

$$g_J = \frac{3}{2} + \frac{S(S+1) - L(L+1)}{2J(J+1)}. \tag{4.7}$$

The thermal average of the component of the angular momentum along the magnetic field is given by

$$\mathrm{E}\{m_J\} = \frac{\sum_{m_J=-J}^{J} m_J e^{\frac{m_J g_J \mu_B B}{k_B \vartheta}}}{\sum_{m_J=-J}^{J} e^{\frac{m_J g_J \mu_B B}{k_B \vartheta}}} \tag{4.8}$$

and equals to $JB_J\left(\frac{g_J \mu_B B}{k_B \vartheta}\right)$ where B_J is the Brillouin function.[5] Let N be the number of atoms per unit volume, then the magnitude of the magnetization is given by $M = N g_J \mu_B \mathrm{E}\{m_J\}$. As for the most practical cases, the temperature is not very low and the magnetic field is not extremely large. If these conditions are met, the Brillouin function can be expressed by a Taylor series. Furthermore, if the assumption $g_J \mu_B B \ll k_B \vartheta$ is true, then the magnetic susceptibility can be approximated by

$$\chi \approx \frac{N \mu_0 \mu_{\mathrm{eff}}^2}{3 k_B \vartheta} \tag{4.9}$$

where μ_{eff} denotes the effective magnetic moment given by

$$\mu_{\mathrm{eff}} = g_J \mu_B \sqrt{J(J+1)}. \tag{4.10}$$

4.1.4. Environments

So far, the interaction of isolated atoms with their local environments has been neglected. However, some magnetic ions in certain crystal environments significantly interact with their environment. Consequently, by investigating the magnetic properties of such ions, the respective environment must be taken into account. In the following an iron ion in an octahedral environment is investigated.

The electronic configuration of the iron atom is $[\mathrm{Ar}]3\mathrm{d}^6 4\mathrm{s}^2$. This notation denotes that the state of a completely filled shell corresponds to the electronic configuration of argon and two valence shells are present additionally. The 3d valence shell is filled with six electrons and the 4s valence shell contains two electrons. In the ionic state, iron can be found either as Fe^{2+} or Fe^{3+}. In both cases, the 4s shell is empty. Depending on the ionic state, the 3d shell consists of six (Fe^{2+}) or five electrons (Fe^{3+}), respectively. Since iron belongs to the class of 3d transition metals[6], the alteration of the electron configuration of the 3d shell in dependence of the oxidation

[5] $B_J(y) = \frac{2J+1}{2J} \coth\left(\frac{2J+1}{2J} y\right) - \frac{1}{2J} \coth\left(\frac{y}{2J}\right)$

[6] Transition metal compounds are paramagnetic if one ore more electrons are unpaired.

state is accompanied by a change of the effective magnetic moment μ_{eff}. By solving Schrödinger's equation for the 3d shell electrons, one obtains five orbitals defining the electron probability density in space. The orientation of these orbitals plays a key role for the interaction with the environment and is therefore of significant relevance for cooperative magnetism.

Basically, two theories are common to treat the problem of ions in a crystal environment. In crystal field theory, neighboring orbitals are modeled as negative point charges. As an alternative, ligand field theory improves crystal field theory and is essentially an extension of molecular orbital theory with respect to d orbitals of the central ion overlapping with the orbitals of the surrounding ions. For the sake of simplicity, the explanations herein are only based on crystal field theory and are solely used to provide a short overview of the interaction between the local environment and the central ion. For this purpose, the situation of 3d orbitals in octahedral crystal field is demonstrated in Figure 4.1. The three orbitals d_{xy}, d_{xz} and d_{yz} are lowered in energy associated with the threefold t_{2g} levels but the $d_{x^2-y^2}$ and the d_{z^2} orbitals are raised in energy denoted by the twofold e_g levels. This circumstance is due to the fact that the t_{2g} orbitals point between the coordinating x, y and z axis, while the e_g orbitals are aligned along them. Therefore, the electrostatic repulsion is less operative in the case of the t_{2g} orbitals than in case of the e_g orbitals resulting in the splitting of the corresponding energy levels.

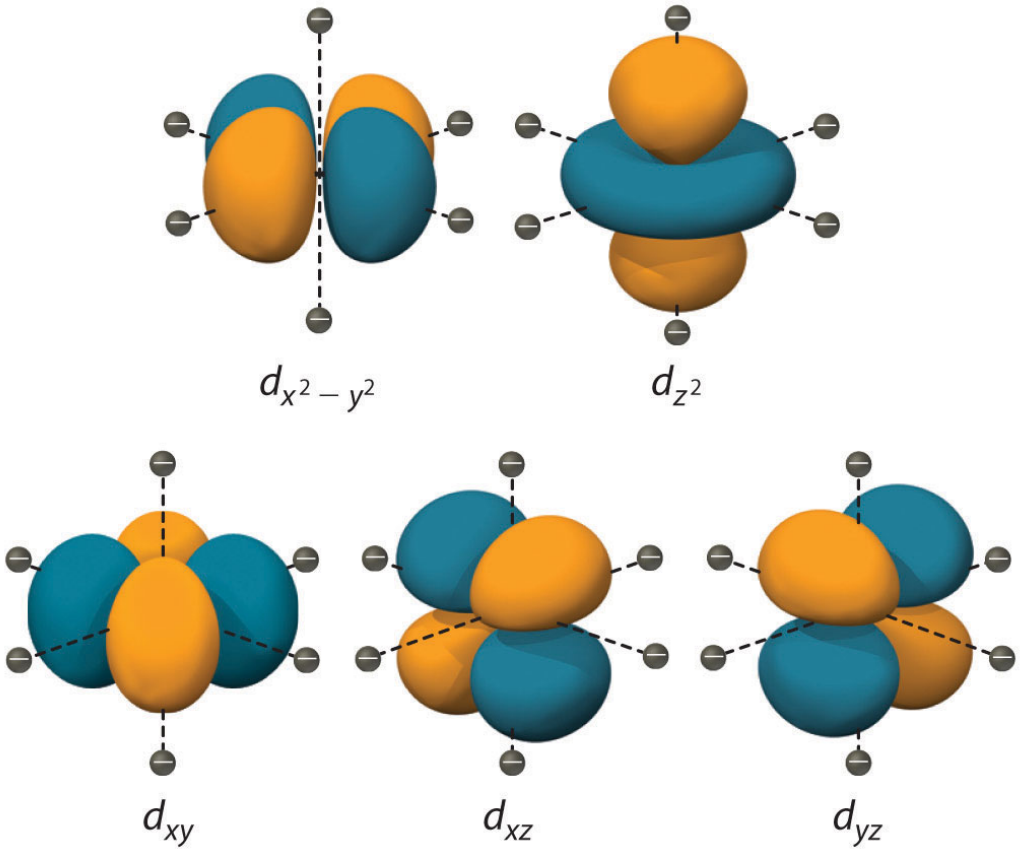

Figure 4.1.: Angular distribution of d-orbitals in an octahedral crystal field. [87]

The question is the occupation of the 3d by the valence electrons. In order to minimize the electrostatic repulsion, the orbitals associated with the t_{2g} levels are preferably filled first (low-spin). This is only the case if a strong crystal field is present since the same orbital is occupied by two electrons at the cost of Coulomb energy denoted as spin pairing energy. If the crystal field is weak, it is energetically more favorable to fill all orbitals first before pairing the electrons with anti-parallel spins leading to high-spin configuration. As for the case of Fe^{2+} and Fe^{3+} ions, both situations are illustrated in Figure 4.2 and Figure 4.3, respectively.

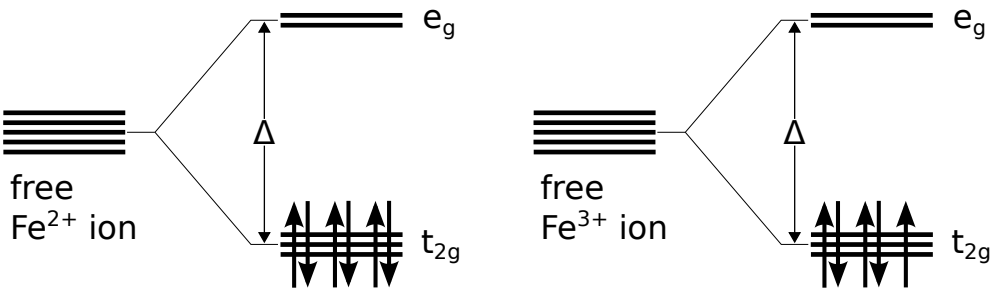

(a) low-spin Fe^{2+}, $S = 0$ (b) low-spin Fe^{3+}, $S = \frac{1}{2}$

Figure 4.2.: Electronic configuration of an Fe^{2+} (a) and Fe^{3+} (b) ion for the low-spin (strong crystal field) case in an octahedral environment.

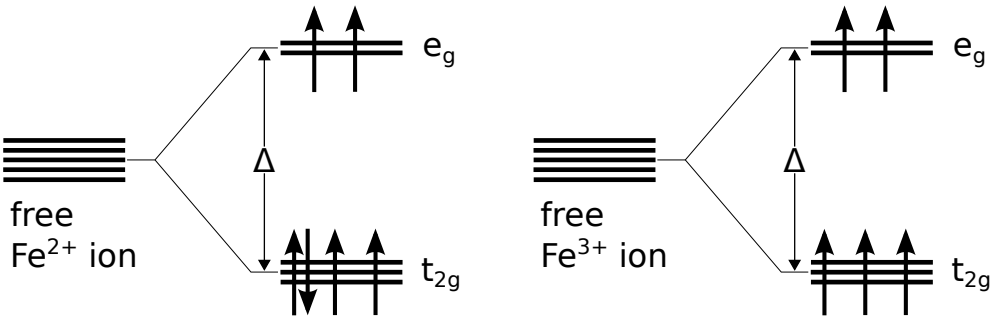

(a) high-spin Fe^{2+}, $S = 2$ (b) high-spin Fe^{3+}, $S = \frac{5}{2}$

Figure 4.3.: Electronic configuration of an Fe^{2+} (a) and Fe^{3+} (b) ion for the high-spin (weak crystal field) case in an octahedral environment.

In case of 3d transition metals, one often encounters the situation that solely the spin configuration determines the magnetic properties of the central ion. This is due to the fact that the ground state of such systems is chosen in a way that orbital magnetism is quenched ($L = 0$). Consequently, the expression for the effective magnetic moment reduces to $\mu_{\text{eff}} = 2\mu_{\text{B}}\sqrt{S(S+1)}$.

The theory discussed here allows an rough estimate of the effective magnetic moment and, thus, the magnetic susceptibility for the case of $LiFePO_4$ particles in the battery's positive electrode. The iron ions change the state of oxidation from Fe^{2+} to Fe^{3+} dependent on lithium insertion/depletion and vice versa. In the crystal

environment of $LiFePO_4$, the iron ions are located in the center of an octahedron, composed of PO_4 molecules acting as ligands at the corners via their magnetic response. Consequently, the spin configuration of the Fe^{2+} and Fe^{3+} ions can be determined. In the case of a low-spin configuration, the spin momentum and, thus, the paramagnetic contribution to the magnetic susceptibility vanishes. Based on previous measurements, this situation can be ruled out [83, 88]. Hence, it is most likely that the ground state for both the Fe^{2+} and Fe^{3+} ion is the high-spin configuration. Consequently, the total spin is assumed to change from $S = 2$ to $S = \frac{5}{2}$ if the lithium ion is removed. Since the orbital momentum is assumed to be quenched, the spin-only formula for the effective moment can be utilized. Thus, the magnetic susceptibility of the cathode's active material is expected to increase up to approximately 45% from a totally discharged to a totally charged battery.

4.2. Experimental Evaluation

In the previous section, the relationship between the state of oxidation and the effective magnetic moment of an iron ion centered in an octahedral PO_4 environment was carried out, whereby the high-spin configuration was assumed as ground state for both the Fe^{2+} and the Fe^{3+} ion. The question is now how much agreement is reached with the lithium insertion/depletion-induced alteration of the magnetic susceptibility in the positive electrode's active material of real $LiFePO_4$ batteries. Note that the presented theory relies on some constraints which are presumably not met in practice. The local environment is assumed to form a symmetric and undistorted octahedron, the orbital momentum is expected to be totally quenched and the crystal field energy Δ is supposed to be not too large to provide the high-spin electronic configuration of the iron ion, to address just a few.

However, the actual composition of the $LiFePO_4$ battery's positive electrode suggests that at least some of the mentioned constraints are violated. This circumstance is due to the fact that the positive electrode's active material consists of carbon coated nanoporous $LiFePO_4$ particles and is therefore not directly comparable to the case of mono-crystal $LiFePO_4$. Additionally, the influence of binder and filler additives in the cathode may not be negligible. A further source of uncertainty is the intercalation process in the active material since insertion/depletion of lithium ions causes deformations in the local environment [89,90]. Hence, the orbital contribution to the magnetic moment might not be fully quenched.

The concomitant change of the magnetic moment of the transition ion spins in the positive electrode's active material has not yet been fully understood to draw essential conclusions from the available reviews of this subject for a practical detection of the SOC by magnetic principles [83, 91, 92]. Consequently, an experimental evaluation of the relationship between the magnetic susceptibility and the level of lithiation of the battery's positive electrode is indispensable to prove the usability of the proposed physical effect for SOC sensing. In this context, two studies with different sample configurations were carried out. In both studies, the magnetic properties of the battery's positive electrode were examined by means a SQUID-based measurement system. The results of the experiments are reported in [42] and [43], respectively.

4.2.1. Experimental Setup

In a first trial, an arrangement of an $LiFePO_4$ battery (pouch package) and an attached air coil was used to investigate whether the battery's SOC can be derived from electromagnetic field quantities. In this early stage and inspired by a white paper of Cadex Electronics Inc. [93], the negative electrode's electrical conductivity was taken into consideration to constitute, inter alia, a relationship with the SOC. Hence, charge and discharge experiments were carried out and the air coil was fed by a sine-wave current and the coil's inductance was measured by a LCR-bridge. According to the mentioned white paper, the electric conductivity of the negative electrode was supposed to increase with an increased level of lithiation. Consequently, eddy currents induced by the air coil were supposed to be increased in higher SOC, which causes a reduction of the air coil's inductance according to Lenz's law. In order to investigate the influence of the skin depth, the excitation frequency was varied between 20 kHz and 200 kHz.

Although small in magnitude, a linear relationship between the inductance of the sense coil and the SOC was measured [41]. Encouraged by these results, the same experiments were carried out in a cylindrical $LiFePO_4$ battery and yielded ambiguous results. As a possible explanation, the battery's charge-dependent expansion is assumed to be responsible for the different outcomes. The intercalation of lithium ions in the negative electrode's active material (usually graphite) is accompanied by a volumetric expansion of the electrode up to 10%. It turned out that the change of inductance arose most likely from this charge dependent expansion rather than from the alteration of the magnetic and electrical properties of the battery's active materials. Since the cylindrical package is significantly more stiff than the soft pouch package, the expansion is reduced and the internal arrangement of the metal foils remains unchanged. The conclusion which can be drawn from the results is that the sensitivity of the LCR-bridge method is much too low to detect the alteration of electromagnetic quantities of the battery's active material.

Nevertheless, according to the theory presented before, the level of lithiation has distinct influence on the magnetic properties of the positive electrode's active material. Hence, more refined laboratory facilities were sought, which concluded in a fruitful cooperation with the Department of Experimental Physics at the Institute of Physics at the University of Graz. Prof. Dr. Heinz Krenn established the research area of magnetometry and photonics there and operates a cryogenic laboratory equipped with a Quantum Design MPMS XL7 magnetic property measurement system. The operation of this measurement system is based on a superconducting quantum interference device (SQUID) magnetometer, cooled with liquid helium, and is consequently best suited to detect the smallest deviations of the magnetic susceptibility for temperatures between 1.7 K and 400 K.

However, the sample chamber and the arrangement of the coils of the MPMS XL7 measurement system restrict the samples to be cylindric and less than 8 mm in diameter and 8 mm of maximum height. Unfortunately, since $LiFePO_4$ batteries are preferably used in high-power applications, there are no commercial $LiFePO_4$ batteries available on the market which fulfill these constraints. As a workaround, it was decided to examine the charge-dependent alteration of the magnetic susceptibility of the positive electrode by investigating differently oxidized nanoporous $LiFePO_4$ samples. For this purpose, samples were extracted from both powder mixtures and

commercial available $LiFePO_4$ batteries.

Unfortunately, the sample preparation proved to be challenging. Since the aim of the experimental evaluation was to investigate the change of magnetic susceptibility related to the oxidation state of the transition metal ions in the positive electrode, the samples had to be prevented from uncontrolled oxidation. A professional sample preparation was performed in a cooperation with Ass. Prof. Dr. Roland Fischer from the Institute of Inorganic Chemistry at Graz University of Technology. Thanks to his efforts, two studies could be carried out.

In a first step, differently concentrated $LiFePO_4/FePO_4$ powder mixtures were analyzed, followed by a study of samples of positive electrodes from differently charged identical batteries. In the case of the latter, the disassembly of the charged batteries proved to be challenging since short circuits do not only represent an immanent safety risk but also distort the desired level of lithiation in an irreproducible manner.

For both experiments, the samples were packed in cylindrical aluminum capsules which were sealed using epoxy adhesives. Aluminum was chosen for the capsules for two reasons. First, it provides a steam-tight housing, necessary to prevent the samples from uncontrolled oxidation. Second, the magnetic moment of aluminum is mainly determined by a temperature-independent diamagnetic contribution to the magnetic susceptibility. Consequently, the capsule contributes to the measured magnetization only with a small and temperature-independent negative ground signal. To place the samples in the sample chamber of the MPMS XL7 measurement system, a thin-walled sealed aluminum tube was used as sample holder. In order to minimize contaminations, especially the importing of oxygen, the installation of the sample capsule was done in a helium atmosphere. The arrangement of the sample capsule in the sample holder is schematically illustrated in Figure 4.4.

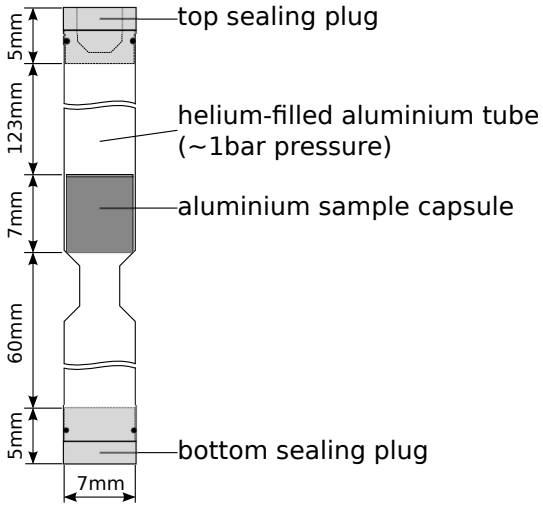

Figure 4.4.: Scheme of the SQUID sample holder. A thin-walled aluminum tube of 7 mm outer diameter was used to put the sample capsule into the SQUID magnetometer. In order to minimize contaminations, the capsules were installed in a helium atmosphere [43].

4.2.2. Powder Samples

Due to the challenges associated with the preparation of the samples extracted from charged batteries, samples of differently concentrated $LiFePO_4/FePO_4$ powder mixtures were investigated in a first step. For this purpose, (battery grade) pure $LiFePO_4$ powder was chemically delithiated employing NO_2BF_4 following the reaction

$$LiFePO_4 + NO_2BF_4 \rightleftarrows FePO_4 + LiBF_4 + NO_2\,.$$

The thus obtained $FePO_4$ powder was used in combination with the $LiFePO_4$ powder to prepare samples of different $LiFePO_4/FePO_4$ concentrations by mechanically mixing of both materials. This approach was chosen as major parts of the electrode reaction are dominated by the coexistence of a lithium rich phase and a lithium poor phase. Consequently, such prepared samples should yield a magnetic response which is directly comparable to materials prepared via electrochemical lithiation or delithiation, respectively. As can be seen in Table 4.1, 7 samples of powder mixtures have been prepared, whereby the levels of lithiation were chosen to be nearly uniformly distributed between 0% (sample #7) and 100% (sample #1).

As already mentioned several times, $LiFePO_4$ batteries are preferably used in high-power automotive applications. Hence, an SOC sensor based on magnetic principles is required to operate in a relatively wide temperature range. In order to meet the conditions of such applications, the experiment was carried out with temperatures between $-20°C$ and $+60°C$. Since tension-induced influences on the magnetic moment could not be ruled out, the temperature's influence on the magnetic susceptibility was investigated with both a heating and a cooling cycle.

Sample #	Mass (mg)	$LiFePO_4$ (%)	$FePO_4$ (%)
1	205	0	100
2	185	13	87
3	201	27.5	72.5
4	211	52.8	47.2
5	206	76.4	23.6
6	222	90	10
7	194	100	0

Table 4.1.: Sample mass, $LiFePO_4$ and $FePO_4$ concentrations of the investigated powder mixtures. The samples were prepared by mechanically mixing single-phase $LiFePO_4$ and $FePO_4$ powder. The latter was obtained by chemically delithiating nanoporous $LiFePO_4$ powder.

Figure 4.5 shows the obtained courses of the temperature-dependent magnetic volume susceptibilities of the investigated powder mixtures. Apparently, in this low temperature span a small deviation from the expected results seems to appear. Although the magnetic volume susceptibility decreases with increasing temperature, the curves are approximated by an affine function of temperature rather than a reciprocal function which is characteristic for paramagnetism in a broader temperature range.

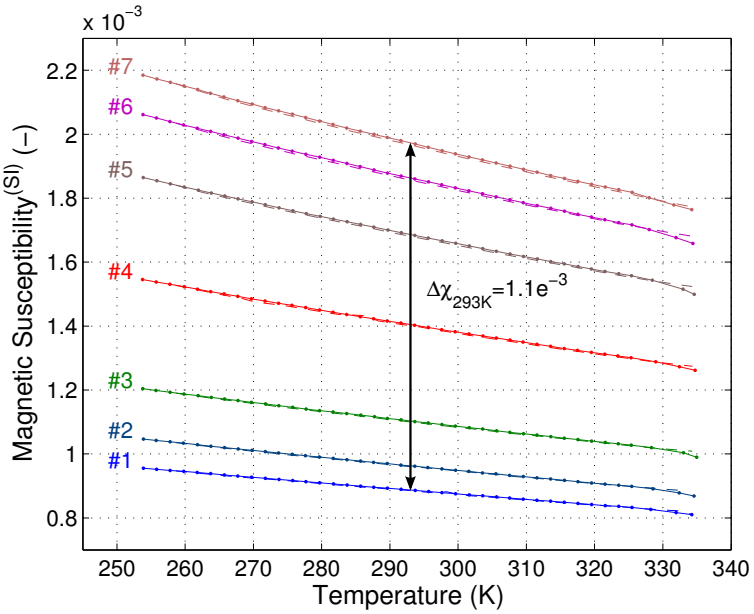

Figure 4.5.: Magnetic volume susceptibilities χ of differently delithiated $LiFePO_4$ and $FePO_4$ powder mixtures for both a cooling (solid line) and a heating (dashed line) cycle [42].

Although a direct correlation between the level of delithiation and the magnetic susceptibility can be observed, the fact that the measured magnetic susceptibility decreases with increasing level of delithiation is in direct contradiction to the assumptions made in section 4.1.4. Instead of an oxidation-induced increase in magnetic susceptibility of approximately 45%, a decrease of 45% is noticed at 20 °C. Consequently, the high-spin configuration can be ruled out for the delithiated case (Fe^{3+}). As possible explanation, the crystal field splitting energy Δ is presumably too low for the low-spin state but at the same time too high for the high-spin state, resulting in an energetically more favorable intermediate state. Hence, an electronic configuration of the Fe^{3+} ion accompanied by the total spin of $S = \frac{3}{2}$ reaches much better agreement with the results of the experiment. Assuming an alteration of the total spin number from $S = 2$ to $S = \frac{3}{2}$ corresponds to a decrease in magnetic susceptibility of 37.5% in the case of a totally quenched angular momentum. Since the measured magnetic susceptibility of the totally delithiated sample is even lower by 7.5% , this mismatch can be interpreted by a non-vanishing contribution of the orbital momentum to the effective magnetic moment μ_{eff}.

4.2.3. Battery Samples

The results reported in the previous section showed a direct relationship between the magnetic susceptibility and the level of delithiation of the powder mixture. However, positive electrodes are considerably more complex than simple binary mixtures of single-phase materials. Therefore, the question arises how representative these results for real batteries are. In order to answer this question, a second study was carried out. For this purpose, nine identical and "virgin" A123 26650m1B 2.5 Ah batteries were selected for sample extraction. Initially, ten full charge cycles were performed in order to guarantee full formation of the batteries. Afterwards, the

batteries were fully charged to the end-of-charge voltage of 3.6 V by means of a constant-current constant-voltage charging scheme corresponding to the minimum level of lithium in the positive electrode. Finally, the batteries were discharged by a certain charge amount Q_{dis} (see Table 4.2) to achieve approximately linear-distributed levels of lithiation.

Sample #	Mass (mg)	Q_{dis} (Ah)	C_{LiFePO_4} in (%)
A	284	-2.5	100
B	329	-2.1875	87.5
C	320	-1.875	75
D	342	-1.5625	62.5
E	327	-1.25	50
F	329	-0.9375	37.5
G	314	-0.625	25
H	320	-0.415	16.6
I	324	0	0

Table 4.2.: Sample mass, level of discharge and corresponding $LiFePO_4$ concentrations with respect to the nominal capacity of the disassembled batteries of 2.5 Ah. The samples were prepared by extracting parts of the positive electrode of differently charged identical $LiFePO_4$ batteries.

The charged batteries were disassembled in nitrogen atmosphere in a glove box and samples were extracted by stamping out snippets of different parts from the positive electrodes of the batteries. These snippets were filled into sealed aluminum capsules and the same experimental conditions were applied similar to the study of the powder samples. On the assumption of nearly identical batteries[7], the magnetic susceptibility of these samples should show a direct relationship to the level of discharge. According to the previous study on intermediate spin states, the effective magnetic moment μ_{eff} is expected to increase with the level of lithiation from the lithium rich (#A) to lithium depleted (#I) samples.

As can be seen in Figure 4.6, the measured magnetic volume susceptibilities show a reciprocal temperature dependence characteristic for paramagnetism. Compared to the results of the previous experiment, the overall alteration of susceptibility with respect to the level of delithiation is reduced by the factor of five. Since the battery's positive electrode is not entirely composed of nanoporous $LiFePO_4$ (filling factor < 1), the magnetic susceptibility is expected to be reduced. In addition to the active material, nonmagnetic carbon, binder and filler materials, parts of the aluminum current collector foil as well as non-volatile constituents of the electrode contribute to the sample's mass without magnetic response. $LiFePO_4$ contributes about 60% to the total mass of the battery. Accordingly, the reduction of magnetic susceptibility to this extent is not surprising at all.

[7]This assumption is due to the fact that all disassembled batteries stemmed from the same production batch.

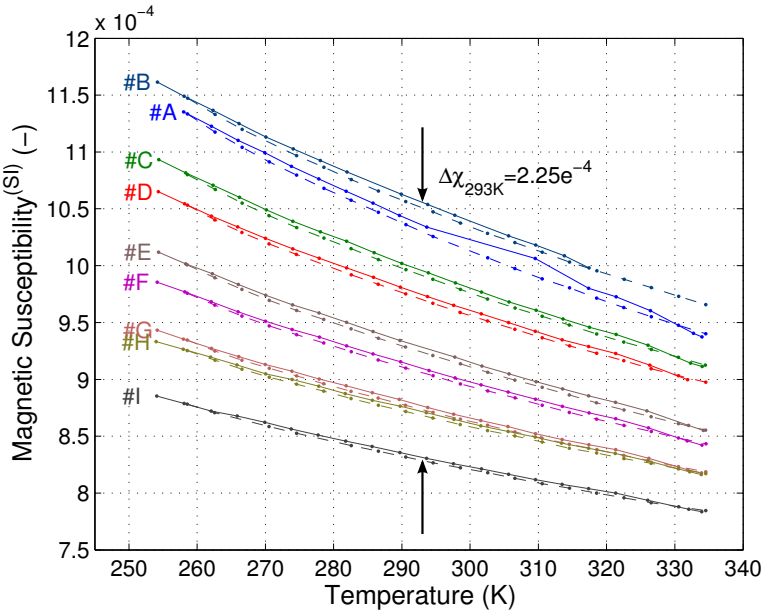

Figure 4.6.: Magnetic volume susceptibilities χ of samples extracted from the positive electrodes of differently charged identical A123 26650m1-B batteries in dependence of the temperature. Both a cooling (solid line) and a heating cycle (dashed line) was investigated [43].

It is also striking that the curves are not uniformly distributed according to the charge levels specified in Table 4.2. A smaller magnetic moment has been measured for sample #A than for sample #B and the distance between the curves of samples #G and #H appears to be much smaller than expected. This can be interpreted as a deviation which is most likely caused by imprecisions in the sample preparation. In view of the challenging sample preparation in the nitrogen glove box, such deviations cannot be avoided. In order to demonstrate the alteration of the paramagnetic contribution to the magnetic volume susceptibility, the results of the heating cycle were taken to adapt $\frac{a}{\vartheta}$-reciprocal curves (see eq. 4.9). By means of these curves, the measurements can be deliberated from parasitic magnetic components in order to determine the remaining paramagnetic contribution (= mapping to a filling factor of 1). As can be seen in Figure 4.7, the fitted curves coincide very well with the measurements. This confirms the paramagnetic behavior of the positive electrode within the given range of temperature. In addition, the nearly equidistant spaces between the curves indicate a quadratic increase of the effective magnetic moment μ_{eff} with a linearly increasing level of lithiation in the positive electrode. This circumstance is in agreement with the specified levels of discharge shown in Table 4.2.

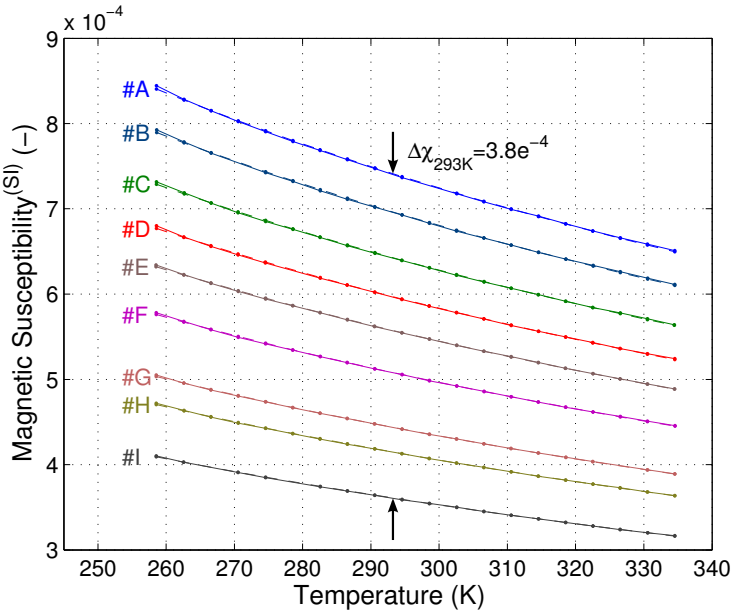

Figure 4.7.: Paramagnetic contribution to the magnetic volume susceptibilities of differently charged samples of $LiFePO_4$ electrodes in dependence of the temperature. The results of the heating cycle (Figure 4.6) were used to fit $\frac{a}{\vartheta}$-reciprocal curves (dashed lines). By means of these curves, the measured magnetic magnetic volume susceptibilities were freed from the magnetic bias components (solid lines). Apparently, the fitted curves nearly coincide with the measurements.

After normalization to a filling factor of 1 in the specimens, the magnetic volume susceptibility can be expected to decrease down to 51.3% with increasing lithium content. Although the total variation is slightly increased, this can be interpreted by the alteration of the total spin number from $S = 2$ to $S = \frac{3}{2}$. Similar to the results presented before, the difference to the theoretical value obtained by the spin-only formula can be explained by an additional contribution to the effective magnetic moment induced by non-vanishing orbital moments.

The findings presented in this section prove that the level of lithiation of the battery's positive electrode is directly related to the active material's magnetic susceptibility. In contradiction to the theoretical values obtained by assuming the high-spin electronic configuration of the transition ion and a totally quenched orbital momentum, the magnetic susceptibility is enhanced with an increasing level of lithiation corresponding to an intermediate spin state $S = \frac{3}{2}$ of the Fe^{3+}-ions. Additionally, the total alteration is slightly larger than expected, indicating that the orbital momentum is not entirely quenched.

However, the aim of these experiments was to derive the order of magnitude of the charge dependent alteration of the magnetic susceptibility in view of a novel sensor concept. Consequently, the detailed theoretical interpretation of the findings is closed at this point.

4.3. Sensor Placement

So far, the magnetic properties of the battery's cathode material has been investigated. The question is how these findings can be utilized to measure the SOC with an induction sensor. In order to determine the required magnetic field sensitivity as well as the optimal sensor placement for an induction sensor, the spatial distribution of the magnetic **B**-field is evaluated for the case of a cylindrical geometry. For parametrization, the actual dimensions of the investigated A123 26650m1B batteries were used.

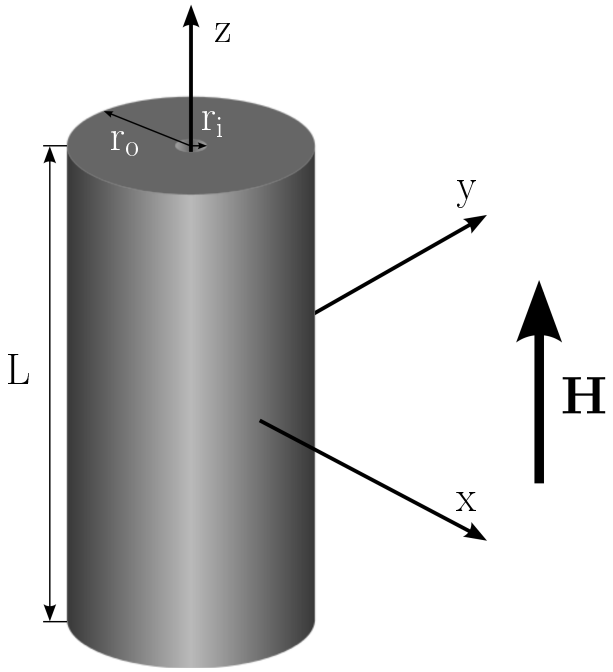

Figure 4.8.: Simplified cylindrical geometry of a 26650-battery package. The components of the battery are represented by a cylinder of homogeneous magnetization. In order to meet realistic conditions, a production-related coaxial hole was placed in the center of the battery with an inner radius r_i. The cylinder is assumed to be exposed to a homogeneous **H**-field oriented along the z-direction.

4.3.1. Mathematical Formulation

In magnetostatics, the magnetic vector potential **A** of a magnetized body is given by

$$\mathbf{A}(\mathbf{r}) = \frac{\mu_0}{4\pi}\int_V \frac{\mathbf{J}_V(\mathbf{r}')}{|\mathbf{r}-\mathbf{r}'|}dV' + \frac{\mu_0}{4\pi}\oint_S \frac{\mathbf{J}_S(\mathbf{r}')}{|\mathbf{r}-\mathbf{r}'|}dS' \tag{4.11}$$

where $\mathbf{J}_V(\mathbf{r}) = \nabla \times \mathbf{M}$ denotes an equivalent magnetization current density in the body, and $\mathbf{J}_S(\mathbf{r}) = \mathbf{M} \times \mathbf{n}$ is an equivalent current density on the surface of the body with surface normal vector **n**. Let us assume a homogeneously magnetized rigid body shown in Figure 4.8. The first term of eq. 4.11 vanishes due to the

homogeneous magnetization. The second term is reduced to a surface integral with respect to the outer and inner cylindrical surface since the surfaces at the top and bottom do not contribute due to symmetry. Consequently, the expression for the magnetic vector potential is represented by the magnetization distributions on the shell surfaces.

$$\mathbf{A}(\mathbf{r}) = \underbrace{\frac{\mu_0}{4\pi}\int_{S_o}\frac{\mathbf{M}(\mathbf{r}')\times\mathbf{n}'_o}{|\mathbf{r}-\mathbf{r}'|}dS'}_{=:\mathbf{A}_o(\mathbf{r})} + \underbrace{\frac{\mu_0}{4\pi}\int_{S_i}\frac{\mathbf{M}(\mathbf{r}')\times\mathbf{n}'_i}{|\mathbf{r}-\mathbf{r}'|}dS'}_{=:\mathbf{A}_i(\mathbf{r})}. \tag{4.12}$$

The expressions for $\mathbf{A}_o(\mathbf{r})$ and $\mathbf{A}_i(\mathbf{r})$ for the outer and inner shell differ only with respect to the radius at the surfaces and the radial orientation of surface normal vector. For the sake of clarity, only the solution for $\mathbf{A}_o(\mathbf{r})$ is presented in the following.

The geometry of the battery package suggests an evaluation of the surface integral in cylindrical coordinates. Consequently, the observation and source point are given by $\mathbf{r} = r\mathbf{e}_r + z\mathbf{e}_z$ and $\mathbf{r}' = r_o\cos(\varphi')\mathbf{e}_r + r_o\sin(\varphi')\mathbf{e}_\varphi + z'\mathbf{e}_z$, respectively, r_o being the radius of the outer surface. The surface normal vector is given by $\mathbf{n}' = \cos(\varphi')\mathbf{e}_r + \sin(\varphi')\mathbf{e}_\varphi$ and the magnetization is assumed to be homogeneous and in z-direction orientated according to

$$\mathbf{M}(\mathbf{r}') = \begin{cases} M\mathbf{e}_z & \text{for } |z'| \leq \frac{L}{2} \\ \mathbf{0} & \text{else} \end{cases}. \tag{4.13}$$

Consequently, the contribution to the magnetic vector potential related to magnetization currents $\mathbf{M}\times\mathbf{n}_o$ on the outer surface is given by

$$\begin{aligned}\mathbf{A}_o(\mathbf{r}) = \frac{\mu_0 r_o M}{4\pi}\Bigg[&\int_0^{2\pi}\int_{-\frac{L}{2}}^{\frac{L}{2}}\frac{-\sin(\varphi')d\varphi'dz'}{\sqrt{r^2+r_o^2+(z-z')^2-2r_o r\cos(\varphi')}}\mathbf{e}_r + \\ &\int_0^{2\pi}\int_{-\frac{L}{2}}^{\frac{L}{2}}\frac{\cos(\varphi')d\varphi'dz'}{\sqrt{r^2+r_o^2+(z-z')^2-2r_o r\cos(\varphi')}}\mathbf{e}_\varphi\Bigg].\end{aligned} \tag{4.14}$$

The radial component of $\mathbf{A}_o(\mathbf{r})$ vanishes, which can easily be demonstrated using the substitution $\cos(\varphi') = x$ and evaluating the integral with respect to x.

$$\begin{aligned}\int_0^{2\pi}\frac{-\sin(\varphi')d\varphi'}{\sqrt{r^2+r_o^2+(z-z')^2-2r_o r\cos(\varphi')}} &= \\ \frac{-1}{r_o r}\sqrt{r^2+r_o^2+(z-z')^2-2r_o r x}\Big|_{x_0}^{x_1} &= \\ \frac{-1}{r_o r}\sqrt{r^2+r_o^2+(z-z')^2-2r_o r\cos(\varphi')}\Big|_0^{2\pi} &= 0\end{aligned}$$

Unfortunately, the determination of the azimuthal component of $\mathbf{A}_o(\mathbf{r})$ is less straightforward since an analytical treatment of the according integral is not tractable. However, $\mathbf{A}_o(\mathbf{r})$ can be expressed in terms of complete elliptic integrals of the first and second kind which at least allows a closed evaluation of (4.14).

By means of the identity $\cos(\alpha) \equiv 2\cos(\frac{\alpha^2}{2}) - 1$ and the definition

$$k_{r_o}^2 := \frac{4r_o r}{(r+r_o)^2 + (z-z')^2}, \tag{4.15}$$

the term under the square root can be expressed according to

$$r^2 + r_o^2 + (z-z')^2 - 2r_o r\cos(\varphi') = \frac{k_{r_o}^2}{4r_o r}\left(1 - k_{r_o}^2\cos^2\left(\frac{\varphi'}{2}\right)\right). \tag{4.16}$$

Again, using the identity $\cos(\alpha) \equiv 2\cos(\frac{\alpha^2}{2}) - 1$ and the substitution $\theta' = \frac{\varphi'}{2}$ allows a formulation of the integral with respect to φ' given by

$$\int_0^{2\pi} \frac{\cos(\varphi')d\varphi'}{\sqrt{r^2 + r_o^2 + (z-z')^2 - 2r_o r\cos(\varphi')}} = \frac{4\sqrt{r_o r}}{k_{r_o}} \int_0^{\pi} \frac{2\cos^2(\theta') - 1}{\sqrt{1 - k_{r_o}^2\cos^2(\theta')}} d\theta'. \tag{4.17}$$

Since the integrand on the right-hand side is a symmetric and periodic function in θ' with periodicity π, it suffices to integrate only from 0 to $\frac{\pi}{2}$. In conjunction with the substitution $t = \cos(\theta')$, this circumstance allows to express eq. 4.17 in terms of complete elliptic integrals of the first and second kind, respectively according to Appendix B (see eq. B.4 and eq. B.5).

$$\frac{4\sqrt{r_o r}}{k_{r_o}} \int_0^{\pi} \frac{2\cos^2(\theta') - 1}{\sqrt{1 - k_{r_o}^2\cos^2(\theta')}} d\theta' =$$

$$\frac{8\sqrt{r_o r}}{k_{r_o}^3}\left((2 - k_{r_o}^2)\underbrace{\int_0^{\frac{\pi}{2}} \frac{d\theta'}{\sqrt{1 - k_{r_o}^2\cos^2(\theta')}}}_{=K(k_{r_o})} - 2\underbrace{\int_0^{\frac{\pi}{2}} \sqrt{1 - k_{r_o}^2\cos^2(\theta')} d\theta'}_{=E(k_{r_o})}\right) \tag{4.18}$$

Consequently, the contribution to the magnetic vector potential from the total outer surface is given by

$$\mathbf{A}_o(\mathbf{r}) = \frac{2\mu_0\sqrt{r}M}{\pi} r_o^{\frac{3}{2}} \int_{-\frac{L}{2}}^{\frac{L}{2}} \frac{(2 - k_{r_o}^2)K(k_{r_o}) - 2E(k_{r_o})}{k_{r_o}^3} dz' \mathbf{e}_\varphi. \tag{4.19}$$

According to eq. 4.12 the overall magnetic vector potential for both shells expressed in terms of complete elliptic integrals of the first and second kind is given by

$$\mathbf{A}(\mathbf{r}) = \frac{2\mu_0\sqrt{r}M}{\pi}\left(r_o^{\frac{3}{2}} - r_i^{\frac{3}{2}}\right) \int_{-\frac{L}{2}}^{\frac{L}{2}} \frac{(2 - k_{r_o}^2)K(k_{r_o}) - 2E(k_{r_o})}{k_{r_o}^3} -$$
$$\frac{(2 - k_{r_i}^2)K(k_{r_i}) - 2E(k_{r_i})}{k_{r_i}^3} dz' \mathbf{e}_\varphi. \tag{4.20}$$

Once this integral is computed, the components of the magnetic **B**-field can be determined. In cylindrical coordinates these are

$$\mathbf{B}\left(\mathbf{r}\right) = \nabla \times \mathbf{A} = -\frac{\partial A_\varphi}{\partial z}\mathbf{e}_r + \frac{1}{r}\frac{\partial}{\partial r}\left(rA_\varphi\right)\mathbf{e}_z. \tag{4.21}$$

Since the problem is rotationally symmetric with respect to the z-axis, the components of the **B**-field are restricted to the xz-plane to:

$$B_x(x,z) = -\frac{\partial A_\varphi}{\partial z} \tag{4.22a}$$

$$B_y(x,z) = 0 \tag{4.22b}$$

$$B_z(x,z) = \frac{1}{x}A_\varphi + \frac{\partial A_\varphi}{\partial x} \tag{4.22c}$$

4.3.2. Numerical Evaluation

The following results were obtained by numerically integrating eq. 4.20 by using an adaptive Gaussian quadrature method. The geometry of a 26650-battery package (r_o = 13 mm, L = 65 mm) was used for parametrization. The disassembly of the investigated A123 25550 $LiFePO_4$ batteries revealed an inner diameter of the center's bore of 4 mm. According to eq. 4.13, the magnetized part in the battery is assumed as M = const. The magnitude of the magnetization was chosen to be $M = \Delta\chi H$ where $\Delta\chi$ is parameterized by means of the charge induced total variation in magnetic suceptibility at 20 °C highlighted in Figure 4.7. Since $LiFePO_4$ contributes approximately 60% to the total mass of the battery, the experimentally determined value was modified to $\Delta\chi = 2.28{\cdot}10^{-4}$. By analogy with the experiments in the lab, the magnitude of the **H**-field is parametrized by $H = 50$ Oe (≈ 3979 A/m).

For the given configuration the numerical determination of the emanating **B**-field in the xz-plane results in the radial and axial false color represented perspective components shown in Figure 4.9 and Figure 4.10, respectively. Except for the enhanced contributions at the edges of the hollow cylinder, the azimuthal x-component almost vanishes. Except from these overemphasized contributions (caused by ignoring demagnetization effects at the edges as well the numerical approximation of the curl operator), the x-component of the emanating **B**-field can be assumed to be negligible. By contrast, the false color representation of the z-component proves to be more informative. As can be seen in Figure 4.10 and Figure 4.11, the alteration of the magnetic susceptibility causes a dominant alteration of the z-component inside the magnetized matter of the hollow cylinder. If the magnetization is homogeneous, the optimal location for an induction sensor is centered in the horizontal sense but shifted in the vertical sense in such a way that the induction sensor is placed just in the middle of the battery's stacked and coiled structure.

In this position, the swing of the **B**-field is in the range of tenths of mT and therefore promises good detectability by state-of-the-art induction sensors. Unfortunately, the placement of an induction sensor between the stacked electrodes proves to be disadvantageous due to production-related reasons. Hence, the central bore is the most natural choice for the sensor placement. However, Figure 4.10 demonstrates that the magnetic sensitivity of an induction sensor is much more restricted if the sensor is located in the bore.

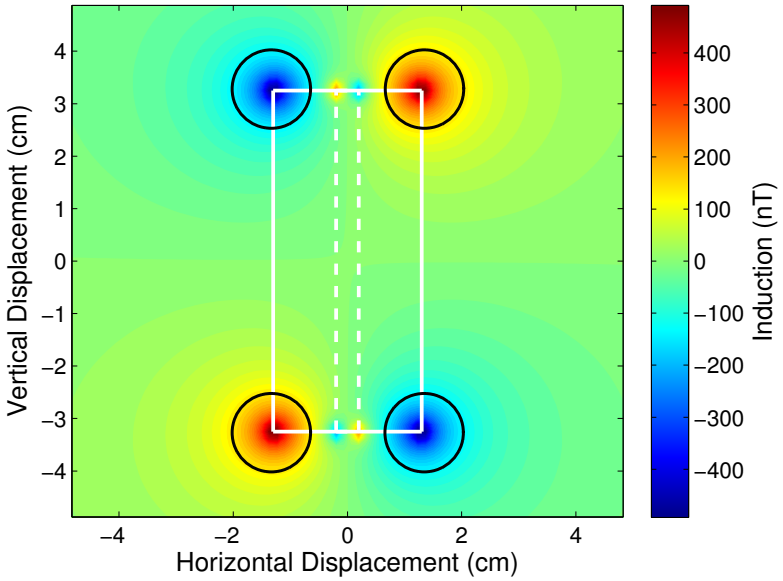

Figure 4.9.: False color representation of the azimuthal x-component of the emanating **B**-field for the battery-like cylinder (26650-battery package with a centered 4 mm bore) in the case of a homogeneous magnetization induced by an **H**-field of 50 Oe and for a total alteration of the volumetric magnetic susceptibility of $\Delta\chi = 2.28 \cdot 10^{-4}$. The misleading contributions at the edges (black circles) are caused by ignoring demagnetization effects and the numerical approximation of the curl operator.

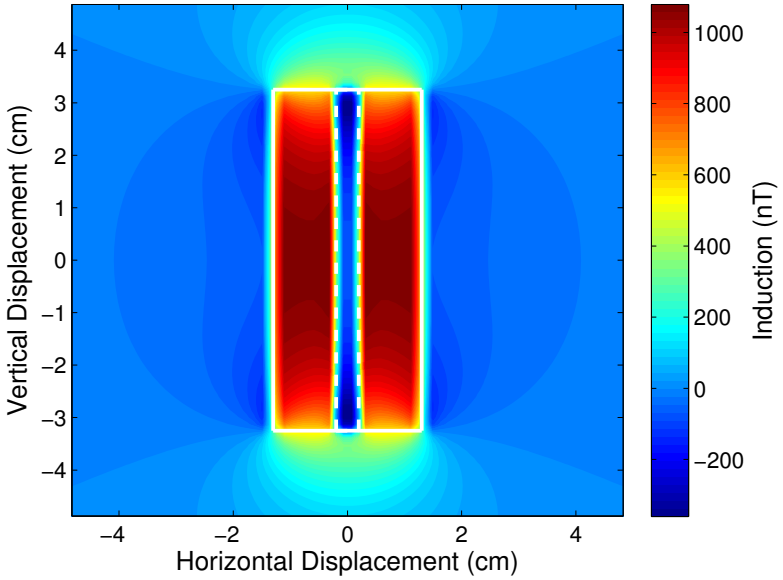

Figure 4.10.: False color representation of the z-component of the emanating **B**-field for the battery-like cylinder (26650-battery package with a centered 4 mm bore) in the case of a homogeneous magnetization induced by an **H**-field of 50 Oe and for a total alteration of the volumetric magnetic susceptibility of $\Delta\chi = 2.28 \cdot 10^{-4}$.

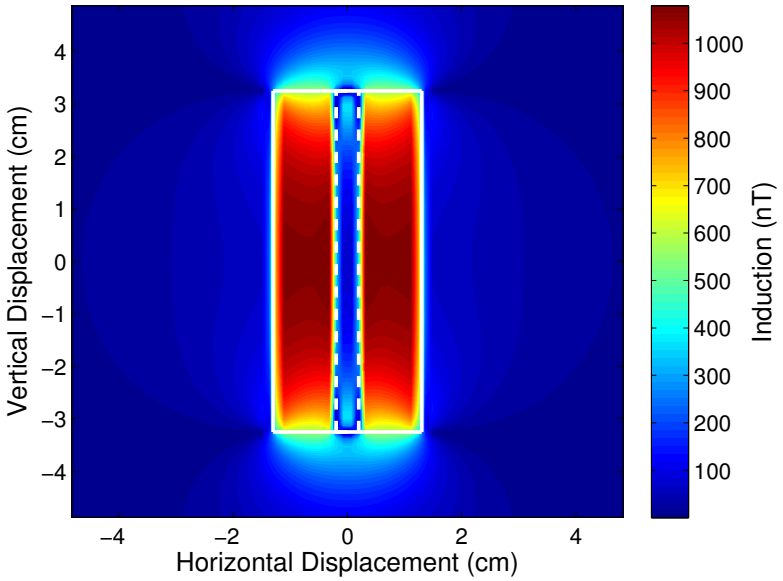

Figure 4.11.: Absolute values of the numerically determined z-component of the emanating **B**-field for the battery-like cylinder (26650-battery package with a centered 4 mm bore) as shown in Figure 4.10 to illustrate the optimum for locating an SOC sensor based on magnetic principles.

The formulation of the problem by means of complete elliptic integrals of the first and second kind proves to be problematic if the axial dependence of the magnetic **B**-field is considered. This circumstance is due to the fact that the expression of the magnetic vector potential (see eq. 4.20) cannot be evaluated if $r = 0$ since the elliptic moduli k_{r_o} and k_{r_i} vanish. Consequently, the expression in the integral becomes singular. Fortunately, for just this case, the magnetic **B**-field can easily be determined in a closed analytic form. Similar to the derivation of the magnetic vector potential shown above, the **B**-field is derived by means of an equivalent magnetic surface current density ($\mathbf{M} \times \mathbf{n}$) on the outer and inner lateral surface of the battery-like cylinder. Since the radial components vanish alongside the z-axis, the infinitesimal small contribution to the axial **B**-field is given by applying Biot-Savart's law according to

$$dB_z(z) = \frac{\mu_0 \Delta\chi H}{4\pi} \left[\oint \frac{\mathbf{e}_z \left(d\mathbf{s}_o \times (\mathbf{r} - \mathbf{r}'_o) \right)}{|(\mathbf{r} - \mathbf{r}'_o)|^3} - \oint \frac{\mathbf{e}_z \left(d\mathbf{s}_i \times (\mathbf{r} - \mathbf{r}'_i) \right)}{|(\mathbf{r} - \mathbf{r}'_i)|^3} \right] d\acute{z}. \tag{4.23a}$$

By using the definitions

$$d\mathbf{s}_o = r_o d\varphi \mathbf{e}_\varphi \tag{4.23b}$$

$$d\mathbf{s}_i = r_i d\varphi \mathbf{e}_\varphi \tag{4.23c}$$

$$\mathbf{r} - \mathbf{r}'_o = -r_o \mathbf{e}_r + (z - \acute{z}) \mathbf{e}_z \tag{4.23d}$$

$$\mathbf{r} - \mathbf{r}'_i = -r_i \mathbf{e}_r + (z - \acute{z}) \mathbf{e}_z, \tag{4.23e}$$

the axial magnetic **B**-field is obtained by integrating eq. 4.23a with respect to the length of the battery-like cylinder according to

$$B_z(z) = \int_{-\frac{L}{2}}^{\frac{L}{2}} dB_z(z)d\acute{z} = \frac{\mu_0 \Delta\chi H}{4\pi}\left[\frac{z+\frac{L}{2}}{\sqrt{r_o^2+\left(z+\frac{L}{2}\right)^2}} - \frac{z-\frac{L}{2}}{\sqrt{r_o^2+\left(z-\frac{L}{2}\right)^2}} - \right.$$
$$\left. \frac{z+\frac{L}{2}}{\sqrt{r_i^2+\left(z+\frac{L}{2}\right)^2}} + \frac{z-\frac{L}{2}}{\sqrt{r_i^2+\left(z-\frac{L}{2}\right)^2}}\right]. \quad (4.23f)$$

By evaluating this closed form solution, the distribution of the magnetic **B**-field is determined for the entire interesting space. Additionally, by means of the analytic solution, the accuracy of the numerically determined distribution of the **B**-field can easily be verified. In Figure 4.12, both the analytic solution (blue line) and the numerically derived curve of the z-component of the **B**-field (red line) are compared. As mentioned before, eq. 4.20 cannot be evaluated for $r = 0$, therefore, the latter is evaluated for the closest numerically determined locus being shifted by 650 µm (the grid size was 1.3 mm) from the z-axis. Since the curves shown in Figure 4.12 nearly coincide, it is justified that the numerical integration of eq. 4.20 converges to the correct values.

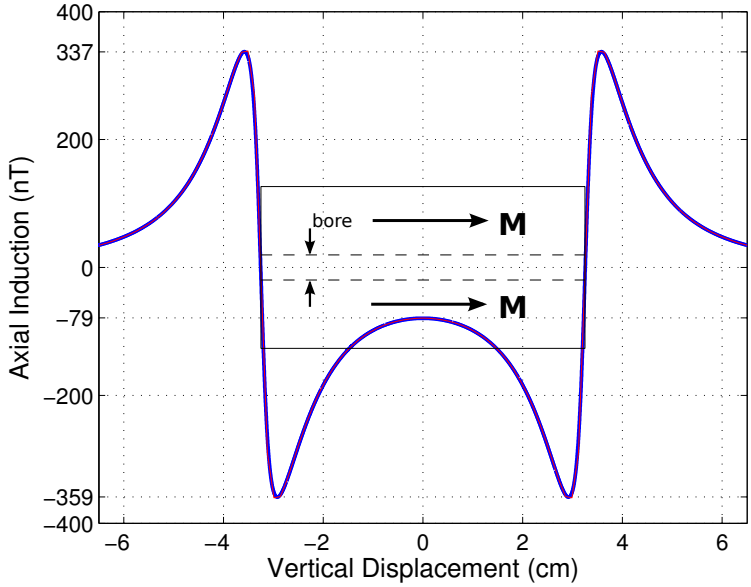

Figure 4.12.: Emanating axial **B**-field for the battery-like cylinder (26650-battery package with a centered 4 mm bore) in the case of a homogeneous magnetization induced by an **H**-field with 50 Oe in magnitude and a total alteration of the volumetric magnetic susceptibility of $\Delta\chi = 2.28 \cdot 10^{-4}$. The blue line shows the analytical solution obtained by applying Biot-Savart's law, while the red line corresponds to closest (x = 650 µm) axial numerical data using eq. 4.20 and 4.21.

For the sake of completeness, however, it should be mentioned that the ratio between the inner and the outer radius has a distinct influence on the accuracy of the numerically determined values of the **B**-field. Reducing the inner radius by e.g. 0.5 mm causes the quadrature integration method to converge to a wrong value and the numerically determined z-component of the **B**-field is strongly biased in the vicinity of the z-axis.

Finally, it must be clarified that the magnetization of the cylindric shell was chosen to be homogeneous in order to efficiently calculate the corresponding surface integrals by means of complete elliptic integrals of the first and second kind. This situation is presumably not encountered in practice since the application of a homogenous magnetic **H**-field is required to detect the alteration of the magnetic susceptibility χ. However, the **H**-field in the magnetized body of the battery is most likely non-homogeneous and not completely aligned along the z-axis, with the consequence of a deformation of the axial magnetic field.

Nevertheless, the results presented in this chapter proved that the level of lithiation has a measurable influence on the magnetic properties of the $LiFePO_4$ battery's positive electrode. Furthermore, it was demonstrated that the expected alteration of the positive electrode's magnetic susceptibility is principally detectable by state-of-the-art induction sensors in a (sub-)Microtesla field range at moderate biasing fields of 50 Oe.

5. Conclusion and Outlook

The motivation for writing this thesis arises from the challenge to monitor the state of charge (SOC) of $LiFePO_4$ batteries in high-power applications. As mentioned several times, the shortcomings of the state-of-the-art methods for SOC estimation stem from the $LiFePO_4$ battery's characteristics depending mapping of the SOC on the open circuit voltage U_{OCV}. Based on the experimental evaluation of the open circuit voltage in the lab, it was demonstrated in chapter 2 that the open circuit voltage shows a flat dependence on the state of charge in large ranges and is significantly influenced by hysteresis phenomena.

In the thesis, two different approaches were investigated to tackle the problems associated with the above mentioned SOC-mapping. Although both approaches support the same purpose, they differ significantly with respect to the underlying principles. According to this circumstance, the thesis is finalized by summarizing both approaches separately.

Bayesian Filtering

Based on the empirically obtained findings of the mapping between the state of charge and the open circuit voltage U_{OCV} presented in chapter 2, a nonlinear state space model for the battery's dynamics was introduced which is capable to cope with the ambiguous mapping between the state of charge and the open circuit voltage U_{OCV}. In chapter 3, a joint estimation framework utilizing a sequential Monte Carlo method (particle filtering) was presented in order to simultaneously estimate the states $\mathbf{x}_k$ and parameters $\boldsymbol{\theta}$ of this state space model. Since the dimensionality of the augmented state space model exceeds the practical range of particle filtering, a variance reduction method based on the concept of sufficient statistics (Rao-Blackwellization) was applied.

Simulation studies carried out in a first step by means of realistic load scenarios, which are typical of hybrid electric vehicle drive trains, yielded promising results. The trajectories of the states and, thus, the simulated state of charge, as well as the parameters were accurately estimated independent of the charge quantities associated with charging/discharging. In order to investigate whether the proposed estimator overcomes the shortcomings of state-of-the-art methods in connection with inaccurate current measurements, the current signal was artificially distorted by significant systematic errors. The simulation studies showed that the proposed estimation framework overcomes the problems associated with the current distortions. This circumstance proves the applicability of methods invoking statistical inference associated with the problematic correlation between the state of charge and the open circuit voltage U_{OCV}.

Encouraged by the outcomes of the simulation studies, the performance of the proposed joint estimation framework was compared with real measurements obtained by experimentally evaluating a hybrid test cycle in the lab. Unfortunately, this investigation yielded sobering results since significantly biased estimates are achieved

by the proposed estimator with non-negligible probability. Fortunately, a modification of the proposed estimator by estimating an acceptance threshold solved the problem of the significantly biased estimates.

However, the impact of distorted current measurements proved to be only partly compensated by the estimator. Consequently, the estimator requires similar to state-of-the-art SOC estimation methods highly accurate current measurements. Moreover, the estimates of the remaining trajectories as well the parameter courses do not meet the expected courses. In order to investigate this circumstance, two possible causes can be taken into consideration.

The first cause may arise from problems associated with Rao-Blackwellized particle filters and poor mixing dynamic systems. In this context, the mixing property quantifies the dependency of the linear states of the conditionally Gaussian state space model at time instant k on the history of the nonlinear states. Good mixing systems are characterized by the fact that the time lag in which this dependency is detectable is limited to some time steps. Hence, the conditionally linear states significantly vary with respect of time. In contrast, in poor mixing systems, this time lag corresponds to large parts of the trajectories of the nonlinear states.

In practice, the latter case proves to be problematic since Rao-Blackwellized particle filtering is usually based on a particle representation targeting the marginalized smoothing posterior density $p\left(\mathbf{x}_{0:k}|\mathbf{y}_{0:k}\right)$. If the mixing property is poor, the exact target distribution must be approximated by the importance sampler for time lags which reach far back into the past. However, due to the sample degeneracy problem and the associated workaround (resampling), this requirement can not be ensured. Consider, for example, the case of jointly estimating the states and static parameters of a linear Gaussian state space model. According to the explanation above, it is clear that Rao-Blackwellized particle filters fail to provide accurate estimates for this case. This circumstance is exactly the reason why the battery's nominal capacity is not incorporated in the estimation framework and must be known a priori. Nevertheless, the temporal alternation of the remaining parameters might also be too low in practice, causing the estimator potentially to converge to biased solutions.

In order to overcome the shortcomings associated with poor mixing systems in the context of Rao-Blackwellized particle filtering, Lindsten et al. [77] presented an alternative approach. The Rao-Blackwellized marginal particle filter is premised on the factorization $p\left(\boldsymbol{\theta}_k, \mathbf{x}_k|\mathbf{y}_{0:k}\right) = p\left(\boldsymbol{\theta}_k|\mathbf{x}_k, \mathbf{y}_{0:k}\right) p\left(\mathbf{x}_k|\mathbf{y}_{0:k}\right)$, which is basically motivated by the approach of Klaas et al. [60]. Instead of targeting the marginal smoothing posterior density, the particle filter's task is to target the marginal filtering density $p\left(\mathbf{x}_k|\mathbf{y}_{0:k}\right)$. Since sample degeneracy is not a problem for this case, the mixing properties of the state space model are of minor relevance. At first glance, the factorization used by Lindsten et al. looks like a simplification. Unfortunately, the opposite is the case since the conditional marginal density $p\left(\boldsymbol{\theta}_k|\mathbf{x}_k, \mathbf{y}_{0:k}\right)$ is not generally Gaussian but can be expressed by a Gaussian mixture model. As the components of this Gaussian mixture model increases exponentially with time, Lindsten et al. solved the problem by a single Gaussian density derived by means of moment matching. The major drawback of this approach is the significant increase of the computational demands. Native particle filtering (and, thus, the Rao-Blackwellized particle filter) operates in a complexity class of $\mathcal{O}(N)$, whereas the versions target-

ing $p(\mathbf{x}_k|\mathbf{y}_{0:k})$ possess a quadratic computational complexity $\mathcal{O}(N^2)$. Hence, this approach is clearly unfeasible for the practical implementation in a state of charge estimator.

Nevertheless, the concept of Rao-Blackwellized marginal particle filtering was adopted for joint estimating the states and parameters (including the nominal capacity C_n) of the state space model used in chapter 3. Due to the high computational demands, the performance of Rao-Blackwellized marginal particle filter was only evaluated by a few individual trails. The obtained results, not shown in this thesis, appeared to be improved but still significantly influenced by the systematic error of the current measurements. The conclusion which can be drawn is that the mixing properties of the proposed conditionally linear Gaussian state space model are presumable not (entirely) responsible for the poor performance of the proposed estimation framework in case of significantly biased current measurements.

The second potential cause is the presumably inaccurate model of the $LiFePO_4$ battery's dynamics. This circumstance is based on two facts. First, due to the exhausting relaxation periods, the upper and lower open circuit voltage curves were empirically determined by continuously charging/discharging the battery by means of a small operating current and measuring the battery's terminal voltage U_{term}. Hence, the obtained courses are rather approximations than the true open circuit voltage curves are. Due to the mentioned mapping between the state of charge and the open circuit voltage U_{OCV}, the inverse mapping relate small deviations of the open circuit voltage U_{OCV} to large deviations of the state of charge. Consequently, even small deviations of the open circuit voltage model prove to be problematic.

Furthermore, the battery's transient dynamics are modeled insufficiently. Recall that the transient contribution U_{trans} to the terminal voltage was incorporated by a time-varying linear subsystem of the first order. This is in agreement with most adaptive state-of-the-art approaches but apparently too simple to entirely cover the battery's transient dynamics.

Among the mentioned possible reasons for the poor performance of the Rao-Blackwellized joint estimation framework in case of significantly biased current measurements, the shortcomings associated with the dynamic model are presumably more serious than the slow mixing of the associated parameter courses. Consequently, it is necessary to consider a better dynamic model based on electrochemical principles. Thus, it is not surprising that modeling of $LiFePO_4$ batteries has recently been subject of extensive research. However, since some phenomena have not yet been understood, accurate dynamic models for $LiFePO_4$ batteries are still missing.

Another issue is the applicability of the dynamic model in practice. Consider, for example, a high-power application like a hybrid electric drive train of a public traffic bus. Since operating voltages up to 700 V are not unusual for these applications, at least 212 individual $LiFePO_4$ batteries connected in serial are required to nominally guarantee this voltage. This circumstance evokes special requirements for the battery management and explains why simple lumped component RC models are that widespread in this field. As a consequence, battery models derived from electrochemical (or other) principles are required to be as simple as possible to be applicable in a battery management system. With respect to the high level of complexity, this poses significant challenges by modeling the battery's dynamics.

Magnetic Sensing

In chapter 4, a novel approach for the determination of the state of charge of $LiFePO_4$ was presented. In contrast to the state-of-the-art methods for state of charge determination in battery systems, it was proposed to monitor the state of charge by the battery's magnetic properties. The motivation to determine the state of charge by magnetic sensing arises from the role of iron in the $LiFePO_4$ octahedral complex in the positive electrode's active material. The stoichiometry of Fe^{2+} versus Fe^{3+} ions and, thus, the state of oxidation is proportional to the amount of lithium removed from the positive electrode's active material. Since iron (a transition metal ion) is located in an octahedral crystal environment of ${PO_4}^{3+}$ complex, it is influenced by the ligands at the corners of the octahedron. The change of the iron ion's oxidation state from Fe^{2+} to Fe^{3+} is accompanied by a change of the compounds' magnetic moment.

The advantages of the proposed approach are clear: Since the amount of lithium ions removed from the positive electrode is indirect proportional to the battery's charge level, the positive electrode's magnetic susceptibility is directly related to the state of charge. Consequently, the shortcomings associated with the battery's flat and ambiguous mapping between the state of charge and the open circuit voltage U_{OCV} are canceled. Furthermore, this approach does not rely on an accurate model of the battery's dynamics or precise measurements of the operating current and the terminal voltage U_{term}.

However, the concomitant change of the magnetic moment of the transition ion spins has not yet been fully understood for practical detection of the state of charge in view of a sensor concept based on magnetic principles. Consequently, the results shown in chapter 4 correspond rather to a feasibility study than to the development of an serviceable state of charge sensor. Hence, the question is: How does the positive electrode's magnetic susceptibility alter with respect to the level of lithiation, and what is the sensitivity required by induction sensors in order to detect SOC-related magnetic susceptibility?

For this purpose, two SQUID studies of different sample configurations were carried out. In a first step, samples of differently oxidized powder mixtures were investigated. The obtained results confirmed the expected paramagnetic behavior but showed in contrast to the expected dependency a decrease of the magnetic moment with decreasing level of lithiation. In order to meet more realistic conditions, it was decided to carry out a second SQUID study of samples extracted from the positive electrode of identically and differently charged commercial $LiFePO_4$ batteries. Both studies yielded comparable results in-so-far, that the paramagnetic behavior and the direct relationship between the level of lithiation and the magnetic moment showed satisfactory agreement.

Finally, the results of the second study were used to quantify the change of the magnetic $\mathbf{B}$-field accompanied by the charge-induced swing of magnetic susceptibility for the case of a homogeneously magnetized body. The geometry of a cylindrical 26650-battery package was used as input parameters, whereby a production-related hollow shell geometry was incorporated. The aim of this investigation was to examine the most locations for the placement of an induction sensor and to prove the minimum sensitivity which must is required by the induction sensor. Depending on the location, the swing of induction proved to be in the range of some hundreds nT,

which affirms that the state of charge can be detected by state-of-the-art induction sensors.

However, the concept of determining the state of charge of $LiFePO_4$ batteries based on magnetic principles is still far from any practical realization of an according sensor concept since many details have not yet been clarified. For example, solely the positive electrode was considered for the investigations in this thesis. Thus, the question is how the magnetic properties of the entire battery are influenced. Furthermore, the used simulation of the magnetic vector potential is significantly inconvenient in the case of a non-homogeneous magnetized body, even if the battery was assumed to be magnetized by a homogeneous magnetic field of the order of 50 Oe. However, in view of a practical sensor implementation, the magnetization by a homogeneous magnetic field is presumably hard to realize. Moreover, disturbances like the earth's magnetic field or fields from the operating current presumably hamper in practice the determination of the battery's magnetic susceptibility.

To summarize, the findings presented here demonstrate the potential of state of charge sensing based on magnetic susceptibility monitoring. However, it must be mentioned that a series of further investigations are required to prove the applicability of a state of charge sensor in view of a novel sensor concept.

A. Multivariate Gaussian Distributions

A.1. Affine Transformations

Lemma A.1.1. *Let* $\mathbf{x}$ *and* $\mathbf{z}$ *conditioned on* $\mathbf{x}$ *be Gaussian distributed according to*

$$p(\mathbf{x}) = \mathcal{N}\left(\mathbf{x}; \boldsymbol{\mu}_{\mathbf{x}}, \boldsymbol{\Sigma}_{\mathbf{x}}\right) \tag{A.1a}$$

$$p(\mathbf{z}|\mathbf{x}) = \mathcal{N}\left(\mathbf{z}; \mathbf{A}\mathbf{x} + \mathbf{b}, \boldsymbol{\Sigma}_{\mathbf{z}|\mathbf{x}}\right). \tag{A.1b}$$

Then, the marginal probability density function of $\mathbf{z}$ *is given by*

$$p(\mathbf{z}) = \mathcal{N}\left(\mathbf{z}; \mathbf{A}\boldsymbol{\mu}_{\mathbf{x}} + \mathbf{b},\ \boldsymbol{\Sigma}_{\mathbf{z}|\mathbf{x}} + \mathbf{A}\boldsymbol{\Sigma}_{\mathbf{x}}\mathbf{A}^T\right). \tag{A.1c}$$

Furthermore, the conditional probability density function $p(\mathbf{x}|\mathbf{z})$ *is given by*

$$p(\mathbf{x}|\mathbf{z}) = \mathcal{N}\left(\mathbf{x}; \boldsymbol{\mu}_{\mathbf{x}|\mathbf{z}}, \boldsymbol{\Sigma}_{\mathbf{x}|\mathbf{z}}\right) \tag{A.1d}$$

with

$$\boldsymbol{\mu}_{\mathbf{x}|\mathbf{z}} = \boldsymbol{\mu}_{\mathbf{x}} + \boldsymbol{\Sigma}_x\mathbf{A}^T\boldsymbol{\Sigma}_z^{-1}\left(\mathbf{z} - (\mathbf{A}\boldsymbol{\mu}_{\mathbf{x}} + \mathbf{b})\right) \tag{A.1e}$$

$$\boldsymbol{\Sigma}_{\mathbf{x}|\mathbf{z}} = \boldsymbol{\Sigma}_{\mathbf{x}} - \boldsymbol{\Sigma}_{\mathbf{x}}\mathbf{A}^T\boldsymbol{\Sigma}_{\mathbf{z}}^{-1}\mathbf{A}\boldsymbol{\Sigma}_{\mathbf{x}}. \tag{A.1f}$$

Lemma A.1.2. *Let* $\mathbf{u}$ *be a partitioned random vector according to* $\mathbf{u} = \left[\mathbf{x}^T, \mathbf{z}^T\right]^T$ *with a joint probability density function according to*

$$p(\mathbf{u}) = \mathcal{N}\left(\begin{bmatrix}\mathbf{x}\\ \mathbf{z}\end{bmatrix}; \begin{bmatrix}\boldsymbol{\mu}_{\mathbf{x}}\\ \boldsymbol{\mu}_{\mathbf{z}}\end{bmatrix}, \begin{bmatrix}\boldsymbol{\Sigma}_{\mathbf{x}} & \boldsymbol{\Sigma}_{\mathbf{xz}}\\ \boldsymbol{\Sigma}_{\mathbf{xz}}^T & \boldsymbol{\Sigma}_{\mathbf{z}}\end{bmatrix}\right). \tag{A.2a}$$

Then, the marginal probability density function $p(\mathbf{x})$ *and the conditional probability density function* $p(\mathbf{x}|\mathbf{z})$ *are given by*

$$p(\mathbf{x}) = \mathcal{N}\left(\mathbf{x}; \boldsymbol{\mu}_{\mathbf{x}}, \boldsymbol{\Sigma}_{\mathbf{x}}\right) \tag{A.2b}$$

and

$$p(\mathbf{x}|\mathbf{z}) = \mathcal{N}\left(\mathbf{x}; \boldsymbol{\mu}_{\mathbf{x}} + \boldsymbol{\Sigma}_{\mathbf{xz}}\boldsymbol{\Sigma}_{\mathbf{z}}^{-1}, \boldsymbol{\Sigma}_{\mathbf{x}} - \boldsymbol{\Sigma}_{\mathbf{xz}}\boldsymbol{\Sigma}_{\mathbf{z}}^{-1}\boldsymbol{\Sigma}_{\mathbf{xz}}^T\right), \tag{A.2c}$$

respectively.

B. Elliptic Integrals

If $s^2(x)$ is a cubic or quadratic polynominal in x with simple zeros and $r(s,x)$ is a rational function of s and x containing at least one odd power of s, then

$$\int r(s,x)dx \tag{B.1}$$

is called an elliptic integral [94]. Two important elliptic integrals of the class of Legendre's integrals are given by

$$F(\phi,k) = \int_0^{\phi} \frac{d\theta}{\sqrt{1-k^2\sin^2(\theta)}} = \int_0^{\sin(\phi)} \frac{dt}{\sqrt{1-t^2}\sqrt{1-k^2t^2}} \tag{B.2}$$

$$E(\phi,k) = \int_0^{\phi} \sqrt{1-k^2\sin^2(\theta)} = \int_0^{\sin(\phi)} \frac{\sqrt{1-k^2t^2}}{\sqrt{1-t^2}}dt. \tag{B.3}$$

If $\phi = \frac{\pi}{2}$, these integrals are called complete ellptic integtrals of the first and second kind, respectively.

$$K(k) = \int_0^{\frac{\pi}{2}} \frac{d\theta}{\sqrt{1-k^2\sin^2(\theta)}} = \int_0^{1} \frac{dt}{\sqrt{1-t^2}\sqrt{1-k^2t^2}} \tag{B.4}$$

$$E(k) = \int_0^{\frac{\pi}{2}} \sqrt{1-k^2\sin^2(\theta)}d\theta = \int_0^{1} \frac{\sqrt{1-k^2t^2}}{\sqrt{1-t^2}}dt. \tag{B.5}$$

Bibliography

[1] S.M. Whittingham. Electrical energy storage and intercalation chemistry. *Science*, 192(4244):1126–1127, 1976. 1

[2] International Energy Agency. Technology roadmap: Electric and plug-in hybrid electric vehicles (ev/phev), 2011. 2

[3] C. M. Julien, A. Mauger, K. Zaghib, and H. Groult. Comparative issues of cathode materials for Li-ion batteries. *Inorganics*, 2:132–154, 2014. 2

[4] B. Scrosati and J. Garche. Lithium batteries: Status, prospects and future. *Journal of Power Sources*, 195:2419–2430, 2010. 2

[5] F. Larsson and B. Mellander. Abuse by external heating, overcharge and short circuiting of commercial lithium-ion battery cell. *Journal of the Electrochemical Society*, 161(10):A1611–A1617, 2014. 2

[6] K.A. Smith, C.D. Rahn, and C. Wang. Control oriented 1d electrochemical model of lithium ion battery. *Energy conversion and Management*, 48:2565–2578, 2007. 4

[7] K.A. Smith. Electrochemical control of lithium-ion batteries. *IEEE Control Systems Magazine*, 30:18–25, 2010. 4

[8] N.A. Chaturvedi, R. Klein, J. Christensen, J. Ahmed, and A. Kojic. Algorithms for advanced battery-management systems. *IEEE Control Systems Magazine*, 30:49 – 68, 2010. 4

[9] M. Corno, N. Bhatt, S.M. Savaresi, and M. Verhaegen. Electrochemical model-based state of charge estimation for li-ion cells. *IEEE Transactions on Control Systems Technology*, 23:117 – 127, 2015. 4

[10] T. Dao C. Schmitke. Developing mathematical models of batteries in modelica for energy storage applications. In *11^{th} International Modelica Conference*, 2015. 4

[11] J.E.B. Randels. Kinetics of rapid electrode reactions. *Discussions of the Faraday Society*, 1:11–19, 1947. 4

[12] H. He, R. Xiong, and J. Fan. Evaluation of lithium-ion battery equivalent circuit models for state of charge estimation by an experimental approach. *Energies*, 4:582–598, 2011. 4

[13] S. Li, C. Liao, and L. Wang. Research progress of equivalent circuit models for soc estimation of batteries in electric vehicles. In *2014 IEEE Conference and Expo Transportation Electrification Asia-Pacific (ITEC Asia-Pacific)*, 2014. 4

[14] G. Liu, L. Lu, H. Fu, and J. Hua. A comparative study of equivalent circuit models and enhanced equivalent circuit models of lithium-ion batteries with different model structures. In *2014 IEEE Conference and Expo Transportation Electrification Asia-Pacific (ITEC Asia-Pacific)*, 2014. 4

[15] C.C. Chan, E.W.C. Lo, and S. Weixiang. The available capacity computation model based on artificial neural network for lead–acid batteries in electric vehicles. *Journal of Power Sources*, 87:201–204, 2000. 4

[16] M. Charkhgard and M. Farrokhi. State-of-charge estimation for lithium-ion batteries using neural networks and ekf. *IEEE Transactions on Industrial Electronics*, 57(12):4178–4187, 2010. 4

[17] A.J. Salkind, C. Fennie, P. Singh, T. Atwater, and D.E. Reisner. Determination of state-of-charge and state-of-health of batteries by fuzzy logic methodology. *Journal of Power Sources*, 80:293–300, 1999. 4

[18] P. Singh, C. Fennie, and D. Reisner. Fuzzy logic modelling of state-of-charge and available capacity of nickel/metal hydride batteries. *Journal of Power Sources*, 136:322–333, 2004. 4

[19] M. Shahriari and M. Farrokhi. Online state-of-health estimation of vrla batteries using state of charge. *IEEE Transactions on Industrial Electronics*, 60(1):191–202, 2013. 4

[20] N. Watrin, B. Blunier, and A. Miraoui. Review of adaptive systems for lithium batteries state-of-charge and state-of-health estimation. In *2012 IEEE Transportation Electrification Conference and Expo (ITEC)*, 2012. 4, 40

[21] H. Rahimi-Eichi, F. Baronti, and M. Chow. Online adaptive parmeter identification and state-of-charge coestimation for lithium-polymer battery cells. *IEEE Transactions on Industrial Electronics*, 61:2053–2061, 2014. 4, 40

[22] C. Zhang, L.Y. Wang, X. Li, W. Chen, G.G. Yin, and J. Jiang. Robust and adaptive estimation of state of charge for lithium-ion batteries. *IEEE Transactions on Industrial Electronics*, 62:4948–4957, 2015. 4, 40

[23] J. Newman and K.E. Thomas-Alyea. *Electrochemical Systems*. John Wiley and Sons, Inc., 3rd edition, 2004. 6

[24] M. Sommer. *Implementation of an Electrochemical Model for Lithium-Ion Battery Condition Monitoring*. PhD thesis, Graz University of Technology, 2012. 7

[25] K. Zaghib, A. Guerfi, P.Hovington, A. Vijh, M. Trudeau, A. Mauger, J.B. Goodenough, and C.M. Julien. Review and analysis of nanostructured olivine-based lithium rechargeable batteries: Status and trends. *Journal of Power Sources*, 232:357–369, 2013. 7, 10, 11

[26] M.D. Bhatt and C. O'Dwyer. The role of carbonate and sulfite additives in propylene carbonate-based electrolytes on the formation of sei layers at graphitic Li-ion battery anodes. *Journal of Electrochemical Society*, 161(9):A1415–A1421, 2014. 8

[27] J.O. Besenhard and M. Winter. Insertion reactions in advanced electrochemical energy storage. *Pure and Applied Chemistry*, 70(3):603–608, 1998. 8

[28] M. Winter, J.O. Besenhard, M.E. Spahr, and P. Novák. Insertion electrode materials for rechargeable lithium batteries. *Journal of the Electrochemical Society*, 10(10):725–763, 1998. 10

[29] H. Matsui, T. Nakamura, Y. Kobayashi, M. Tabuchi, and Y. Yamada. Open-circuit voltage study on $LiFePO_4$ olivine cathode. *Journal of Power Sources*, 195:6879–6883, 2010 2010. 10, 13

[30] A. Yamada, H. Koizumi, S. Nishimura, N. Sonoyama, R. Kanno, M. Yonemura, T. Nakamura, and Y. Kobayashi. Room-temperature miscibility gap in Li_4FePO_4. *nature materials*, 5:357–360, 2006. 11

[31] A.K. Padhi, K.S. Nanjundaswamy, and J. B. Goodenough. Phospho-olivines as positive-electrode materials for rechargeable lithium batteries. *Journal of Electrochemical Society*, 144:1188–1194, 1997. 12

[32] A.S. Andersson and J.O. Thomas. The source of first-cycle capacity loss in $LiFePO_4$. *Journal of Power Sources*, 97:498–502, 2001. 12

[33] V. Srinivasan and J. Newman. Existence of path-dependence in the LiFePO4 electrode batteries, fuel cells, and energy conversion. *Electrochemical and Solid-State Letters*, 9(3):A110–A114, 2006. 12

[34] H.C. Shin, K.Y. Chung, W.S. Min, D.J. Byun, H. Jang, and B.W. Cho. Asymmetry between charge and discharge during high rate cycling in $LiFePO_4$ – in situ X-ray diffraction study. *Electrochemistry Communications*, 10:536–540, 2008. 12

[35] L. Laffont, C. Delacourt, P. Gibot, M. Yue Wu, P. Kooyman, C. Masquelier, and J.M Tarascon. Study of the $LiFePO_4/FePO_4$ two-phase system by high-resolution electron energy loss spectroscopy. *Chemistry of Materials*, 18(23):5520–5529, 2006. 12

[36] C. Delmas, M. Maccario, L. Croguennec, F. Le Cras, and F. Weill. Lithium deintercalation in $LiFePO_4$ nanoparticles via a domino-cascade model. *nature materials*, 7:665–671, 2008. 12

[37] G. Brunetti, D. Robert, P. Bayle-Guillemaud, J. L. Rouvière, E. F. Rauch, J. F. Martin, J. F. Colin, F. Bertin, and C. Cayron. Confirmation of the domino-cascade model by $LiFePO_4/FePO_4$ precession electron diffraction. *Chemistry of Materials*, 23(20):4515–4524, 2011. 12

[38] W. Dreyer, J. Jamnik, C. Guhlke, R. Huth, J., and M. Gaberšček. The thermodynamic origin of hysteresis in insertion batteries. *nature Materials*, 9:448–453, 2010. 13

[39] W. Dreyer, C. Guhlke, and M. Herrmann. Hystersis and phase transition in many-particle storage systems. *Continum Mech. Thermodyn.*, 23:211–231, 2010. 13

[40] T. Gallien and G. Brasseur. State of charge estimation of a $LiFePO_4$ battery: A dual estimation approach incorporating open circuit voltage hysteresis. Accepted paper I2MTC2016, 2016. 13, 67

[41] T. Gallien, B. Schweighofer, M. Recheis, and H. Wegleiter. State of charge determination of $LiFePO_4$ batteries using an external applied magnetic field. In *39th Annual Conference of the IEEE Industrial Electronics Society (IECON2013)*, pages 4000–4004, 2013. 13, 76

[42] T. Gallien, H. Krenn, R. Fischer, and H. Wegleiter. Magnetism vs. $LiFePO_4$ battery's state of charge: A route to a novel sensor concept. In *Conference on Precision Electromagnetic Measurements (CPEM 2014)*, 2014. 14, 75, 79

[43] T. Gallien, H. Krenn, R. Fischer, S. Lauterbach, B. Schweighofer, and H. Wegleiter. Magnetism vs. $LiFePO_4$ battery's state of charge: A feasibility study for magnetic-based charge monitoring. *IEEE Transactions on Instrumentation and Measurement*, 64(11):2959–2964, 2015. 14, 75, 77, 81

[44] K.T. Lee, W.H. Kan, and L.F. Nazar. Proof of intercrystallite ionic transport in $LiMPO_4$ electrodes (M = Fe, Mn). *Journal of the American Chemical Society*, 131:6044–6045, 2009. 15

[45] F. Baronti, W. Zamboni, N. Femia, R. Roncella, and R. Saletti. Experimental analysis of open-circuit voltage hysteresis in lithium-iron-phosphate batteries. In *IECON 2013 - 39th Annual Conference of the IEEE Industrial Electronics Society*, 2013. 17

[46] M. Grubmüller, B. Schweighofer, and H. Wegleiter. Fast, high accuracy, freely programmable single cell battery measurement system. In *IEEE International Instrumentation and Measurement Technology Conference (I2MTC) 2015*, 2015. 19, 38, 49

[47] E.A. Wan and A. Nelson. Dual Kalman filtering methods for nonlinear prediction, estimation, and smoothing. In *In Proceedings of the Neural Information Processing Systems Conference*, 1997. 23

[48] E.A. Wan and A. Nelson. Neural dual extended Kalman filtering: Applications in speech enhancement and monaural blind signal separation. In *In Neural Networks for Signal Processing VII: Proceedings of the 1997 IEEE Workshop*, 1997. 23

[49] E.A. Wan, R. van der Merwe, and A.T. Nelson. Dual estimation and the uncentend transformation. In *Neural Information Processing Systems (NIPS)*, 2000. 23

[50] E. Wan and R. van der Merwe. The uncented Kalman filter for nonlinear estimation. In *IEEE Symposium 2000 on Adaptive Systems for Signal Processing, Communications, and Control*, 2000. 23

[51] F. Gustafsson and T. Schön. Particle filters for system identification of state-space models linear in either parameters or states. In *In proceedings of the 13th IFAC Symposium on System Identification*, pages 1287–1292, 2003. 23, 46

[52] T. Schön, F. Gustafsson, and P. Nordlund. Marginalized particle filters for mixed linear/nonlinear state-space models. *IEEE Transactions on Signal Processing*, 53:2279–2289, 2005. 23, 29, 33

[53] A.L. Barker, D.E. Brown, and W.N. Martin. Bayesian estimation and the kalman filter. *Computers & Mathematics with Applications*, 30(10):55–77, 1995. 25

[54] M.S. Grewal and A.P. Andrews. *Kalman Filtering: Theory and Practice Using MATLAB*. John Wiley and Sons, Inc., second edition, 2001. 25

[55] M. S. Arulampalam, Maskell S, N. Gorden, and T. Clapp. A tutorial on particle filters for online nonlinear/non-Gaussian Bayesian tracking. *IEEE Transactions on Signal Processing*, 50:177–188, 2002. 25

[56] A. Doucet and A.M. Johansen. A tutorial on particle filtering and smoothing: Fifteen years later, 2008. 25, 26, 28

[57] S. Särkkä. *Bayesian Filtering and Smoothing*. Cambridge University Press, 2013. 25

[58] F. Gustafsson. Particle filter theory and practice with positioning applications. *IEEE A&E Systems Magazine*, 7:53 – 82, 2010. 25

[59] O. Cappé, S.J. Godsill, and E. Moulines. An overview of existing methods and recent advances in sequential monte carlo. *Proceedings of the IEEE*, 95:899 – 924, 2007. 25

[60] M. Klaas, N. de Freitas, and A. Doucet. Toward practical N^2 Monte Carlo: the marginal particle filter. In *Proceedings of the Twenty-First Conference on Uncertainty in Artificial Intelligence (UAI2005)*, 2005. 27, 92

[61] J. D. Hol, T. B. Schön, and F. Gustafsson. On resampling algorithms for particle filters. In *Nonlinear Statistical Signal Processing Workshop*, pages 79–82. IEEE, 2006. 28, 42

[62] R. Douc, O. Cappé, and E. Moulines. Comparison of resampling schemes for particle filtering. In *4th International Symposium on Image and Signal Processing and Analysis (ISPA)*, 2005. 28, 42

[63] P. Del Moral, A. Doucet, and A. Jasra. On adaptive resampling strategies for sequential Monte-Carlo methods. *Bernoulli*, 18(1):252–278, 2012. 28, 42

[64] N.J. Gordon, D.J. Salmond, and A.F.M. Smith. Novel approach to nonlinear/non-Gaussian Bayesian state estimation. *Radar and Signal Processing, IEE Proceedings F*, 140:107–113, 1993. 28, 46

[65] J.V. Candy. Bootstrap particle filtering. *IEEE Signal Processing Magazine*, 24:73–85, 2007. 28

[66] A. Doucet, S. Godsill, and C. Andrieu. On sequential Monte Carlo sampling methods for Bayesian filtering. *Statistics and Computing*, 10:197–208, 2000. 29, 41

[67] R. Fisher. On the mathematical foundations of theoretical statistics. *Philosophical Transactions of the Royal Society*, 222:309–368, 1922. 29

[68] T. B. Schön. *Estimation of Nonlinear Dynamic Systems, Theory and Applications*. PhD thesis, Department of Electrical Engineering, Linköpings University, 2006. 33

[69] F. Lindsten and T.B. Schön. Identification of mixed linear/nonlinear state-space models. In *49th IEEE Conference on Deciosion and Control (CDC)*, 2010. 33

[70] F. Lindsten. *Rao-Blackwellised particle methods for inference and identification*. PhD thesis, Linköping University, 2011. 34, 41, 46

[71] D. Haifeng, W. Xuezhe, and S. Zechang. State and parameter estimation of a hev li-ion battery pack using adaptive kalman filter with a new soc-ocv concept. In *International Conference on Measuring Technology and Mechatronics Automation ICMTMA '09*, 2009. 40

[72] S. Sepasi, R. Ghorbani, and B.Y. Liaw. Soc estimation for aged lithium-ion batteries using model adaptive extended kalman filter. In *2013 IEEE Transportation Electrification Conference and Expo (ITEC)*, 2013. 40

[73] D. Simon and D.L. Simon. Kalman filtering with inequality constraints for turbofan engine health estimation. *IEE Proceedings - Control Theory and Applications*, 153:371–378, 2006. 42

[74] N. Gupta and R. Hauser. Kalman filtering with equality and inequality state constraints. Technical report, Oxford University Computing Laboratory, Numerical Analysis Group, 2008. 42

[75] D. Simon. Kalman filtering with state constraints: a survey of linear and nonlinear algorithms. *IET Control Theory and Applications*, 4:1303–1318, 2010. 42

[76] T.L. Chia, D.Simon, and H.J. Chizeck. Kalman filtering with statistical state constraints. 42

[77] F. Lindsten, T. Schön, and L. Svensson. A non-degenerate rao-blackwellised particle filter for estimating static parameters in dynamical models. In *16th IFAC Symposium on System Identification*, pages 1149–1154, 2012. 46, 92

[78] Z. Ghahramani. An introduction to hidden markov markov models and bayesian networks. *Internation Journal of Pattern Recognition and Artificial Intelligence*, 15:9–42, 2001. 46

[79] O. Cappé, E. Moulines, and T. Ryden. *Inference in Hidden Markov models*. Springer Series in Statistics, 2005. 46

[80] R. Douc, G. Fort, E. Moulines, and P. Priouret. Forgetting the inital distribution for hidden Markov models. *Stochiastic Processes and their Applications*, 119:1235–1256, 2009. 46

[81] R. Douc, A. Garivier, E. Moulines, and J. Olsson. Sequential Monte Carlo smoothing for general state space hidden Markov models. *The Annals of Applied Probability*, 21:2109–2145, 2011. 46

[82] G. Kitagawa. A self-organizing state-space model. *Journal of the American Statistical Association*, 93:1203–1215, 1998. 46

[83] N.A. Chernova, G.M. Nolis, F.O. Omenya, H. Zhou, Z. Li, and S.M. Whittingham. What can we learn about battery materials from their magnetic properties? *Journal of Materials Chemistry*, 21:9865–9875, 2011. Chemie. 68, 75

[84] J.M.D. Coey. *Magnetism and Magnetic Materials*. Cambridge University Press, 2010. 69

[85] N.A. Spaldin. *Magnetic Materials: Fundamentals and Applications*. Cambridge University Press, 2nd edition, 2010. 69

[86] Stephen Blundell. *Magnetism in Condensed Matter*. Oxford University Press, 2001. 69

[87] B.A. Averill and P. Eldredge. Principles in general chemistry. 73

[88] J.G. Creer and G.J. Troup. The magnetic susceptibility of $LiFePO_4$ and $LiCoPO_4$ and. *Physics Letters A*, 32(6):439–440, 1970. 75

[89] P. Axmann, C. Stinner, M. Wohlfahrt-Mehrens, A. Mauger, F. Gendron, and C.M. Julien. Nonstoichiometric $LiFePO_4$: Defects and related properties. *Chem. Mater.*, 21(8):1636–1644, 2009. 75

[90] R. Toft-Petersen, M. Reehuis, T. B. S. Jensen, N. H. Andersen, J. Li, M. D. Li, M. D. Le, M. Laver, C. Niedermayer, B. Klemke, K. Lefmann, and D. Vakin. Anomalous magnetic structure and spin dynamics in magnetoelectric $LiFePO_4$. *Physical Review B*, 92:024404, 2015. 75

[91] M.C. Tucker, M.M. Doeff, T.J. Richardson, R. Fi nes, E.J. Chairns, and J.A. Reimer. Hyperfine fields at the Li site in $LiFePO_4$-type olivine materials for lithium rechargeable batteries: A ^{7}Li MAS NMR and SQUID study. *Journal of the American Chemical Society*, 124:3832 – 3833, 2002. 75

[92] K. Zaghib, J. Trottier, A. Mauger, H. Groult, and C.M. Julien. Surface and bulk properties of $LiFePO_4$ probed by the magnetic analysis. *Int. J. Electrochem. Sci.*, 8:9000 – 9014, 2013. 75

[93] J. Tinnemeyer. New advances in lithium ion battery monitoring, 2011. 76

[94] F.W.J. Oliver, D.W. Lozier, R.F. Boisvert, and C.W. Clark, editors. *NIST Handbook of Mathematical Functions*, chapter Elliptic Integrals, pages 485 – 523. Cambridge University Press, 2010. 97